

Signatures of Topological Superconductors

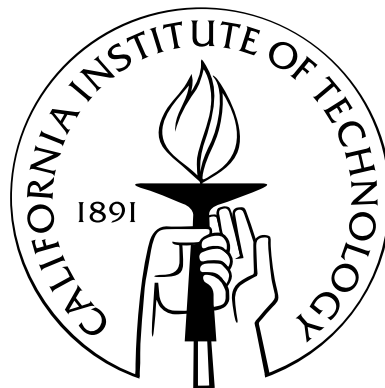
Thesis by

Shu-Ping Lee

In Partial Fulfillment of the Requirements

for the Degree of

Doctor of Philosophy



California Institute of Technology

Pasadena, California

2015

(Defended May 26, 2015)

For my parents, who inspired me to finish this.

Acknowledgements

My six years at Caltech have been among the most wonderful and colorful of my life. I am extremely lucky to have Jason Alicea as my PhD advisor, and I am deeply grateful to him for sharing his profound knowledge with me and making every effort to carve me into a good researcher. Whatever little bit I have learned, I greatly owe it to him.

During my six years at Caltech, I have greatly benefitted from working closely with very talented and motivated group members, including Paraj, David, Scott, and Karthik.

Finally, here I met my wife Debaleena Nandi, who has shared with me every joy and sorrow of life at Caltech. My parents, close family members, and friends have remained a great source of strength, as their love transcended academic achievements and helped me to withstand failures.

Abstract

Topological superconductors are particularly interesting in light of the active ongoing experimental[1, 2, 3] efforts for realizing exotic physics such as Majorana zero modes[1, 3]. These systems have excitations with non-Abelian exchange statistics, which provides a path towards topological quantum information processing. Intrinsic topological superconductors are quite rare in nature. However, one can engineer topological superconductivity by inducing effective p-wave pairing in materials which can be grown in the laboratory. One possibility is to induce the proximity effect in topological insulators[4]; another is to use hybrid structures of superconductors and semiconductors[5, 6, 7].

The proposal of interfacing s-wave superconductors with quantum spin Hall systems provides a promising route to ‘engineered’ topological superconductivity. Given the exciting recent progress on the fabrication side, identifying experiments that definitively expose the topological superconducting phase (and clearly distinguish it from a trivial state) raises an increasingly important problem. With this goal in mind, we proposed a detection scheme[8] to get an unambiguous signature of topological superconductivity, even in the presence of ordinarily detrimental effects such as thermal fluctuations and quasiparticle poisoning. We considered a Josephson junction built on top of a quantum spin Hall material. This system allows the proximity effect to turn edge states in effective topological superconductors. Such a setup is promising because experimentalists have demonstrated that supercurrents indeed flow through quantum spin Hall edges[2, 9]. To demonstrate the topological nature of the superconducting quantum spin Hall edges, theorists have proposed examining the periodicity of Josephson currents respect to the phase across a Josephson junction.

The periodicity of tunneling currents of ground states in a topological superconductor Josephson junction is double that of a conventional Josephson junction. In practice, this modification of periodicity is extremely difficult to observe because noise sources, such as quasiparticle poisoning, wash out the signature of topological superconductors. For this reason, we propose a new, relatively simple DC measurement that can compellingly reveal topological superconductivity in such quantum spin Hall/superconductor heterostructures. More specifically, we develop a general framework for capturing the junction's current-voltage characteristics as a function of applied magnetic flux. Our analysis reveals sharp signatures of topological superconductivity in the field-dependent critical current. These signatures include the presence of multiple critical currents and a non-vanishing critical current for all magnetic field strengths as a reliable identification scheme for topological superconductivity.

This system becomes more interesting as interactions between electrons are involved. By modeling edge states as a Luttinger liquid, we find that conductance provides universal signatures to distinguish between normal and topological superconductors. More specifically, we use renormalization group methods to extract universal transport characteristics of superconductor/quantum spin Hall heterostructures where the native edge states serve as a lead. Interestingly, arbitrarily weak interactions induce qualitative changes in the behavior relative to the free-fermion limit, leading to a sharp dichotomy in conductance for the trivial (narrow superconductor) and topological (wide superconductor) cases. Furthermore, we find that strong interactions can in principle induce 'parafermion' excitations at a superconductor/quantum spin Hall junction.

As we identify the existence of topological superconductor, we can take a step further. One can use topological superconductor for realizing Majorana modes by breaking time reversal symmetry. An advantage of 2D topological insulator is that networks required for braiding Majoranas along the edge channels can be obtained by adjoining 2D topological insulators to form corner junctions. Physically cutting quantum wells for this purpose, however, presents technical challenges. For this reason, I propose a more accessible means of forming networks that relies on dynamically ma-

nipulating the location of edge states inside of a *single* 2D topological insulator sheet. In particular, I show that edge states can effectively be dragged into the system's interior by gating a region near the edge into a metallic regime and then removing the resulting gapless carriers via proximity-induced superconductivity. This method allows one to construct rather general quasi-1D networks along which Majorana modes can be exchanged by electrostatic means.

Apart from 2D topological insulators, Majorana fermions can also be generated in other more accessible materials such as semiconductors. Following up on a suggestion by experimentalist Charlie Marcus, I proposed a novel geometry to create Majorana fermions by placing a 2D electron gas in proximity to an interdigitated superconductor-ferromagnet structure[10]. This architecture evades several manufacturing challenges by allowing single-side fabrication and widening the class of 2D electron gas that may be used, such as the surface states of bulk semiconductors. Furthermore, it naturally allows one to trap and manipulate Majorana fermions through the application of currents. Thus, this structure may lead to the development of a circuit that enables fully electrical manipulation of topologically-protected quantum memory. To reveal these exotic Majorana zero modes, I also proposed an interference scheme to detect Majorana fermions that is broadly applicable to any 2D topological superconductor platform.

Contents

Acknowledgements	iv
Abstract	v
1 Introduction	1
1.1 Quantum computation	1
1.2 Properties of a topological phase	2
1.3 Introduction of Majorana fermion	3
1.4 Kitaev model for a 1D spinless p-wave superconductor	4
1.5 Realization of Kitaev chain in the edge states of a 2D topological insulator	7
1.6 Realization of Kitaev chain in a semiconductor wire	10
1.7 Realization of $p_x + ip_y$ superconductor in a 2D system	13
1.8 Fractional Josephson effect	14
1.9 Tunneling spectroscopy of Majorana zero modes	20
1.10 Experimental progress on topological superconductors	23
1.11 Outline of this thesis	25
2 Dynamical manipulation of 2D topological insulator edge states for Majorana fermion braiding	28
2.1 Introduction	28
2.2 Relocated edge states	29
2.3 Phase diagram of relocated edge states	35
2.4 Network of relocated edge states for braiding	38

3	Revealing topological superconductivity in extended quantum spin Hall Josephson junctions	41
3.1	Motivation	41
3.2	Extended Josephson junction model	43
3.3	Fokker-Planck analysis	46
3.4	Parity conserved case	48
3.5	Low bath temperature parity switching case	50
3.5.1	Critical current with minimum energy	53
3.6	High bath temperature parity switching case	60
3.7	Discussion	64
4	Universal transport signatures of topological superconductivity in quantum spin Hall architectures	66
4.1	Introduction	66
4.2	Setup	68
4.3	Hamiltonian of the system	69
4.4	Fixed point actions for infinite superconductor	71
4.4.1	Perturbing the fixed point actions with TRI terms in infinite SC case	72
4.4.2	Perturbing the fixed point actions with TRB terms in infinite SC case	75
4.5	Fixed point actions for finite superconductor	76
4.5.1	Perturbing the fixed point actions with TRI terms in short SC case	77
4.5.2	Perturbing the fixed point actions with TRB terms in finite SC case	79
4.6	Conductance	79
4.6.1	Time reversal invariant case	81
4.6.2	Time reversal broken case	84
4.7	Conclusions	86

4.8	Appendix:Parafermion zero mode	86
4.9	Appendix:Perfect Andreeve reflection	88
4.10	Appendix:Perfect normal reflection	90
4.11	Appendix:Perfect normal transmission	92
4.12	Appendix:Expansion of partition function	94
4.13	Appendix:Duality for $\cos 4\theta$	97
5	Electrical manipulation of Majorana fermions in an interdigitated superconductor-ferromagnet device	99
6	Future direction	110
	Bibliography	112

Chapter 1

Introduction

1.1 Quantum computation

The idea of quantum computation can be traced back to 1982 when Richard Feynman proposed to use quantum mechanical wave functions of systems to simulate quantum phenomena. The motivation behind this is that the number of bits for a classical computer to simulate a quantum system will exponentially increase with the system size, while the quantum computer will only take a linear number of qubits to do the same job. One example is an N qubit quantum system. This system has 2^N states and therefore it will take a classical computer 2^N bits to compute all states. For a quantum computer, we will only need N qubits to simulate the same system. Apart from computation power, quantum computation also has its necessity in current technology. One of the key ingredients to progress current processor technology relies on size reduction of transistors. The transistors nowadays are about the nanoscale size. As the size of transistors keeps shrinking down, quantum mechanics will automatically appear in the transistors. In other words, we cannot simply use boolean algebra to describe an on or off state of a transistor; instead, we need quantum mechanics to describe the superposition of both on and off states that appear in the systems. For these reasons, quantum computation has drawn much attention from both theorists and experimentalists.

One major challenge of quantum computation is that once the qubits couple to their environment, perturbations coming from the environment can destroy the coher-

ence of qubits. For this reason, people try to circumvent this difficulty by using the fact that perturbations are local operators; therefore, one can maintain the coherence of states if one builds a qubit that is nonlocal. In this way, the nonlocal qubits will be immune to any local measurement which allows coherence of states to be maintained.

The question is; how do we build a nonlocal qubit? This can be accomplished by using the topological properties of materials. One main reason is that the topological properties of a system can only be changed when the system involves a global operations. Therefore, the qubit that is based on topological properties of a material cannot be destroyed by any local perturbations. In the following section, we will address the properties of a topological phase in more detail.

1.2 Properties of a topological phase

To get an idea of topological phase, one can think about the quantum Hall effect. When a perpendicular magnetic field is applied to a 2D electron gas, the electrons will undergo cyclotron motion due to Lorentz force, as shown in Fig.1.1. As a consequence, electrons become localized and the bulk is insulating. However, quantum Hall insulators are fundamentally distinct from trivial insulators. One can see this in Fig.1.1. The electrons on the edges of a quantum Hall insulator cannot complete their circular motion. Once an electron bounces back from the edges, Lorentz force moves electron forward. This provides a conducting channel along the edges. The emergence of edge states is one of the features that distinguishes between topological and trivial insulating phases. The quantum Hall effect is a topological phase that occurs in magnetic field where time reversal is not present. In 2005, it was realized that there is a new type of topological phase in the presence of time reversal invariance, which is named topological insulators later on. Similar to quantum Hall effect, topological insulator also has gapless modes that appear at its boundary. Time reversal symmetry guarantees that the single particle Hamiltonian of spin half systems has Kramer's degeneracy. In a 2D system, this means it has two counter propagating edge modes with opposite spins. In a 3D system, this gives rise to the

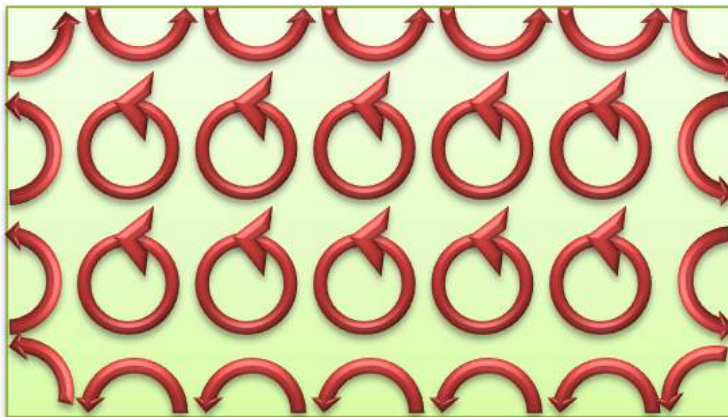


Figure 1.1: Cartoon for quantum Hall effect. Once the magnetic field is threaded into 2D electron gas, electrons undergo cyclotron motion in which resulting insulating phase in the bulk. On the other hand, electrons at the edges cannot complete this circular motion in which provides a conducting channel along the edges.

helicity of surface states, which gives spin-momentum locking in surface states.

The topological phases of matter that coexist with superconductivity are called topological superconductors [11, 12, 13, 14, 15]. One can induce exotic physics in topological superconductors. As we will see in the following sections, Majorana zero modes can be engineered in such systems.

1.3 Introduction of Majorana fermion

Majorana fermion was first proposed by Ettore Majorana in 1937, when he stated that if a charge neutral spin 1/2 fermions can be described by real wavefunctions, then this charge neutral particle must be its own antiparticle. For condensed matter physicists, the key ingredients of having Majorana zero modes come from inducing superconductivity in topological phase. To see this, one can diagonalize the Hamiltonian of a superconducting system by writing down its Hamiltonian in the Nambu spinor basis $\Psi = (c_{\uparrow}, c_{\downarrow}, c_{\downarrow}^{\dagger}, -c_{\uparrow}^{\dagger})^T$ as

$$H = \int dx \Psi^{\dagger} \hat{H} \Psi = \int dx \Psi^{\dagger}(\mathbf{r}) \begin{pmatrix} H_0 & \Delta_0(\mathbf{r}) \\ \Delta_0^*(\mathbf{r}) & -\sigma_y H_0^* \sigma_y \end{pmatrix} \Psi(\mathbf{r}) \quad (1.1)$$

Here c , H_0 , Δ and σ are electron operator, kinetic term, pairing potential and Pauli matrix of spin respectively. One can diagonalize superconducting systems by invoking Bogoliubov transformations. To do that, we calculate the wave function $\Phi_E(\mathbf{r}) = (u_{\uparrow,E}(\mathbf{r}), u_{\downarrow,E}(\mathbf{r}), v_{\downarrow,E}(\mathbf{r}), -v_{\uparrow,E}(\mathbf{r}))^T$ by solving the BdG equation $\hat{H}\Phi_E = E\Phi_E$. Using the solutions of the BdG equations, one can define Bogoliubov quasiparticle operators as $\hat{\gamma}_E^\dagger = \int d\mathbf{r} \sum_\sigma u_{\sigma,E}(\mathbf{r})\hat{c}_\sigma^\dagger(\mathbf{r}) + v_{\sigma,E}(\mathbf{r})\hat{c}_\sigma(\mathbf{r})$. One can show that Bogoliubov quasiparticle operator satisfies the relation of $\hat{\gamma}_E^\dagger = \hat{\gamma}_{-E}$. At zero energy $E = 0$, this relation gives $\hat{\gamma}_0^\dagger = \hat{\gamma}_0$, which is the definition of Majorana operators. In other words, zero energy excitations in superconducting systems correspond to Majorana zero modes. One can find Majorana zero energy modes in a spinless p-wave superconductor. In the following section, we use a Kitaev model of a spinless p-wave superconductor to describe the concept of inducing Majorana modes in more detail.

1.4 Kitaev model for a 1D spinless p-wave superconductor

The motivations for finding Majorana zero modes are two-fold. First, one can use Majorana zero modes to build a nonlocal qubit that is immune to local measurement[16]. Second, this nonlocal qubit is protected by the topological properties of materials. We call it a topologically protected qubit. One way to build a topological protected qubit is to decompose a single fermionic states into two Majorana fermions, and spatially separate these two Majorana fermions. This can be achieved through a topological superconductor such as a spinless p-wave wire[11]. Here we follow the derivation that is shown in ref. [17]: we start from the Kitaev model that describes the Hamiltonian of 1D spinless p-wave superconductor

$$H_p = -\frac{t}{2} \sum_{j=0}^{N-1} \left(c_{j+1}^\dagger c_j + c_j^\dagger c_{j+1} \right) - \frac{\Delta}{2} \sum_{j=0}^{N-1} \left(c_j c_{j+1} + c_{j+1}^\dagger c_j^\dagger \right) - \mu \sum_{j=0}^N c_j^\dagger c_j \quad (1.2)$$

The first term is the kinetic term to describe the hopping of electrons. The second term is the p-wave pairing potential. The third term is the chemical potential terms. To see Majorana fermions appear in the systems, we decompose a Dirac fermion operator c into two Majorana operators γ_a and γ_b in the following way

$$c_j = \frac{1}{2}(\gamma_{b,j} + i\gamma_{a,j}) \quad (1.3)$$

$$c_j^\dagger = \frac{1}{2}(\gamma_{b,j} - i\gamma_{a,j}) \quad (1.4)$$

We can check that γ_a and γ_b indeed satisfied the conditions for Majorana fermions

$$\gamma_{a,j} = \gamma_{a,j}^\dagger \quad (1.5)$$

$$\{\gamma_{\alpha,i}, \gamma_{\beta,j}\} = 2\delta_{\alpha\beta}\delta_{ij} \quad (1.6)$$

We can write the Hamiltonian of p-wave superconductor wire in the Majorana fermions basis. This allows one to see how Majorana fermions couple to each other. For simplicity, we consider pairing potential Δ equal to hopping strength t . The Hamiltonian in Majorana basis becomes

$$H_p = -\frac{i}{2}\Delta \sum_{j=0}^{N-1} \gamma_{b,j}\gamma_{a,j+1} + \frac{i}{2}\mu \sum_{j=0}^N \gamma_{b,j}\gamma_{a,j} \quad (1.7)$$

As one can see from the Hamiltonian, pairing Δ and hopping t term couple two Majorana fermions on nearest neighbor sites, meanwhile, chemical potential μ couples Majorana fermions on the same site. The phase transition between trivial and topological appears, as we adjust the coupling Δ and μ . Trivial phase appears when the coupling of Majorana fermions in the same lattice site is larger than the coupling between different sites (i.e., $|\mu| > |\Delta| = |t|$). One way to see this in an explicit way is by tuning the parameters in the Hamiltonian of eq.1.2 as $\Delta = t = 0$ and $\mu < 0$. In this way, chemical potential is the only term that remains and therefore it is in trivial phase. If we write the Hamiltonian of this trivial phase in Majorana fermion basis, we will find that all Majorana fermions are paired in the same lattice site, as

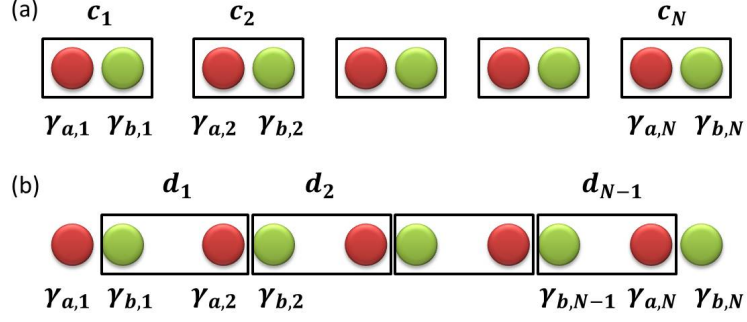


Figure 1.2: (a) In trivial phase, all Majorana fermions pair up at the same lattice site, which leads to ground states being gapped and no unpaired Majorana modes left at the ends of the wire. (b) In topological phase, two unpaired Majorana zero energy modes appear at the end of the 1D spinless p-wave wire.

shown in fig.(1.2)(a) and eq.1.8:

$$H_p = \frac{i}{2}\mu \sum_{j=0}^N \gamma_{b,j} \gamma_{a,j} \quad (1.8)$$

In contrast to trivial phase, topological phase arises when the coupling of nearest neighbor dominates on-site coupling of Majorana fermions (i.e. $|\mu| < |\Delta| = |t|$). To see this, we consider the Hamiltonian when chemical potential $\mu = 0$, and rewrite the Hamiltonian in eq.1.7 as

$$H_p = -\frac{i}{2}\Delta \sum_{j=0}^{N-1} \gamma_{b,j} \gamma_{a,j+1} \quad (1.9)$$

We can schematically plot the coupling between $\gamma_{a,j}$ and $\gamma_{b,j+1}$ in eq. 1.9 on Fig.(1.2)(b). From Fig. (1.2)(b), one can see that there are two unpaired Majorana fermions left at the end of this p-wave wire. We can show that those unpaired Majorana fermions correspond to zero energy modes by diagonalization of the Hamiltonian. To do so, we rewrite the Hamiltonian into the eigen energy basis by defining

$$d_j = \frac{1}{2}(\gamma_{a,j+1} + i\gamma_{b,j}) \quad (1.10)$$

$$d_N = \frac{1}{2}(\gamma_{a,1} + i\gamma_{b,N}) \quad (1.11)$$

Then we rewrite the Hamiltonian of eq.1.9 in this d basis as

$$H_p = \left[\Delta \sum_{j=0}^{N-1} \left(d_j^\dagger d_j - \frac{1}{2} \right) \right] + 0 \left(d_N^\dagger d_N - \frac{1}{2} \right) \quad (1.12)$$

As we write the Hamiltonian in eigen energy basis, we find that d_N operator corresponds to zero energy modes. Since d_N is composed by $\gamma_{a,1}$ and $\gamma_{b,N}$, that means there are two Majorana fermions $\gamma_{a,1}$ and $\gamma_{b,N}$ that appear at the end of a wire as zero energy modes.

1.5 Realization of Kitaev chain in the edge states of a 2D topological insulator

Intrinsic p-wave superconductors are very rare in nature. However, we can engineer this exotic phase in lab by more accessible means. One example is inducing proximity pairing potential on the edge states of 2D topological insulators[4]. In this way, we use pairing potential to couple left ψ_L and right ψ_R movers, and transform the edge states into an effective p-wave superconductor wire. One can see this in a more explicit way by rewriting the Hamiltonian of edge states in the eigen energy basis. We start from the Hamiltonian of edge states:

$$H_{edge} = \int dk \psi_L^\dagger(-v_f k) \psi_L + \psi_R^\dagger(v_f k) \psi_R \quad (1.13)$$

As we induce proximity effect by coupling superconductivity to edge states, we effectively add pairing potential Δ in the edge states.

$$H_\Delta = \Delta \int dk \psi_R(k) \psi_L(-k) + h.c. \quad (1.14)$$

To show that inducing pairing potential in edge states is equivalent to a p-wave superconducting wire, we rewrite the Hamiltonian in the following basis:

$$\xi_+(k) = \begin{cases} \psi_R(k), & \text{if } k \geq 0 \\ \psi_L(k), & \text{if } k < 0 \end{cases} \quad (1.15)$$

$$\xi_-(k) = \begin{cases} \psi_R(k), & \text{if } k < 0 \\ \psi_L(k), & \text{if } k \geq 0 \end{cases} \quad (1.16)$$

The changing of basis allows us to rewrite the pairing term as

$$H_\Delta = \Delta \int_0^\infty dk \xi_+(k) \xi_+(-k) + \Delta \int_{-\infty}^0 dk \xi_-(k) \xi_-(-k) + h.c. \quad (1.17)$$

$$= \int_{-\infty}^\infty dk \left(\frac{\Delta}{2} \text{sign}(k) \right) (\xi_+(k) \xi_+(-k) + \xi_-(k) \xi_-(-k)) + h.c. \quad (1.18)$$

The pairing potential $\Delta \text{sign}(k)$ in eq.1.18 reveals that the edge states indeed become effective p-wave superconducting wire as we couple them to a regular s-wave superconductor. The topological superconductor that we induce from the edge states has time reversal symmetry, in contrast to the spinless p-wave superconductor where time reversal symmetry is already broken.

One can induce Majorana zero modes from this topological superconducting phase by breaking time reversal symmetry. To do that, we apply Zeeman field to the systems and model it as

$$H_Z = \int dx V_z(x) \psi_R^\dagger(x) \psi_L(x) + h.c. \quad (1.19)$$

The total Hamiltonian $H_{\text{tot}} = H_{\text{edge}} + H_\Delta + H_Z$ can be written in Nambu spinors basis $\Psi = (\psi_R, \psi_L, \psi_L^\dagger, -\psi_R^\dagger)^T$ as

$$H_{\text{tot}} = -iv_f \sigma_z \tau_z \partial_x + \Delta(x) \tau_x + V_z(x) \sigma_x \quad (1.20)$$

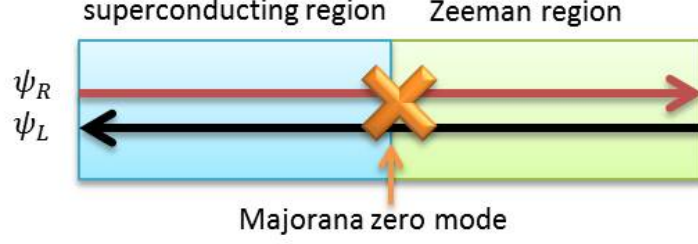


Figure 1.3: A Majorana zero mode appears on the domain wall between topological phase and trivial phase. Here topological phase comes from proximity induced superconductivity in the edge states, while trivial phase corresponds to the region where edge states are gapped by Zeeman splitting.

We then separate the edge states into two regions. As shown in Fig.(1.3), on the left side ($x < 0$) edge states are gapped by superconductivity ($V_z = 0$ in this side) and on the other side ($x > 0$) they are gapped by Zeeman splitting ($\Delta = 0$ in this side). In this way, we create a topological superconducting phase on one side and a trivial phase on the other side. One can diagonalize the total Hamiltonian in eq.(1.20) to see the Majorana zero modes. The wave function of zero energy modes is

$$\Phi = e^{\frac{\Delta}{v}x}(1, -i, i, -1)^T \text{ for } x < 0 \quad (1.21)$$

$$= e^{-\frac{V_z}{v}x}(1, -i, i, -1)^T \text{ for } x > 0 \quad (1.22)$$

In other word, the operator of zero energy excitations can be written as

$$\gamma_0 = \int_{-\infty}^0 dx e^{\frac{\Delta}{v}x}(\psi_R - i\psi_L + i\psi_L^\dagger + \psi_R^\dagger) + \int_0^{\infty} dx e^{-\frac{V_z}{v}x}(\psi_R - i\psi_L + i\psi_L^\dagger + \psi_R^\dagger) \quad (1.23)$$

This zero energy mode operator satisfies $\gamma_0 = \gamma_0^\dagger$, which is the definition of a Majorana operator. Furthermore, it peaks at $x = 0$, which is the location of the domain wall between the topological superconducting phase and the trivial phase.

1.6 Realization of Kitaev chain in a semiconductor wire

Apart from 2D topological insulator, topological superconductors can also be induced in semiconductor systems. The semiconductor platform has drawn much attention because it allows a wider class of materials for realizing this exotic phase. The main idea is using the Zeeman field to lift the spin degeneracy of band structure in order to create an effective spinless environment, and then we use the spin orbital interaction of the semiconductor to create 2π winding of spin on each band. The 2π winding of spin arises from the topological phase, which gives topological superconductivity as we induce proximity effect on the semiconductor. In the following, we illustrate this idea in great detail.

Let's first start with the kinetic energy of electrons, which is given as $\frac{\hbar^2 k^2}{2m} - \mu$ with μ as chemical potential. This band structure is two-fold degenerate, because both spin up and down electron have the same band structure. As we include spin orbital interaction that appears in the semiconductor, we lift the spin degeneracy of the band structure except at zero momentum. We can diagonalize the Hamiltonian to see this. The Hamiltonian with spin orbit interaction can be written in the spin basis $\Psi^\dagger = (\psi_\uparrow^\dagger, \psi_\downarrow^\dagger)$ as

$$H_K = \int dk_x \Psi^\dagger \left(\frac{\hbar^2 k_x^2}{2m} - \mu \right) \Psi \quad (1.24)$$

$$H_{\text{soc}} = \alpha \int dk_x \Psi^\dagger \sigma_y k_x \Psi \quad (1.25)$$

Here σ_y is the Pauli matrix for spin. By diagonalizing the Hamiltonian in eq.1.25, we get the band structure shown in Fig.(1.4). The red and black curves in fig.1.4 correspond to the opposite directions of electron spins. As one can see from this figure, for a given chemical potential μ , chemical potential always intersects with two bands. Each band gives 2π winding of spin due to spin orbital interaction. The spin winds in opposite directions on each band, which results in the cancelation of

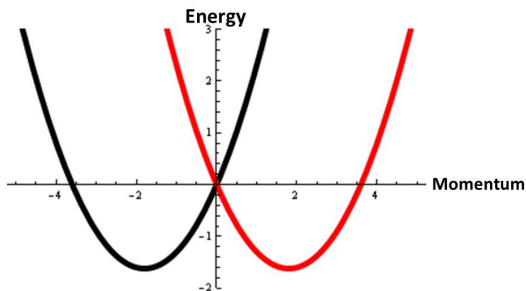


Figure 1.4: Band structure with Rashba spin orbital interactions. Red and black curve have opposite spins.

topological index–Chern number. In order to get the topological phase, we will need to reduce the number of bands that the chemical potential intersected from two to one. One way to achieve this goal is by applying a magnetic field to induce Zeeman splitting. We can see this in a more explicit way by writing down the Zeeman term as

$$H_{\text{Zeeman}} = V_z \int dk_x \Psi^\dagger \sigma_z \Psi \quad (1.26)$$

Now, we can diagonalize the Hamiltonian of semiconductor wire and Zeeman term together to get the band structures shown in Fig.(1.5). As we tune the chemical potential μ inside the Zeeman gap V_z , we have effectively created a spinless system because chemical potential intersects with a single band. We can then induce proximity pairing Δ on a semiconductor wire to engineer effective spinless p-wave superconductor. To see this, we model the proximity pairing term as

$$H_{\text{sc}} = \Delta \int dk \psi_\downarrow^\dagger \psi_\uparrow^\dagger + h.c. \quad (1.27)$$

One can diagonalize the total Hamiltonian $H_K + H_{\text{soc}} + H_{\text{Zeeman}} + H_{\text{sc}}$ and extract the energy gap at zero momentum as $V_z - \sqrt{\Delta^2 + \mu^2}$. This gap closes at $V_z = \sqrt{\Delta^2 + \mu^2}$, where the wire undergoes a phase transition. In other word, the induced pairing potential arises from the trivial superconducting phase when Zeeman field is small ($V_z < \sqrt{\Delta^2 + \mu^2}$) and enters a topological superconducting phase when Zeeman field

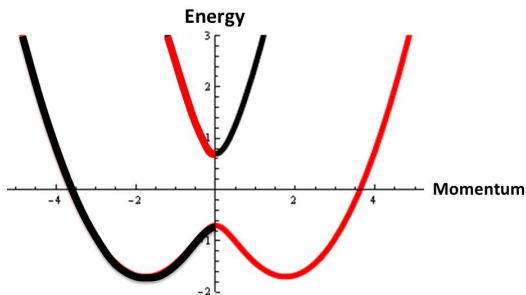


Figure 1.5: Band structure of semiconductor with both Rashba spin orbital interaction and Zeeman splitting. Red and black colors correspond to opposite spins.

is large ($V_z > \sqrt{\Delta^2 + \mu^2}$).

One can induce Majorana zero modes in a semiconductor wire once it enters topological superconducting phase. To see this, we consider a semiconductor wire with a Zeeman field that is spatially linear increased as $V_z = \Delta + ax$. Without losing generality, we consider chemical potential $\mu = 0$ case. In this model, the semiconductor wire is in trivial phase when $x < 0$, but in topological phase when $x > 0$. Majorana zero modes appear at the boundary between topological and trivial phase. To see Majorana zero modes, we express the total Hamiltonian in the Nambu spinor basis $\Psi = (c_\uparrow, c_\downarrow, c_\downarrow^\dagger, -c_\uparrow^\dagger)^T$ and neglecting the second order kinetic term $\frac{\hbar^2 k^2}{2m}$ to linearize total Hamiltonian operator as

$$\hat{H}_{\text{linear}} = -i\alpha\sigma_y\tau_z\partial_x + V_z(x)\sigma_z + \Delta\tau_x \quad (1.28)$$

Here σ and τ are Pauli matrices that correspond to spin and particle hole sectors respectively. We can diagonalize this Hamiltonian and get the wave function of zero energy modes as $e^{-ax^2/(2\alpha)}(ie^{-i\pi/4}, e^{i3\pi/4}, e^{-i3\pi/4}, ie^{i\pi/4})^T$. This wave function allows us to write the quasi particle operator at zero energy as

$$\gamma_0 = \int dx e^{-ax^2/(2\alpha)}(ie^{-i\pi/4}c_\uparrow + e^{i3\pi/4}c_\downarrow + e^{-i3\pi/4}c_\downarrow^\dagger - ie^{i\pi/4}c_\uparrow^\dagger)^T \quad (1.29)$$

One can clearly see that γ_0 is a Majorana operator that satisfied $\gamma_0 = \gamma_0^\dagger$. Furthermore, the wave package $e^{-ax^2/(2\alpha)}$ shows that the wave function of Majorana zero

modes peaks at $x = 0$ which is the phase boundary between trivial and topological phase as we predicted.

1.7 Realization of $p_x + ip_y$ superconductor in a 2D system

One can generalize the idea of having Majorana fermion in 1D spinless p-wave superconducting wire to two dimensional systems. Here we follow the derivation that is shown in ref. [18] to see this argument in an explicit way. We consider a special case where 1D p-wave wire undergoes a phase transition. From the Kitaev model, we know the phase transition of the 1D p-wave wire happens when pairing potential Δ , hopping strength t , and chemical potential μ have the same strength (i.e. $\Delta = t = -\mu$). In this case, the Hamiltonian at critical point becomes

$$H_{\text{crit}} = -\frac{i}{2}\Delta \sum_j (\gamma_{b,j}\gamma_{a,j+1} + \gamma_{b,j}\gamma_{a,j}) \quad (1.30)$$

Because the wire undergoes phase transition, this 1D system becomes gapless at this point. For this reason, we can rewrite the Hamiltonian in the basis of two counter propagating Majorana modes γ_R and γ_L in the following way:

$$\gamma_{a,j} = \gamma_{R,j} + \gamma_{L,j} \quad (1.31)$$

$$\gamma_{b,j} = \gamma_{R,j} - \gamma_{L,j} \quad (1.32)$$

The Hamiltonian in this basis becomes

$$H_{\text{crit}} = -\frac{i}{2}\Delta \sum_j (\gamma_{L,j}\gamma_{R,j} - \gamma_{L,j}\gamma_{R,j+1}) + (\gamma_{L,j}\gamma_{R,j} - \gamma_{L,j}\gamma_{R,j-1}) \quad (1.33)$$

$$-\frac{i}{2}\Delta \sum_j + (\gamma_{R,j}\gamma_{R,j+1} - \gamma_{R,j}\gamma_{R,j}) - (\gamma_{L,j}\gamma_{L,j+1} - \gamma_{L,j}\gamma_{L,j}) \quad (1.34)$$

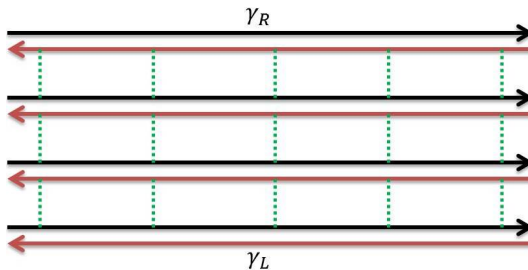


Figure 1.6: One can model a 2D p-wave superconducting film by coupling several Kiteav chains in parallel. To do that, one can first model each Kiteav chain as two counter propagating modes at a critical point, then couple two counter propagating modes in the nearest neighbor Kiteav chains. This results in two unpaired Majorana edge modes on the top and bottom edges.

In continuous model, the first two terms can be combined into a square term of momentum. The last two terms are linear in momentum, which can be expressed as

$$H_{\text{edge state}} = -\frac{i}{2}\Delta \int dx (\gamma_R \partial_x \gamma_R - \gamma_L \partial_x \gamma_L) \quad (1.35)$$

As one can see, in the lowest order of momentum, we decompose a p-wave wire into two counter propagating modes[18]. One can couple several p-wave wire in parallel to form a 2D superconducting film. To do that, we first model each individual wire as two counter propagating modes, and then we couple these propagating modes as shown in Fig.(1.6) and eq.(1.36).

$$H_{\text{p-wave bulk}} = i\epsilon \int_{\text{bulk}} dx \gamma_R \gamma_L \quad (1.36)$$

As a result, the coupling of these counter propagating modes opens a gap of ϵ in the bulk and leaves two unpaired Majorana edge modes at the top and bottom edges of this 2D p-wave superconducting film.

1.8 Fractional Josephson effect

The topological nature of the material changes the transport properties, which provides a pathway for experimentalists to reveal these exotic physics. One example

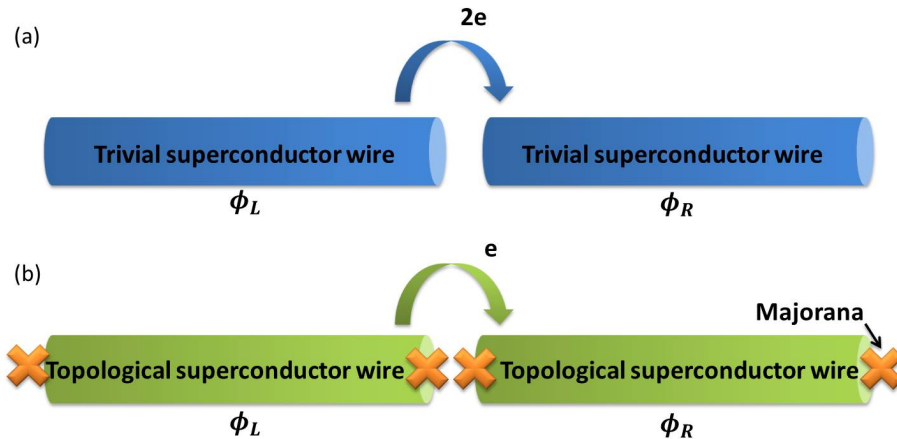


Figure 1.7: (a) A Josephson junction built by trivial superconductors. Cooper pair tunneling leads the 2π current phase relation. (b) A Josephson junction built by spinless p-wave superconducting wires. Majorana modes γ appear in the topological superconducting wires. Two Majorana modes form a single electron state in the Josephson junction, which allows single electrons to tunnel through the junction.

of this is that the Josephson relation of topological superconductors is different to trivial superconductors. In trivial superconductors, cooper pairs hop across a Josephson junction. This results in the tunneling current of a 2π periodic function of phase that crosses to the Josephson junction. Due to the fact that single electron tunneling requires breaking the Cooper pair in the usual Josephson junction, the expectation value of the single electron tunneling operator is suppressed when the energy of the BCS wave function is smaller than the pairing potential. As a comparison, fig.1.7(b) shows that two Majorana modes in topological superconductors can hybridize into single electron states in topological Josephson junction which allow single electron to tunnel across the junction. This tunneling process modifies the current phase relation of ground states into a 4π periodic function[11, 19, 20, 21, 22, 23, 24, 25, 26, 27, 28, 29, 30]. To see this, we consider a Josephson junction that is built by two spinless p-wave superconducting wires, as shown in fig.1.7(b).

We can model p-wave wires as Kitaev chain, and consider a special case where chemical potential is zero, i.e, $\mu = 0$. For simplicity, we consider hopping strength t is equal to pairing potential Δ , and denote superconducting phase at the left and

right side as $\phi_{L/R}$ in our Hamiltonian. With these conventions, we can write down the Hamiltonian of wires $H_{L,R}$ and tunneling term H_t of this Josephson junction as follows [17]

$$H_\alpha = -\frac{\Delta}{2} \sum_{x=0}^{N-1} \left[c_{\alpha,x+1}^\dagger c_{\alpha,x} + c_{\alpha,x}^\dagger c_{\alpha,x+1} + e^{i\phi_\alpha} c_{\alpha,x} c_{\alpha,x+1} + e^{-i\phi_\alpha} c_{\alpha,x+1}^\dagger c_{\alpha,x}^\dagger \right] \quad (1.37)$$

$$H_t = \Gamma \left(c_R^\dagger c_L + h.c. \right) \quad (1.38)$$

Here α is the index for left and right side of this Josephson junction. The superconducting phase $\phi_{L/R}$ can be absorbed into tunneling term by choosing the following gauge:

$$\tilde{c}_\alpha = e^{-i\phi_\alpha/2} c_\alpha \quad (1.39)$$

In this way, The Hamiltonian becomes

$$H_\alpha = -\frac{\Delta}{2} \sum_{x=0}^{N-1} \left[\tilde{c}_{\alpha,x+1}^\dagger \tilde{c}_{\alpha,x} + \tilde{c}_{\alpha,x}^\dagger \tilde{c}_{\alpha,x+1} + \left(\tilde{c}_{\alpha,x} \tilde{c}_{\alpha,x+1} + \tilde{c}_{\alpha,x+1}^\dagger \tilde{c}_{\alpha,x}^\dagger \right) \right] \quad (1.40)$$

$$H_t = \Gamma \left(e^{i(\phi_R - \phi_L)/2} \tilde{c}_R^\dagger \tilde{c}_L + h.c. \right) \quad (1.41)$$

We can diagonalize this Hamiltonian in Majorana fermions basis as shown in eq.1.4. In this way, the low energy excitation can be characterized by the tunneling term. To get eigen energy of ground states, we replace $\tilde{c}_L \rightarrow \frac{1}{2}\gamma_b$ and $\tilde{c}_R \rightarrow \frac{i}{2}\gamma_a$, and this allows us to project the tunneling term into low energy modes as

$$H_t \sim \frac{-i}{2} \Gamma \gamma_a \gamma_b \cos \left(\frac{\phi_R - \phi_L}{2} \right) = \Gamma \cos \left(\frac{\phi_R - \phi_L}{2} \right) \left(d^\dagger d - \frac{1}{2} \right) \quad (1.42)$$

Here $d = \frac{1}{2}(\gamma_b + i\gamma_a)$ is the annihilation operator of the single fermionic states that appears at the Josephson junction. As one can see from eq.(1.42), the energy of this single fermionic states is a 4π periodic function of the phase if the occupation number (parity) $d^\dagger d$ is a constant. We plot the energy phase relation in fig.1.8(a) for the parity conserved case. Due to thermal fluctuation and quasi particle poisoning, the

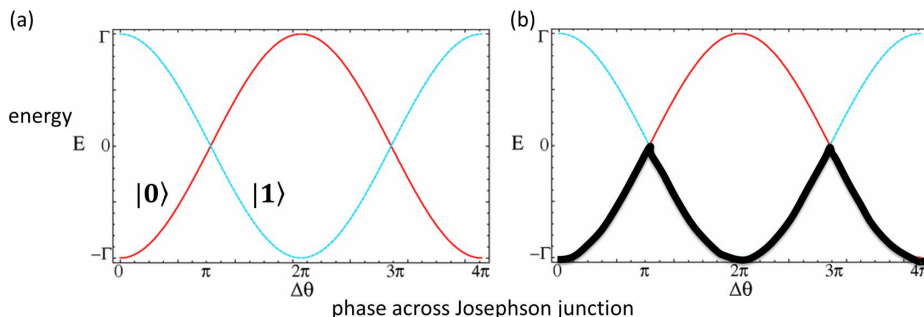


Figure 1.8: Fractional Josephson effect. (a) When parity is conserved in the Josephson junction, the energy is a 4π periodic function of phase. (b) When parity is allowed to fluctuate, the system will choose parity to minimize the energy, which results in energy phase relation becoming a 2π periodic function.

occupation number of the single fermionic states in a Josephson junction may fluctuate when the superconducting phase starts to wind. Once parity is not conserved, the system will choose the parity which minimize energy. In this case, the ground state energy phase relation becomes a 2π periodic function, as shown by the black curve in fig.(1.8)(b). The 2π energy phase relation causes confusion in experimental read out, because once parity of a Josephson junction is allowed to fluctuate, we cannot distinguish the difference between topological and trivial superconductor by measuring the periodicity of current phase relation. To solve this difficulty, we propose using the signature of multiple critical currents and nonvanished critical current as features to identify the existence of topological superconductivity. The details of this proposal are illustrated in chapter 3.

Since p-wave superconductivity can be realized by coupling edge states and superconductivity, we would expect that fractional Josephson effect would also appear if we build a Josephson junction on top of two counter propagating edge states of a 2D topological insulator, as shown in Fig.1.9. We can model the Hamiltonian of Fig.1.9 in the following way:

$$H = (\psi_R^\dagger(x), \psi_L(x)) \begin{pmatrix} -iv\partial_x & \Delta^*(x) \\ \Delta(x) & iv\partial_x \end{pmatrix} \begin{pmatrix} \psi_R(x) \\ \psi_L^\dagger(x) \end{pmatrix}$$

Here we model the pairing potential of this Josephson junction as:

$$\Delta(x) = \begin{cases} \Delta_0 & \text{if } x < 0 \\ \Delta_0 e^{i\varphi} & \text{if } x > 0 \end{cases} \quad (1.43)$$

We can diagonalize this Hamiltonian in the energy eigen basis Γ_E as $H = \sum_E E \Gamma_E^\dagger \Gamma_E$. In particular, the bound states of a Josephson junction at $x < 0$ have the following form:

$$\Psi(x < 0) = \begin{pmatrix} \psi_R(x) \\ \psi_L^\dagger(x) \end{pmatrix} = e^{\xi x} \begin{pmatrix} a \\ b \end{pmatrix} \Gamma_E = \Phi_E \Gamma_E \quad (1.44)$$

Solving the eigenfunction $H\Phi_E = E\Phi_E$, we get decay length as:

$$\frac{1}{\xi} = \frac{v}{\sqrt{\Delta_0^2 - E^2}} \quad (1.45)$$

and wavefunction Φ_E as

$$e^{\xi x} \begin{pmatrix} a \\ b \end{pmatrix} = e^{\xi x} \begin{pmatrix} \frac{E}{\Delta_0} - i \frac{\sqrt{\Delta_0^2 - E^2}}{\Delta_0} \\ 1 \end{pmatrix} \quad (1.46)$$

To shorten the notation, let's denote

$$\cos(\theta) = E/\Delta_0 \quad (1.47)$$

$$\sin(\theta) = \sqrt{\Delta_0^2 - E^2}/\Delta_0 \quad (1.48)$$

In this way the wave function at $x < 0$ can be written as:

$$\Phi_E(x < 0) = e^{\xi x} \begin{pmatrix} e^{-i\theta} \\ 1 \end{pmatrix} \quad (1.49)$$

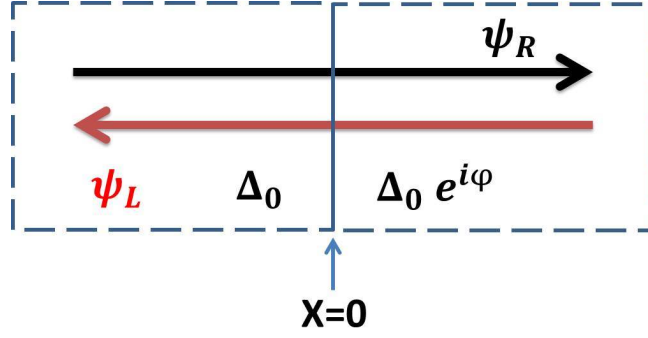


Figure 1.9: Josephson junction is built on top of helical edge states. $x = 0$ is the location of the interface.

By similar argument, we can argue that the wave function at $x > 0$ is

$$\Phi_E(x > 0) = e^{-\xi x} \begin{pmatrix} e^{i\theta - i\varphi} \\ 1 \end{pmatrix} \quad (1.50)$$

Matching the boundary condition of wavefunctions at junction $x = 0$, we get

$$\Phi_E(x < 0)|_{x=0} = \Phi_E(x > 0)|_{x=0} \rightarrow \begin{pmatrix} e^{i\theta - i\varphi} \\ 1 \end{pmatrix} = \begin{pmatrix} e^{-i\theta} \\ 1 \end{pmatrix}$$

This gives

$$\theta = \varphi/2 + n\pi \quad n \text{ is an integer} \quad (1.51)$$

Taking cos on both sides of eq.(1.51) and using the definition of $\cos(\theta)$ in eq.(1.47), we get:

$$\frac{E}{\Delta_0} = \cos(\theta) = (-1)^n \cos\left(\frac{\varphi}{2}\right) \quad (1.52)$$

Taking derivative of this energy phase relation gives us current-phase relation as following:

$$I = \frac{2e}{\hbar} \frac{\partial E}{\partial \varphi} \propto \pm \sin(\varphi/2) \quad (1.53)$$

The \pm sign is determined by the parity of the Josephson junction, as we illustrated before. The current phase relation with 4π periodicity is one of the signatures of topological superconductors. We can generalize this detection scheme in the 2D system by building a long Josephson junction. In this way, we can measure the periodicity of critical current as a function of flux through the junction. This provides signatures of 2D topological superconductors. We illustrate this idea in detail in chapter 3 and 5.

1.9 Tunneling spectroscopy of Majorana zero modes

Apart from using fractional Josephson effects, one can use tunneling spectroscopy to reveal the existence of Majorana zero modes. The idea is that tunneling current resonant with Majorana zero energy modes at zero bias voltage, which gives the conductance peak at zero voltage[31, 32, 33, 34]. To verify this, let's calculate the tunneling current between a tip to a spinless p-wave superconducting wire. We model the system similar to the one in ref. [35]. As shown in fig.(1.10), the electrons at the tips couple the Majorana zero modes that appear at the end of the topological superconductor.



Figure 1.10: One can reveal Majorana zero modes by using tunneling spectroscopy on a topological superconducting wire.

To calculate the conductance of this tunneling process, we can model the electrons on the tip as a chiral field ψ , which couples to Majorana zero modes γ_1 as shown in fig.(1.11).

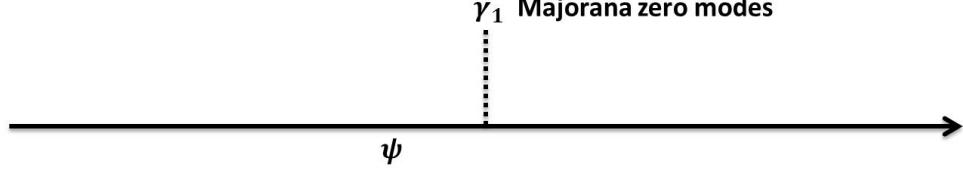


Figure 1.11: One can model the tunneling of an electron to Majorana zero modes that is shown in fig.(1.10) as a chiral field ψ couples to a Majorana zero mode γ_1 .

The electrons on the tip can be modeled as

$$H_e = -iv \int_{-\infty}^{\infty} dx \psi^\dagger \partial_x \psi \quad (1.54)$$

Meanwhile, the coupling between electron and Majorana fermions can be written as

$$\delta H = \frac{t}{\sqrt{2}} \int_{-\infty}^{\infty} dx \gamma_1 (\psi^\dagger - \psi) \delta(x) \quad (1.55)$$

In order to calculate scattering matrix, we rewrite the Majorana fermion γ_1 in the Dirac fermion basis f as $\gamma_1 = (f + f^\dagger)$. In this way, we can write the total Hamiltonian on the basis of $\Psi^\dagger = (\psi^\dagger, \psi, f^\dagger, f)$ as

$$H_{\text{total}} = H_e + \delta H = \frac{1}{2} \int_{-\infty}^{\infty} dx \Psi^\dagger \mathcal{H} \Psi \quad (1.56)$$

$$\mathcal{H} = \begin{pmatrix} -iv\partial_x & 0 & \frac{-t}{\sqrt{2}}\delta(x) & \frac{-t}{\sqrt{2}}\delta(x) \\ 0 & -iv\partial_x & \frac{t}{\sqrt{2}}\delta(x) & \frac{t}{\sqrt{2}}\delta(x) \\ \frac{-t}{\sqrt{2}}\delta(x) & \frac{t}{\sqrt{2}}\delta(x) & 0 & 0 \\ \frac{-t}{\sqrt{2}}\delta(x) & \frac{t}{\sqrt{2}}\delta(x) & 0 & 0 \end{pmatrix} \quad (1.57)$$

The scattering matrix can be calculated in the following way. We first assume that

the incoming wave $\phi_E(x < 0)$ and outgoing wave $\phi_E(x > 0)$ have the following form:

$$\phi_E(x < 0) = \begin{pmatrix} e^{iEx/v} a_E^< \\ e^{iEx/v} b_E^< \\ c_E \\ d_E \end{pmatrix} \quad (1.58)$$

$$\phi_E(x > 0) = \begin{pmatrix} e^{iEx/v} a_E^> \\ e^{iEx/v} b_E^> \\ c_E \\ d_E \end{pmatrix} \quad (1.59)$$

We then apply eigen equation $\mathcal{H}\phi_E = E\phi_E$ to get the relation between incoming wave and outgoing wave:

$$-iv(a_E^> - a_E^<) = \frac{t}{\sqrt{2}}(c_E + d_E) \quad (1.60)$$

$$-iv(b_E^> - b_E^<) = \frac{-t}{\sqrt{2}}(c_E + d_E) \quad (1.61)$$

$$\frac{-t}{\sqrt{2}} \left(\frac{a_E^> + a_E^<}{2} - \frac{b_E^> + b_E^<}{2} \right) = Ec_E \quad (1.62)$$

$$\frac{-t}{\sqrt{2}} \left(\frac{a_E^> + a_E^<}{2} - \frac{b_E^> + b_E^<}{2} \right) = Ed_E \quad (1.63)$$

Solving the above equations gives us the scattering matrix S as follows:

$$a_E^> = S_{ee}a_E^< + S_{eh}b_E^< = \frac{Ev}{Ev + it^2}a_E^< + \frac{it^2}{Ev + it^2}b_E^< \quad (1.64)$$

The tunneling conductance G comes from the channels where electrons scatter into holes. For this reason, we can calculate conductance $G(E)$ as

$$G(E) = \frac{2e^2}{h} |S_{eh}|^2 = \frac{2e^2}{h} \frac{t^4}{(Ev)^2 + t^4} \quad (1.65)$$

The factor of two in the formula of conductance comes from the process of an electron in the tip scattered back as a hole, which results in a cooper pair tunneling to the superconductor. This formula also shows that electrons at the tip have perfect Andreev reflection at zero voltage ($V = 0$), which leads to the conductance peaks at zero voltage ($E = eV = 0$). As we will show in next section, the zero bias peak has been experimentally reported as the possible signature of Majorana zero modes by several experimental groups in various systems.

1.10 Experimental progress on topological superconductors

As shown in fig.(1.12)(a), experimental group lead by Prof. Leo Kouwenhoven reported zero bias peak of conductance in a superconductor coupled InSb nanowire[36].

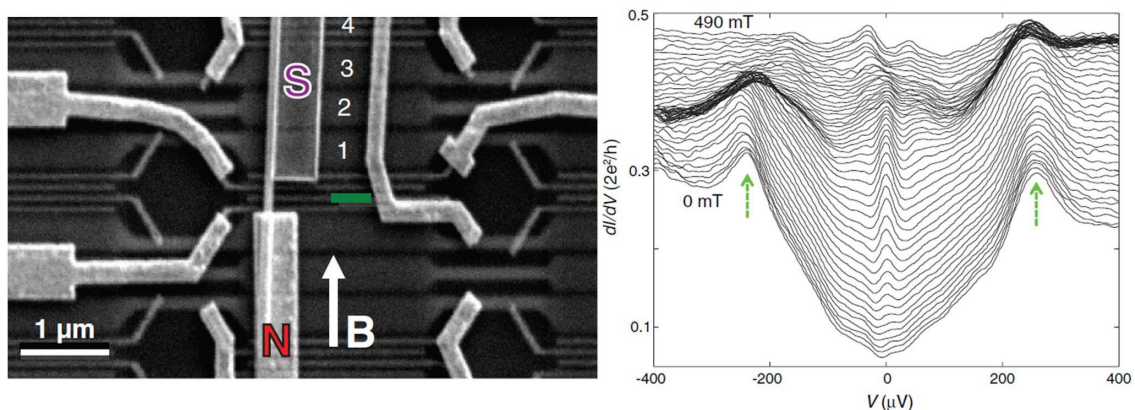


Figure 1.12: (a) The superconductor coupled InSb nanowire for probing Majorana zero modes. (b) Zero bias peak arises when Zeeman field is large, which may indicate the existence of Majorana zero modes. Figures originate from V. Mourik *et. al.* Science 336, 1003 (2012).

The conductance of this device peaks at zero voltage when the magnetic field is strong enough, as indicated in fig.(1.12)(b). One possible explanation of this zero bias peak is the appearance of Majorana zero modes. As we have shown in section 1.3, the topological phase arises when Zeeman field larger than both the induced pairing

potential Δ and the chemical potential μ as $V_z > \sqrt{\Delta^2 + \mu^2}$. Devices built on InAs nanowires also reported zero bias peaks with similar magnetic response [37]. Although the magnetic response of this zero bias peak can be explained as the signature of Majorana zero modes, other sources such as disorders or impurities may also arise from similar features. To provide more unambiguous evidence for Majorana zero modes, experimentalists have used a scanning tunneling microscope to resolve the real space wavefunction of zero energy modes[38]. Fig. 1.13(a) shows the schematic setup built by the group of Prof. Ali Yazdani. They placed ferromagnet (iron) atoms on top of superconducting lead (Pb), and used a scanning tunneling microscope to map the local density of state by varying voltage, as shown in Fig. (1.13)(b).

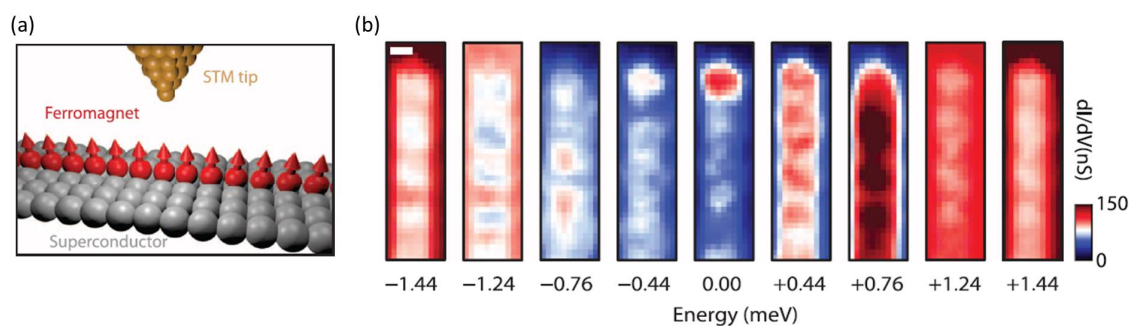


Figure 1.13: (a) Iron atoms placed in a superconducting film. (b) Local density of states scanned by scanned tunneling microscope. The local density of states indeed peak at the end of iron wire at zero energy. Figures originate from Stevan Nadj-Perge *et. al.* Science 346, 6209 (2014).

As one can see in fig.1.13(b), the local density of state peak at the end of the iron chain at zero voltage, which is consistent with the theory prediction of the location of Majorana zero modes.

Since Majorana zero modes are hosted by topological superconductors, we want to know if there is any way to directly identify topological superconductors other than by Majorana zero modes. The motivation of direct probing topological superconductor is the following: Majorana zero modes require the time reversal broken system to appear, while topological superconductors can be induced in both time reversal

broken and invariant systems. To find the signature of topological superconductors, superconductors coupled to topological insulators provide a promising platform to reveal topological superconductivity. Experimentalists have shown proximity induced superconductivity in both HgTe [39, 40, 41, 42, 43] and InAs/GaSb [44, 45, 46, 47] quantum wells.

Fig.(1.14)(a) is the device built by group of Prof. Amir Yacoby[2]. They built a long Josephson junction on top of a HgTe quantum well—which is a 2D topological insulator. As proximity induced pairing potential couples the left and right moving edge states, the edge states transform into an effective 1D spinless p-wave wire. In this experiment, they measure the resistivity as a function of flux and applied current, as shown in Fig.(1.14)(b). By inverse Fourier transforming the interference pattern of this resistivity map, they decode the supercurrent density distribution in real space as shown in Fig.(1.14)(c). From this supercurrent density distribution, one could clearly see that the super current indeed flows through the edges of quantum well as predicted. Similar super current density distribution was also found in InAs/GaSb quantum well by group of Prof. Leo Kouwenhoven [9].

The question is, if topological superconductivity indeed appears in such systems, how do we identify it? In the following chapters, we will address this question in great detail.

1.11 Outline of this thesis

We first analyze what happens when a superconductor is coupled to the bulk of a 2D topological insulator in Chapter 2. We surprisingly find that due to work function mismatch between a superconductor and a 2D topological insulator, the superconductor dopes the 2D topological insulator, which leads to edge state relocation. Once this happens, one can engineer these relocated edge states to form a network for braiding Majorana fermions. This provides a pathway toward quantum computation.

Chapter 3 appeared as Phys. Rev. Lett. 113, 197001 (2014). In this chapter, we discuss how to use Josephson junction that is built on top of a 2D topological insulator

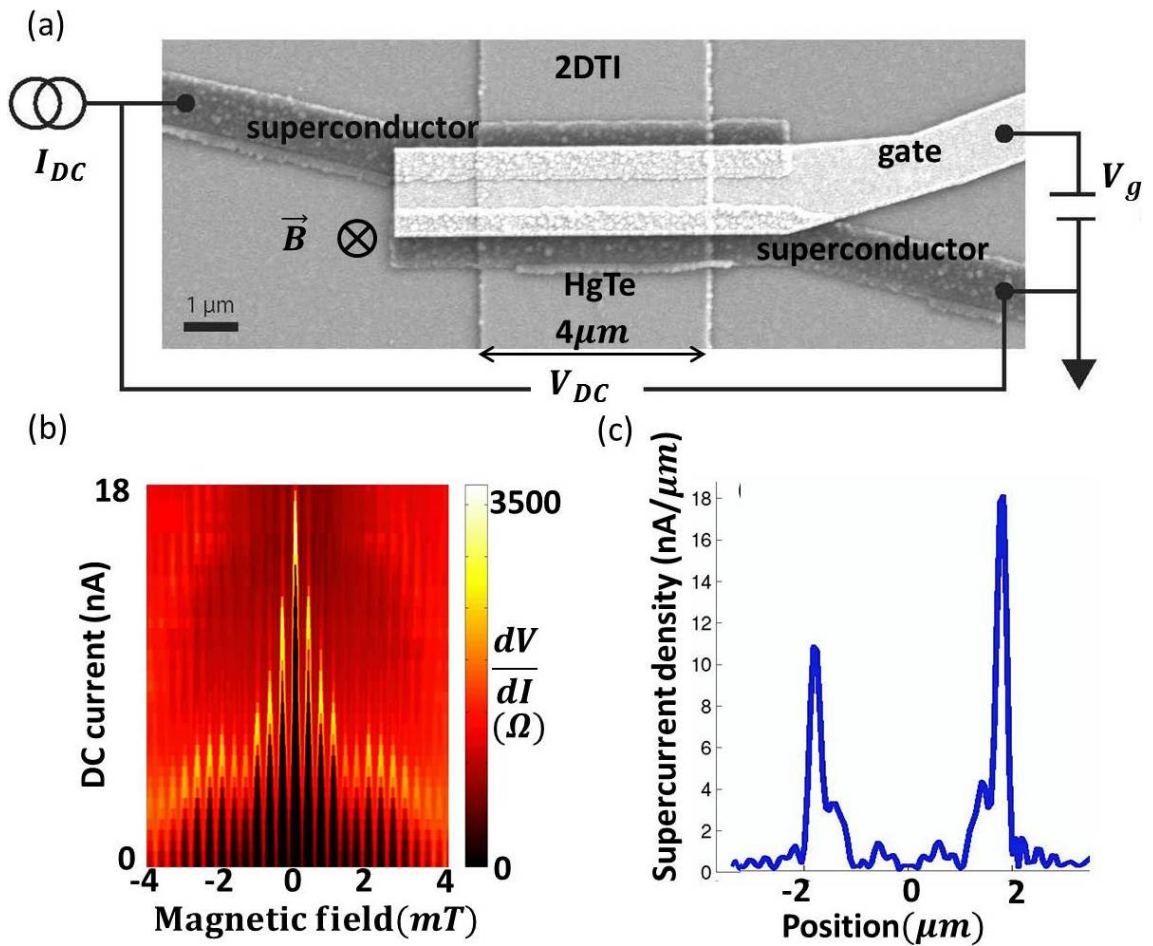


Figure 1.14: (a) A long Josephson junction built on top of HgTe quantum well. (b) The interference pattern of conductance. One can inverse Fourier transform this interference pattern to get the current density distribution in real space as shown in (c). The current density distribution in fig.(c) shows that the super current indeed flows along the edge of the HgTe quantum well. Figures originate from Sean Hart *et. al.* Nature Physics 10, 638643 (2014).

to probe topological superconductivity. To compare our calculation with experimental data from ref.[2] and [9], we consider the same geometry that has been probed by the experimentalists. In particular, we address the issue of when quasi-particle poisoning and thermal fluctuation destroy parity conservation of the Josephson junction, what other alternative signatures apart from the fractional Josephson effect can we look for to identify topological superconductors. We show that multiple critical currents and nonvanish critical currents for all magnetic field may be the alternative signature of topological superconductor in this scenario. The system becomes more interesting as interactions come into play.

Chapter 4 is working in progress. We show that once interactions appear in the edge states, some exotic low energy excitations such as parafermions appear at the ends of topological superconducting region. Apart from that, interactions provide universal conductance quantization that allows one to distinguish between trivial and topological superconductor.

Chapter 5 appeared as *Phys. Rev. Lett.* 109, 126403 (2012). We propose an interdigitated superconductor-ferromagnet structure to engineer topological superconductivity. One advantage of this structure is that both pairing potential and Zeeman splitting can be induced from a single interface, which allows one to induce topological phase in a wider class of a 2D electron gas including the surface state of bulk InSb. This structure allows one to engineer a vortex to trap Majorana zero modes, which provides a feasible way to electrically manipulate Majorana modes. At the end of the chapter, we provide an interference pattern for topological superconductor that is widely applicable in any 2D system.

Chapter 2

Dynamical manipulation of 2D topological insulator edge states for Majorana fermion braiding

2.1 Introduction

Majorana fermions have recently drawn much attention due to their potential for building topologically protected qubits for quantum computation[48]. Several theoretical works predict that such exotic physics might be found in p-wave superconductors[49, 50, 51], semiconductor-superconductor heterostructures[52, 53], and topological insulators with proximity induced superconductivity[54]. These theoretical predictions inspired several experimental groups to find signatures of Majorana fermions[55, 56, 57].

Two dimensional topological insulators such as HgTe quantum wells [58, 59, 60] are one of the promising platforms to realize Majorana fermions [61]. One can realize Majorana fermions in such a system by coupling the counter propagating chiral edge states to a s-wave superconductor [61]. In this way, the proximity induced superconductivity couples the left-moving and right-moving edge states and transforms the edge states into an effective 1D spinless p-wave superconducting chain[17]. The Majorana fermions appear at the ends of this chain [50] if we break time reversal symmetry by coupling to a ferromagnet [62].

2.2 Relocated edge states

Since braiding Majorana fermions is an essential ingredient for topological quantum computation, one can exchange two Majorana fermions in 2D topological insulators by building a corner junction[63, 17, 64, 65]. However, physically etching a corner junction may induce defects to a quantum well and limit the braiding process to be performed along the perimeter. To overcome these difficulties, we introduce a new scheme to relocate the edge states into the bulk while 2DEG remains intact. Arranging these edge states to a checkerboard structure allows one to fabricate a network for braiding Majorana fermions on a single quantum well. Manipulations of Majorana fermions can therefore be performed on these relocated edge states by gates adjacent to the superconductor. This provides a way to circumvent the screening effect that comes from superconductivity.

Figure 2.1 (a) demonstrates the concept of relocating edge states into the bulk of a quantum well. As we bring an s-wave superconductor on top of a HgTe quantum well, the carriers diffuse from superconductor to HgTe due to the mismatch of work functions. As a result, the superconductor dopes part of the quantum well. If the doping level is sufficiently large enough that the chemical potential μ_{SC} on the superconducting side is deep in the bulk band as shown in Fig. 2.1 (c), the wave function of HgTe on the superconducting side becomes insensitive to the mass gap because the Fermi surface is energetically far away from the gap. This allows us to flip the sign of the mass term on superconducting side without affecting the HgTe wavefunction. Therefore, this part of HgTe enters a trivial phase. The edge states appear at the crossover between topological (non-superconducting) and trivial (superconducting) regions [66] as shown in Figure 2.1.

These relocated edge states form gapped Andreev bound states along the junction by coupling to the superconductor. Here we numerically demonstrate that Andreev bound states appear as soon as the superconductor dopes the Fermi surface into the bulk band. We use four band model to describe the Hamiltonian of HgTe[58, 59] in

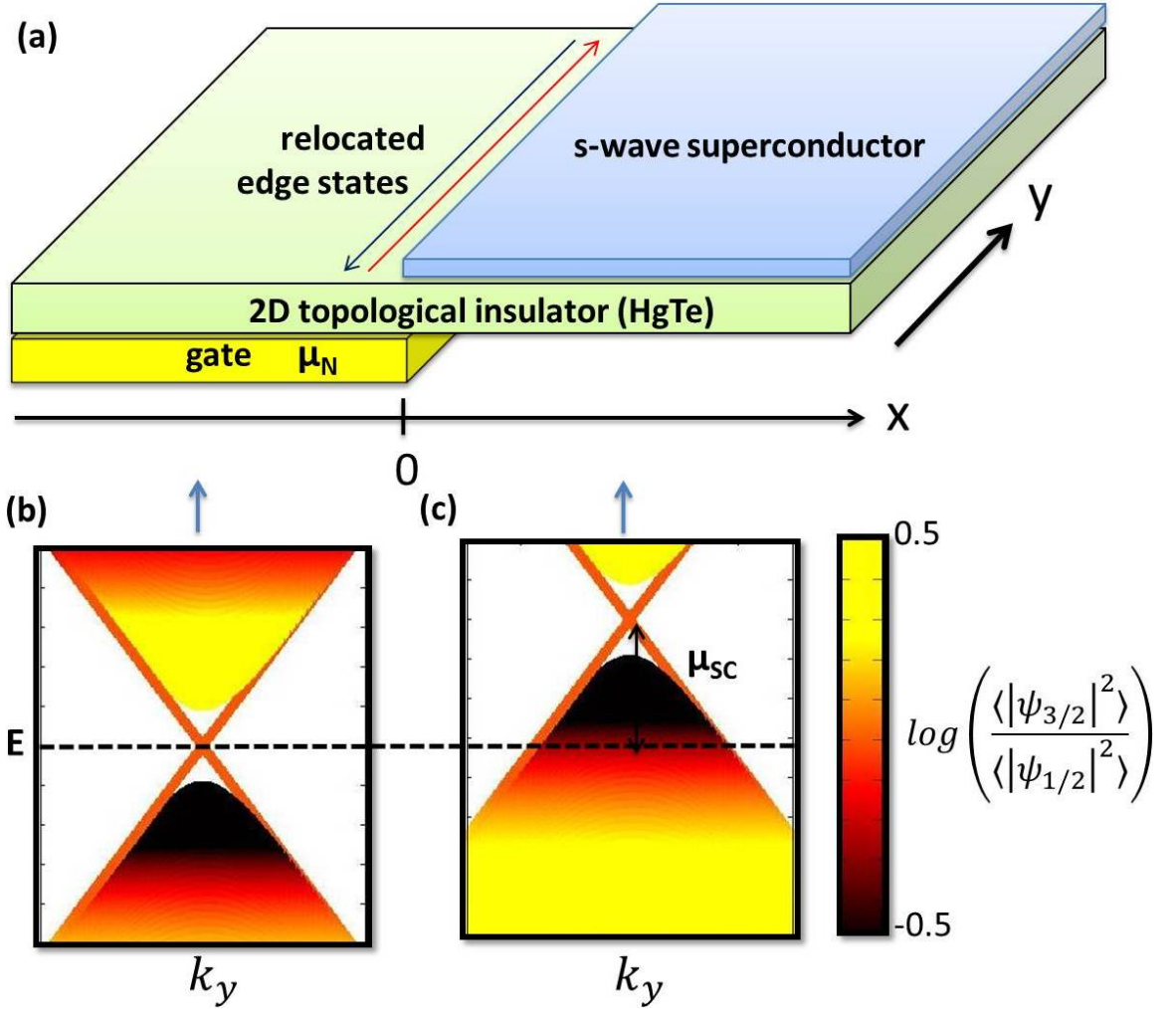


Figure 2.1: (a) The s-wave superconductor dopes the HgTe quantum well underneath it due to the work function mismatch. The relocated edge states appear along the junction between the superconducting and non-superconducting part if the superconductor dopes the HgTe underneath it deeply into its valence band. (b) The band structure of HgTe at normal region. We use a gate to control the chemical potential at this side such that chemical potential μ_N is confined within the mass term bulk gap. (c) Superconductor dopes HgTe because of the work function mismatch. This gives the shifts of the chemical potential μ_{SC} in band structure. Color code is the ratio between angular momentum the $\pm 3/2$ and $\pm 1/2$ part of wavefunctions.

the total angular momentum basis $\Psi^\dagger = (\psi_{1/2}^\dagger, \psi_{3/2}^\dagger, \psi_{-1/2}^\dagger, \psi_{-3/2}^\dagger)$ as

$$H_{\text{HgTe}} = \Psi^\dagger(\vec{k}) \begin{pmatrix} h(\vec{k}) & 0 \\ 0 & h^*(-\vec{k}) \end{pmatrix} \Psi(\vec{k}) \quad (2.1)$$

where

$$h(\vec{k}) = (\mu - D\vec{k}^2)I + Ak_x\sigma_x + Ak_y\sigma_y + (M - B\vec{k}^2)\sigma_z \quad (2.2)$$

and σ are Pauli matrices corresponding to total angular momentum (1/2 and 3/2), and μ is the chemical potential. $A\vec{k}$ is the spin orbital coupling that couples the angular momentum 1/2 and 3/2 bands. The HgTe quantum well enters the topological phase upon band inversion happens. This requires the mass term M to satisfy $M/B > 0$. In Table I, we quote experimentally fitted parameters[58] in our numerical simulations.

A (eV nm)	B (eV nm ²)	M (eV)	D (eV nm ²)	g
0.364	-0.686	-0.01	-0.512	-20.5

Table 2.1: The values of parameters including spin orbital coupling A , and mass term M and the g-factor g of HgTe quantum wells have been given above [58].

The carriers that diffusing from superconductor to HgTe dope the quantum well and give the proximity induced pairing term as:

$$H_{\text{SC}} = \Delta \left[\psi_{\frac{1}{2}}(\vec{k})\psi_{-\frac{1}{2}}(-\vec{k}) + \psi_{\frac{3}{2}}(\vec{k})\psi_{-\frac{3}{2}}(-\vec{k}) \right] + h.c.$$

With this pairing term in hand, we can calculate the required doping level and gaps size by diagonalization of the total Hamiltonian. The black solid curve and red dashed curve in Figure 2.2(a) are the bulk gap and gap of relocated edge states as functions of doping level respectively. The corresponding wavefunction of the red dashed curve in (b) verifies that the relocated edge states indeed appear along the junction. The red dashed curve in Figure 2.2(a) demonstrates that relocated edge states appear as soon as the superconductor dopes chemical potential μ_{SC} into bulk band. We note that Andreev spectroscopy between normal and superconductor doped HgTe quantum

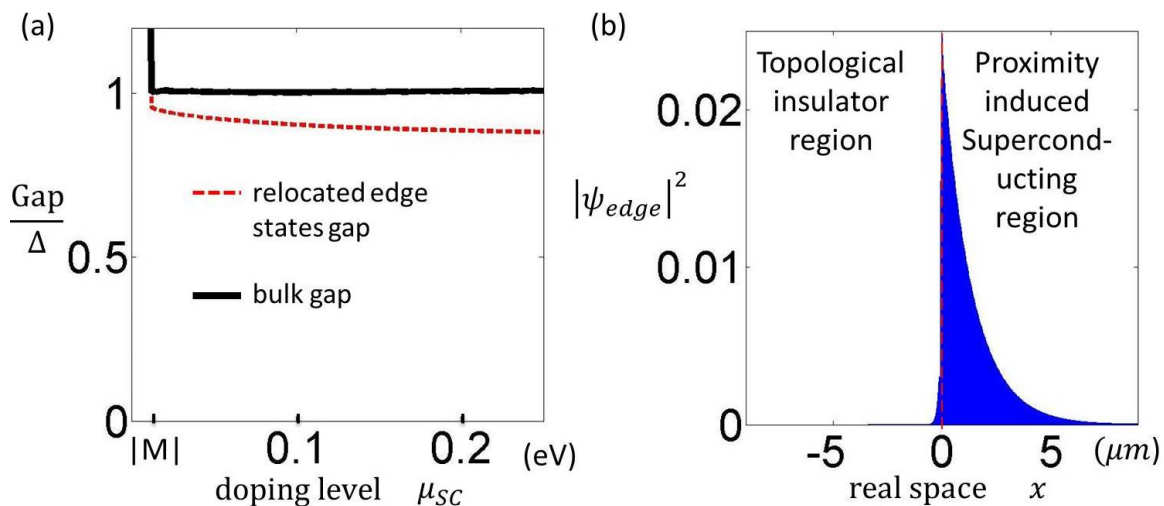


Figure 2.2: (a) Gap of the device shown Fig. 2.1 versus the doping level μ_{SC} of HgTe at superconducting side. The black solid lines and red dashed line are the bulk gap and the gap of relocated edge states, respectively. The Relocated edge states appear as soon as the superconductor dopes the HgTe such that chemical potential at superconducting side enters the bulk band $|M|$. (b) The probability distribution of relocated edge states in real space indicates that the position of relocated edge states indeed appears along the junction that consists with Figure 2.1 (a). x is the direction in real space shown in Figure 2.1 (a).

wells was studied by M. Guigou *et al.*[67].

Majorana fermions appear in the system after we break time reversal symmetry. We can achieve this goal by applying an in-plane magnetic field B_x . However, the Zeeman field induced by in-plane magnetic field may destroy the proximity induced superconductivity. Surprisingly, this problem can be overcome if we heavily hole dope HgTe. This comes from the fact that Zeeman field only couples angular momentum $1/2$ and $-1/2$ part of the wavefunctions. As chemical potential goes deeply into valence band, the HgTe wavefunctions become dominated by the angular momentum $\pm 3/2$ part of the components; therefore, they are insensitive to in-plane magnetic field. This allows proximity-induced superconductivity to survive under Zeeman field. Here we calculate the band structure of HgTe with Zeeman splitting to illustrate this idea in great detail.

We model the in-plane magnetic field that couples angular momentum $1/2$ and

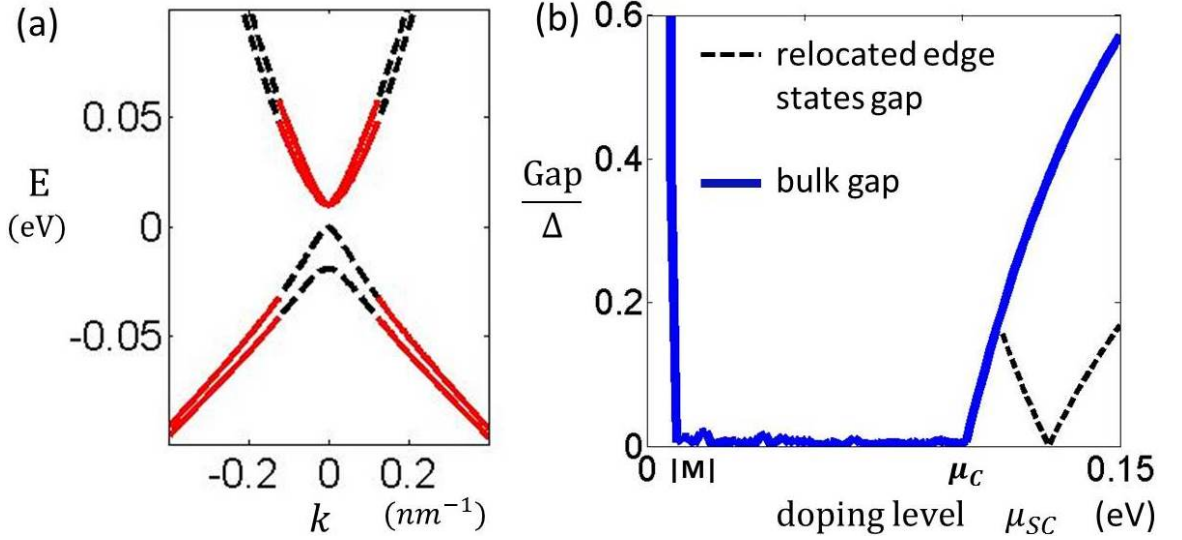


Figure 2.3: (a) Bulk band of HgTe quantum well with Zeeman splitting induced by in-plane magnetic field B_x . Red solid curves and black dashed curves are the bands with wavefunctions dominated by angular momentum $\pm 3/2$ and $\pm 1/2$ part, respectively. The Zeeman splitting in the valence band gradually vanishes as one heavily hole dopes the HgTe quantum well such that the Fermi surface goes deeply into the valence band. (b) Gap of the device shown Fig. 2.1 as function of the doping level μ_{SC} in the superconducting side. The blue solid line and a black dashed line are the bulk gap and the gap of relocated edge states, respectively. In this simulation we use 2 Tesla in-plane magnetic fields and 4 Kelvin induced superconducting gaps Δ . The bulk gap closes for doping levels is larger than mass term gap $|M|$ and is reopened by proximity induced superconductivity when doping level larger than critical doping level μ_c . The relocated edge states appear after the bulk gap is reopened. The gap closing of black dashed line indicates the phase transition of relocated edge states being gapped by the Zeeman field to superconductivity.

$-1/2$ part of the wavefunctions as:

$$H_{\text{Zeeman}} = g\mu_B B_x \psi_{-1/2}^\dagger(\vec{k}) \psi_{1/2}(\vec{k}) + h.c. \quad (2.3)$$

Here g denotes g-factor of HgTe and μ_B is the Bohr magneton. Diagonalization of total Hamiltonian $H_{\text{HgTe}} + H_{\text{Zeeman}}$ gives the valence band dispersion with Zeeman splitting shown in Fig. 2.3(a) and the following equation:

$$E_{\pm\frac{3}{2}}(\vec{k}) = \mu - D\vec{k}^2 \pm \frac{V_z}{2} - \sqrt{A^2\vec{k}^2 + \left(B\vec{k}^2 - M \mp \frac{V_z}{2}\right)^2}$$

The red solid lines and black dashed lines in Fig. 2.3(a) are the bands dominated by total angular momentum $\pm 3/2$ and $\pm 1/2$ part of wavefunctions, respectively. One remarkable feature of these band structures is that the Zeeman splitting becomes smaller as we move the chemical potential deeper into valence bands. The Zeeman splitting at Fermi momentum \vec{k}_f between valence bands will eventually be smaller than the proximity-induced pairing potential as we increase the hole doping level.

$$E_{\frac{3}{2}}(\vec{k}_f) - E_{\frac{-3}{2}}(\vec{k}_f) < 2\Delta \quad (2.4)$$

This property allows us to calculate the critical doping level μ_c , where the proximity induced superconducting gap is opened under Zeeman field $V_x = g\mu_B B_x$.

$$\mu_c \approx \frac{A^2(D - B)|V_x|}{4B^2\Delta}$$

We plot the gaps as a function of doping level in Fig. 2.3(b) to emphasize the importance of *hole* doping for superconductivity to survive under Zeeman field. The HgTe quantum well is gapped by the mass term at zero doping level. As we tune up the doping level, the Fermi surface μ_{SC} at superconducting side of HgTe goes into the angular momentum $\pm 1/2$ part of the valence band, as shown with the dashed line in Fig. 2.3(a). The system goes into a metallic state if the Zeeman splitting V_z is greater than the proximity induced pairing potential Δ , and this gives the gapless

region shown in Fig. 2.3(b). As the doping level at superconducting side of HgTe is increased up to critical doping level, the chemical potential goes into the angular momentum $\pm 3/2$ part of valence band. This allows the proximity effect to open the superconducting gap even under Zeeman field.

Relocated edge states appear along the junction in Fig. 2.1(a) when the bulk band is gapped by the proximity induced superconductivity, as shown with the black dashed curves in Fig. 2.3(b). The gap closing of black dashed curves in Fig. 2.3(b) indicates the phase transition of the relocated edge states from being gapped by the Zeeman field to proximity induced superconductivity. We can use this phase transition to shuttle the Majorana fermions along the relocated edge states via gating. The Majorana zero modes appear at the ends of relocated edge states in Fig. 2.1(a) once we break the time reversal symmetry[17] by applying an in-plane magnetic field. These locations are the domain walls of edge states where the gaps switch from superconducting gap to Zeeman gap. We can move Majorana zero modes along the relocated edge state by adjusting the locations of domain walls for braiding purpose. One way to do that is by putting side gates adjacent to the superconductor for tuning the chemical potential μ_N at normal region as shown in Fig. 2.5(a) and Fig. 2.1 (a). As we varying the side gate voltage locally, the gap of relocated edge states change between Zeeman gap and superconducting gap accordingly. This allows one to dynamically move around the domain wall and hence manipulate the Majorana fermions. We give the phase diagram of relocated edge states in Fig. 4.2 to illustrate this idea in more detail.

2.3 Phase diagram of relocated edge states

Fig. 4.2 is the phase diagram of the device in Fig. 2.1 (a) under an in-plane magnetic field. The HgTe quantum well goes from topological to metallic and then enters the superconducting phase as we increase the doping level μ_{SC} at the superconducting side. Two distinct phases of relocated edge states emerge at the superconducting phase as superconductor dopes HgTe higher than critical doping level. One corre-

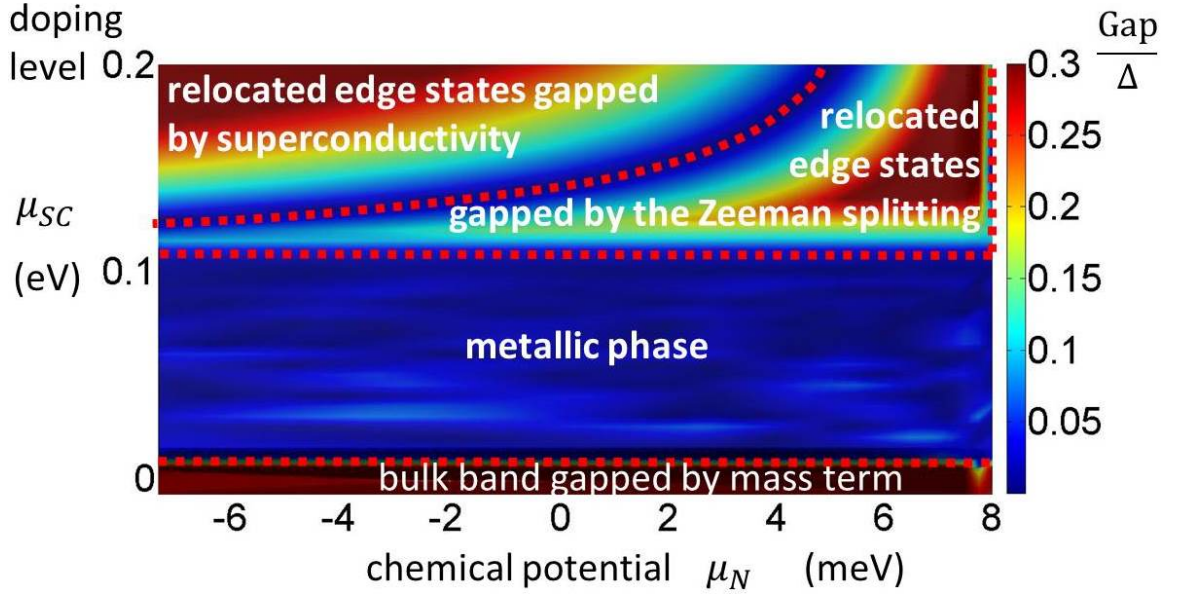


Figure 2.4: Phase diagram of the device shown in Fig. 2.1(a). Vertical axis μ_{SC} corresponds to the doping level at superconducting side of the quantum well. Horizontal axis μ_N corresponds to the chemical potential that is tuned by the side gate voltage at the non-superconducting side of the device. The color code corresponds to the minimum gap of the device. We normalize it with induced pairing potential. Red dashed lines are phase boundaries. The parameters used are induced pairing potential $\Delta = 0.4$ (meV), in-plane magnetic field 2 Tesla, and the coefficients of HgTe quantum well are shown in Table I [58].

sponds to the relocated edge states gapped by Zeeman field in contrast to the other one gapped by superconductivity. The closing of the gap marks the phase boundary between these two phases in Fig. 4.2.

As one can see from the phase diagram, for a fixed doping level μ_{SC} on the superconducting side, we can actually switch the gap of the relocated edge states from being gapped by induced superconductivity to Zeeman field by tuning up the side gate voltage μ_N at non-superconducting part of HgTe in Fig. 2.1(a). The domain walls of gaps can therefore be created on relocated edge states if we locally varying side gate voltage. This provides one a scheme to dynamically manipulate the positions of Majorana fermions that are not restricted on the perimeter of a quantum well but also along the relocated edge state which is interior of a quantum well.

To demonstrate how this works, we present the numerical simulation in Fig. 2.5. First of all, we assume that the superconductor hole dopes the HgTe larger than the critical doping level μ_c , so that the HgTe underneath the superconductor is gapped by a proximity-induced gap. The relocated edge states therefore appear at the junction between superconducting and non-superconducting part of HgTe quantum well in Fig. 2.5(a) and Fig. 2.1(a). We then apply the side gate voltage μ_N on the relocated edge states according to the phase diagram shown in Fig. 4.2. We use the side gate μ_2 to gate the parts of the relocated edge states such that they are gapped by the Zeeman gap. Then we tune the side gates voltage μ_1 such that the relocated edge states underneath them are gapped by proximity-induced superconductivity. In this way, we create domain walls between two different type of gaps as one walks from gate μ_1 to μ_2 in real space. The Majorana zero modes appear on the domain walls as illustrated in Fig. 2.5(a). Fig. 2.5(c) shows the energy levels that are derived from diagonalization of the Hamiltonian of the device in Fig. 2.5(a) in 2D real space with open boundary condition. Zero energy modes appearing in the spectrum indicate the presence of Majorana fermions in this system. The peaks of zero mode wavefunction in Fig. 2.5(b) demonstrate the locations of Majorana fermions in 2D real space. These locations are consistent with the argument that we illustrate in Fig. 2.5(a) regarding the Majorana zero modes appear at the domain wall, where we use gates to switch

the gap of relocated edge states between the Zeeman gap and the superconducting gap.

2.4 Network of relocated edge states for braiding

Two objects will inevitably collide to each other if one tries to exchange them in a 1D system. We can overcome this problem by using two wires to form a T-junction [63] or a “crossing”-junction [17]. Here we provide an experimentally feasible way to mimic the “crossing”-junction by using the relocated edge states to form the corner junctions, as shown in Fig. 2.6(a). The corner junctions allow one to dynamically move and braid Majorana fermions by tuning side gate voltage along the relocated edge states. We can even generalize corner junctions to a checkerboard structure to fabricate a network for quantum computing in a single quantum well. One can detect these relocated edge states by the scheme shown in Fig. 2.6(b). Without the relocated edge states, the corner junction of two s-wave superconductors form a conventional Josephson junction. Single electron tunneling is forbidden in the conventional Josephson junction. This gives the current-phase relation as a 2π periodic function. If relocated edge states appear along the Josephson junction, one can use a gate to create Majorana fermions on the Josephson junction, as shown in Fig. 2.6(b). The Majorana fermions provide a channel to tunnel single electron across the Josephson junction [68], which provides a 4π periodic current-phase relation. We note that K. C. Nowack et. al.[69] recently used SQUID to map the current distribution on a HgTe quantum well. This technique may provide a practical way to measure the location of the relocated edge states.

In conclusion, the relocated edge states appear at the junction between the superconductor doped 2D topological insulator and the undoped one. These relocated edge states allow one to build a braiding network of the Majorana fermions inside a single quantum well without physically etching away quantum wells to form corner junctions. The relocated edge states allow one to dynamically switch the Josephson junction between a conventional and nonconventional one via tuning the gates.

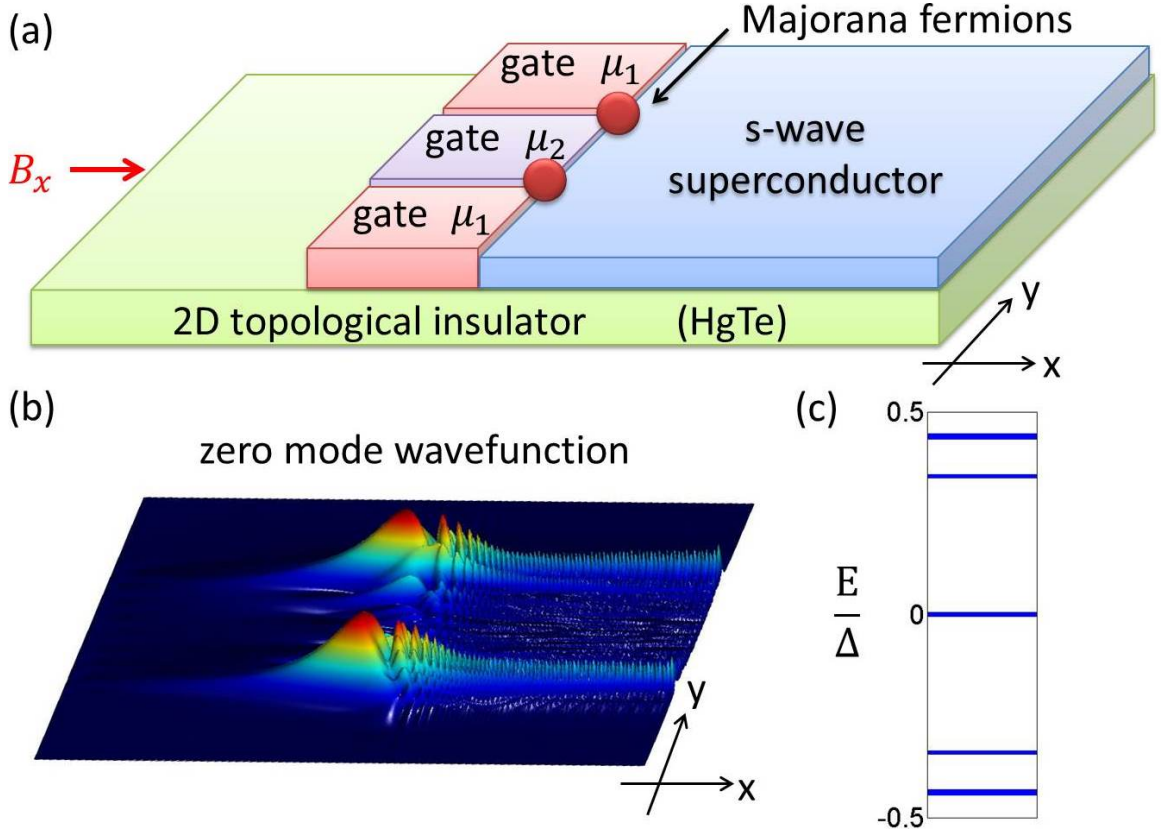


Figure 2.5: (a) The scheme of moving Majorana fermions along the relocated edge states. The red dots are the locations of the Majorana fermions. We use the gate at the non-superconducting side to switch the gap of relocated edge states between the Zeeman gap and superconducting gap. The Majorana fermions appear at the domain walls (red dots) where the gap switched. (b) The zero mode wavefunction of this device in 2D real space, The peaks indicate the location of Majorana fermions. (c) The energy spectrum of this device. We normalize the spectrum with the induced superconducting gap. The parameters in this simulation are superconducting gap $\Delta = 0.4$ (meV), in-plane magnetic field $B_x = 2$ (Tesla), doping level at superconducting side corresponds to chemical potential at $\mu_{SC} = 0.2$ (eV), two side gates $\mu_1 = \frac{DM}{B} = -7.4$ (meV), middle gate $\mu_2 = 7$ (meV). The parameters of HgTe are shown in Table I [58].

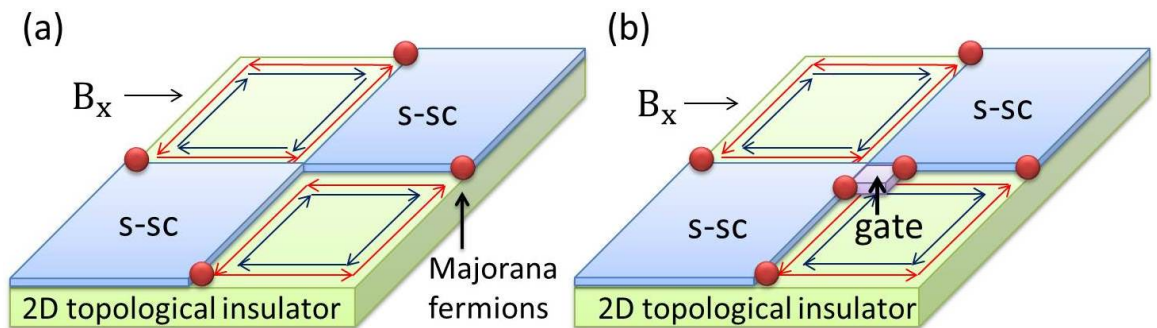


Figure 2.6: Use s-wave superconductors (s-sc) to relocate edge states to form a corner junction inside a single quantum well. In-plane magnetic field B_x is applied to break time reversal symmetry. (a) One can move Majorana fermions along the relocated edge states by applying the gates. (b) The relocated edge states allow one to change the corner junction from a conventional Josephson junction to an unconventional one by using a gate to create Majorana fermions on the Josephson junction.

Chapter 3

Revealing topological superconductivity in extended quantum spin Hall Josephson junctions

3.1 Motivation

As we mentioned in section 1.8, one way to reveal the topological superconductor is by observing the current phase relation in a Josephson junction. The Josephson junction built by topological superconductor has a tunneling current as a 4π periodic function of phase, which is called as fractional Josephson effect. However, experimentally observing fractional Josephson effect is very nontrivial. One of the reasons is because thermal fluctuation or quasi particle poisoning may switch the occupation number (parity) of the single fermionic states in a Josephson junction. Once parity is not conserved, the system may choose the parity which minimizes energy as shown in Fig.(1.8)(b). In this case, the energy phase relation of ground state becomes a 2π periodic function, which is the same as the one in a conventional Josephson junction. In this chapter, we show that although directly observing fractional Josephson effect may be difficult, topological superconductors imprint other qualitative signatures on the junction's interference pattern and the corresponding critical current even when parity switching processes are abundant.

Inspired by recent experiments by Hart *et al.* [43], we study transport in an ex-

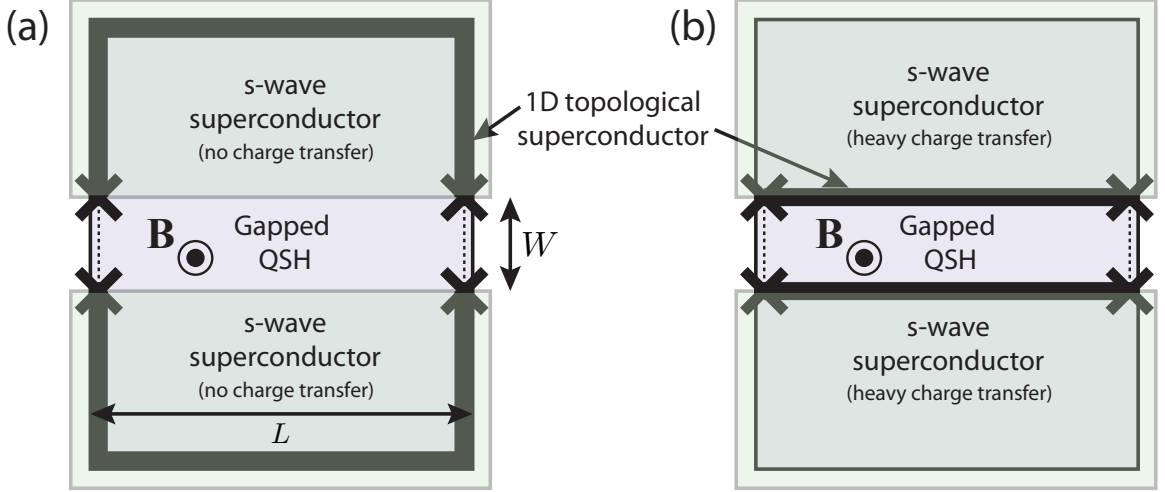


Figure 3.1: Extended QSH Josephson junctions that host 1D topological superconductivity. Topological superconductors reside either (a) at the outer boundary or (b) across the barrier depending on whether the superconductors doped the contacted QSH regions.

tended Josephson junction bridged by a quantum spin Hall insulator, as shown in fig. 3.1. We consider the case where the separation of superconductors is large enough so that most of the tunneling current is contributed from the edge channel. As we explain in section 1.5, the edge states with induced superconductivity are effectively 1D p-wave superconducting wires. To simplify calculations, the setup we show in Fig. (3.1) is modeled as a SQUID composed of topological superconductors. As we mentioned in the previous chapter, the locations of induced topological superconductivity appear at the circumference of quantum well, as shown in Fig. (3.1)(a) if the chemical potential of the topological insulator is inside the bulk gap. Due to work function mismatch between a superconductor and a topological insulator, we expect that superconductor dopes topological insulator in reality. If the doping level is large enough so that the chemical potential of a topological insulator goes into bulk band, we can switch the sign of mass term of topological insulator without changing bulk band. The doping of a topological insulator leads the edge states being relocated from the circumference of the quantum well to the domain wall between superconducting and insulating region, as shown in Fig. (3.1)(b). One can measure critical current $I_c(\Phi)$ as a function of magnetic flux Φ passing between the superconductors. This displays an

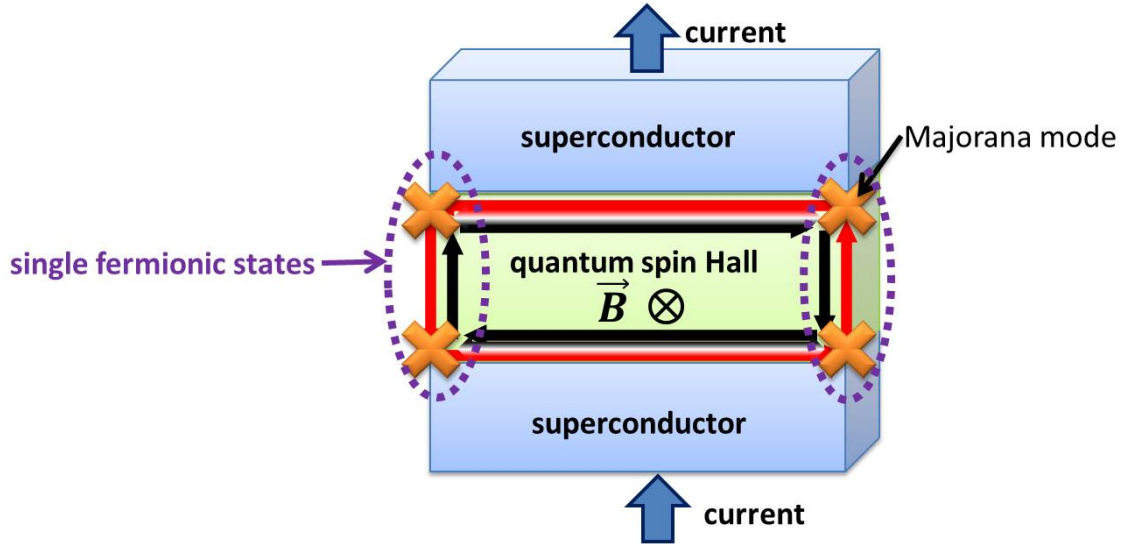


Figure 3.2: Majorana modes hybridize to each other through gapless edge modes to form single fermionic states. Each fermionic state supports channels for tunneling currents as $(-1)^{p_{L/R}} \sin(\delta\phi_{L/R}/2)$. Here $p_{L/R}$ and $\delta\phi$ is the occupation number and the phase difference of the states at left and right sides.

interference pattern that can reveal detailed information about the nature of current flow. Here we ask whether such interference measurements can provide fingerprints of 1D topological superconductivity. We show that if parity relaxes to minimize the energy, the critical current remains finite at any magnetic flux, contrary to conventional symmetric junctions. On the other hand, if parity instead flips randomly on all possible states, multiple critical currents are visible in the current-voltage traces, and the lower critical current vanishes at zero flux.

3.2 Extended Josephson junction model

For simplicity, we consider that the two superconductors are well separated from each other. Therefore, all the tunneling currents tunnel through the single fermionic states that are formed by hybridization of Majorana modes, as shown in Fig.(3.2).

One can simplify this junction as a SQUID which is composed of two individual Josephson junctions on the left/right sides of the edges. Each one supports a single Andreev bound state with energy $(-1)^{p_{L/R}} \Delta \cos(\delta\phi_{L/R}/2)$. Here Δ is the induced

pairing energy while $p_{L/R}$ and $\delta\phi_{L/R}$ respectively denote the parity and phase difference at the left/right sides. The phases across the junction at the left and right side of edges $\delta\phi_{L/R}$ follow from the phase difference ϕ between the two superconductors and the number of flux quanta $f = \Phi/(h/2e)$ threading the barrier. In other word, $\delta\phi_L = \phi$ and $\delta\phi_R = \phi + 2\pi f$. Defining a vector for the parity as $\mathbf{p} = (p_L, p_R)$, the bound states together contribute an energy

$$E_{\mathbf{p}}(\phi, f) = \Delta[(-1)^{p_L} \cos(\phi/2) + (-1)^{p_R} \cos(\phi/2 + \pi f)] \quad (3.1)$$

and a Josephson current

$$I_{\mathbf{p}}(\phi, f) = \frac{e}{\hbar} \partial_{\phi} E_{\mathbf{p}}(\phi, f) = \Delta[(-1)^{p_L} \sin(\phi/2) + (-1)^{p_R} \sin(\phi/2 + \pi f)] \quad (3.2)$$

This supercurrent is composed of two parallel channels, one from the left side of the edge as $\Delta[(-1)^{p_L} \sin(\phi/2)$, and another one from the right side of the edge as $\Delta[(-1)^{p_R} \sin(\phi/2)$. To calculate the current voltage relation, we model this Josephson junction as a RCSJ model [70]. In this model, the total current I is the sum of supercurrent $I_{\mathbf{p}}(\phi, f)$, and the normal current $I_N = V/R = \frac{\hbar}{2eR} \dot{\phi}$ comes from the resistance of Josephson junction and the noise $\zeta(t)$ comes from thermal fluctuation.

$$I = I_{\mathbf{p}}(\phi, f) + \frac{\hbar}{2eR} \dot{\phi} + \zeta(t) \quad (3.3)$$

The thermal noise current $\zeta(t)$ satisfies $\langle \zeta(t)\zeta(t') \rangle = 2T/R\delta(t-t')$ where T denotes the junction temperature. One can analog eq.(3.3) to equations of motion of a particle moving in potential U with overdamped friction force $\gamma\dot{x}$ and noise $\zeta(t)$

$$0 = -\partial_x U + \gamma\dot{x} + \zeta(t) \quad (3.4)$$

From this analogy, $I_{\mathbf{p}}(\phi, f) - I$ map to gradient of potential $\partial_x U$. In other words, we can think of equation (3.3) as a strongly damped particle with coordinate ϕ in a

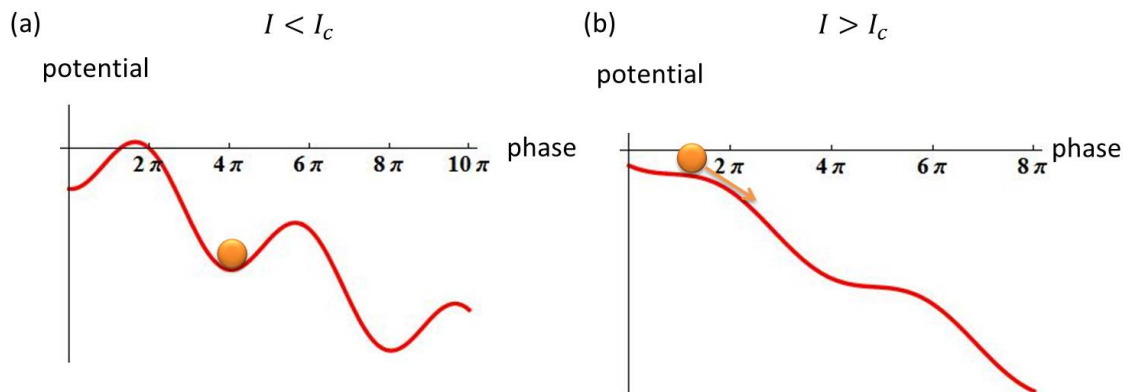


Figure 3.3: (a) When current I is smaller than critical current I_c , the washboard potential has local minimums to trap the system. Since phase is constant over time, we get zero voltage from Josephson relation. (b) When current is larger than critical current I_c , the washboard no longer has local minimums to trap the system. As the system tries to minimize its own energy, the phase grows over time, which leads to a nonzero voltage $V = \frac{\hbar}{2e} \frac{d\phi}{dt}$.

‘tilted washboard’ potential:

$$\begin{aligned}
 U_{\mathbf{p}}(\phi, f) &= E_{\mathbf{p}}(\phi, f) - \hbar I \phi / e \\
 &= \Delta [(-1)^{p_L} \cos(\phi/2) + (-1)^{p_R} \cos(\phi/2 + \pi f)] - \hbar I \phi / e \quad (3.5)
 \end{aligned}$$

One can extract the critical current from the formula of washboard potential. When current I is smaller than critical current I_c , the potential favors pinning the particle to one of its minima, as shown in Fig.(3.3)(a). In this case, the phase is a constant over time, which leads to zero voltage, as we know voltage V is proportional to the time derivative of phase $V = \frac{\hbar}{2e} \frac{d\phi}{dt}$. When current I is larger than critical current I_c , the potential no longer has a local minimum to trap our system, as shown in Fig.(3.3)(b). The particle will roll down along the potential as the systems try to minimize its energy. As a consequence, the phase of Josephson junction grows over time. This gives non-zero time derivative of phase, which leads to non-vanish voltage.

Both fermion states at left and right side of the junction can be either occupied or empty ($p_{L/R} = 0, 1$). This provides four different possible parities, and each parity

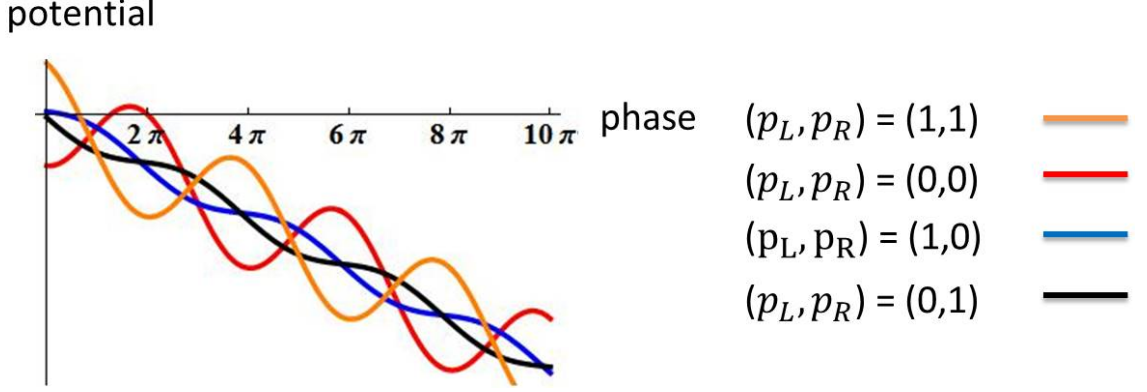


Figure 3.4: Four washboard potentials that correspond to four different parities.

gives its own corresponding washboard potential in eq.(3.5). Here we plot washboard potentials with four different parities in fig.(3.4).

Parity-switching events transfer the particle between different tilted washboard potentials ($U_{\mathbf{p}} \rightarrow U_{\mathbf{p}'}$) and thus provide an additional route for the phase ϕ to diffuse even at zero temperature. Our goal now is to quantify the effects of parity switching on transport in various interesting regimes.

3.3 Fokker-Planck analysis

To calculate the effect of parity switching, we define $\mathcal{P}_{\mathbf{p}}(\phi, t)$ as the distribution function that describes the probability of finding the system with parities \mathbf{p} and phase ϕ at time t . This function obeys a generalized Fokker-Planck equation:

$$\partial_t \mathcal{P}_{\mathbf{p}} = \frac{1}{\tau_R \Delta} \partial_{\phi} [\partial_{\phi} U_{\mathbf{p}} / 2 + T \partial_{\phi}] \mathcal{P}_{\mathbf{p}} + \sum_{\mathbf{p}'} [W_{\mathbf{p}' \rightarrow \mathbf{p}} \mathcal{P}_{\mathbf{p}'} - W_{\mathbf{p} \rightarrow \mathbf{p}'} \mathcal{P}_{\mathbf{p}}] \quad (3.6)$$

This equation is composed by two parts, the first part $\frac{1}{\tau_R \Delta} \partial_{\phi} [\partial_{\phi} U_{\mathbf{p}} / 2 + T \partial_{\phi}] \mathcal{P}_{\mathbf{p}}$ describes thermal phase diffusion along the tilted washboard potential $U_{\mathbf{p}}$ with a fixed parity [71, 72]. One can understand this part in a special case where we know the answer of probability distribution. Let's first consider the case where there is no parity switching $W_{\mathbf{p}' \rightarrow \mathbf{p}} = 0$ and no applied current $I = 0$. In this case, we know once the system is thermal equilibrium that the probability distribution of finding systems

at phase ϕ should satisfy Boltzmann distribution. In other words, probability distribution in this case is $\mathcal{P}_{\mathbf{p}} = e^{-U_{\mathbf{p}}/(2T)}$. We can put Boltzmann distribution into the first part of Fokker-Planck equation, we find $[(\partial_{\phi}U_{\mathbf{p}}/2) + T\partial_{\phi}] \mathcal{P}_{\mathbf{p}} = 0$. This leads to $\partial_t \mathcal{P}_{\mathbf{p}} = 0$ in the Fokker-Planck equation, as we expect, since Boltzmann distribution is the result of thermal equilibrium, and therefore it should be time independent.

The second part of Fokker-Planck equation $\sum_{\mathbf{p}'} [W_{\mathbf{p}' \rightarrow \mathbf{p}} \mathcal{P}_{\mathbf{p}'} - W_{\mathbf{p} \rightarrow \mathbf{p}'} \mathcal{P}_{\mathbf{p}}]$ incorporates parity switching with rates $W_{\mathbf{p} \rightarrow \mathbf{p}'}$. Equation (3.6) implicitly assumes that parity-flip processes do not involve an instantaneous change in the phase ϕ ; this holds provided the time scale for such events is the shortest in the problem. We model the corresponding transition rate from parity configuration \mathbf{p} to \mathbf{p}' by a Boltzmann like distribution:

$$W_{\mathbf{p} \rightarrow \mathbf{p}'}(\phi, f) = \frac{1}{\tau} e^{(E_i - E_j)/T_b} \quad (3.7)$$

With $1/\tau$ the typical parity-switching rate, T_b is a phenomenal parameter that we call bath temperature (which can differ from the junction temperature T), and E_i and E_j correspond to the energy of initial and final states. The transition rate $1/\tau$ is the rate in which electrons transfer between the particle sources and the junction. One can understand τ as the average waiting time for next parity switching event happens. The bath temperature T_b corresponds to the window of available energies carried by them. The small bath temperature limits $T_b \sim T \ll \Delta$, for instance, describe the case where the system always chooses the parity which minimizes the energy [19]. In contrast, the large bath temperature limit corresponds to the case where the system tries to equally populate through all possible parities. This scenario happens when the bound states merge with the continuum spectrums, which enhances quasiparticle poisoning.

Once we calculate the probability distribution $\mathcal{P}_{\mathbf{p}}$ of the each parity from the Fokker-Planck equation, we can use it to calculate the junction voltage. The DC voltage V is determined by stationary solutions of Eq. (3.6). More precisely, the

Josephson relation along with Eq. (3.3) yields

$$V = \frac{\hbar}{2e} \langle \dot{\phi} \rangle = \frac{\hbar}{2e} \sum_{\mathbf{p}} \int_0^{4\pi} d\phi \dot{\phi} \mathcal{P}_{\mathbf{p}}(\phi) = R \sum_{\mathbf{p}} \int_0^{4\pi} d\phi [I - I_{\mathbf{p}}(\phi, f)] \mathcal{P}_{\mathbf{p}}(\phi) \quad (3.8)$$

Determining the $I - V$ characteristics thus reduces to solving Eq.3.6 for the steady-state distribution function $\mathcal{P}_{\mathbf{p}}(\phi)$, which is readily achieved numerically by discretizing ϕ . Below we briefly discuss the solution with conserved parity ($1/\tau = 0$) and then address the more realistic case where parity switching occurs.

3.4 Parity conserved case

When the parities \mathbf{p} are conserved ($1/\tau = 0$), the Andreev bound states on the left and right sides of the edges contribute the Josephson current as $\pm\Delta[\sin(\phi_{L/R}/2)]$, where \pm is determined by the occupation number of the Andreev bound states and $\phi_{L/R}$ corresponds to the phase difference across the junction. The total supercurrent at zero temperature I_{total} is the sum of the supercurrent from the left and right sides. Depend on the occupation number of the Andreev bound states on left and right side, it gives two possible outcomes of the total supercurrent as $I_{\text{total}} = \Delta[\sin(\phi_L/2) + \sin(\phi_R/2)]$ or $I_{\text{total}} = \Delta[\sin(\phi_L/2) - \sin(\phi_R/2)]$. Once we maximize current I_{total} by using the relation of phase $\phi_L - \phi_R = 2\pi f$ to get critical current, we get the critical current as shown in Fig.(3.5).

One can get the current voltage relation by solving the generalized Fokker-Planck equation. For parity fixed case, it admits four steady-state solutions—one for each parity sector. The solutions coincide with the known Ambegaokar-Halperin expressions [71] evaluated with an unconventional current-phase relation $I_{\mathbf{p}}(\phi, f)$. At $T = 0$ the voltage follows as [71, 70]:

$$V = \Theta(I - I_{\mathbf{p},c}) R \sqrt{I^2 - I_{\mathbf{p},c}^2}, \quad (3.9)$$

where $\Theta(x)$ is the Heaviside step function, and the critical currents are $I_{\mathbf{p},c} = e\Delta |\cos(\pi f/2)|/\hbar$

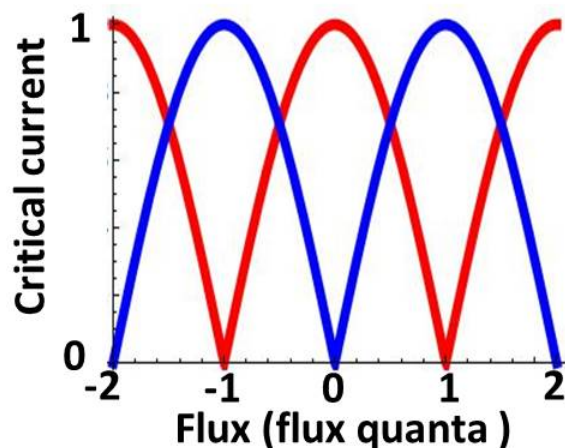


Figure 3.5: Critical current as function of flux. Red curve and Blue curve corresponds to the critical current of even (both Andreev bound states are occupied $|1, 1\rangle$) and odd $|1, 0\rangle$ (one occupied and other empty) parity, respectively.

for parity even case $p_R = p_L$ and $I_{p,c} = e\Delta|\sin(\pi f/2)|/\hbar$ for parity odd case $p_R \neq p_L$. For a given flux f , we plot current-voltage relation of eq.(3.9) as a black solid curve in fig.(3.6). At finite temperature $T \neq 0$, due to thermal fluctuation, the voltage develops even though current is smaller than critical current. We plot current-voltage relation in finite temperature as a red dashed curve in fig.(3.6).

To get the relation between critical current and flux, we plot the color map of voltage V as a function of applied current and flux in fig.3.7. Figures 3.7(c) and (d) respectively illustrate the low-temperature interference patterns in the even- and odd-parity sectors. One can compare these interference patterns in Fig.(3.7) with the usual Fraunhofer pattern that people have observed in conventional Josephson junction in Fig.(3.8). As one can see from these figures, the critical current in a conventional Josephson junction oscillate every one flux quanta, while the Josephson junction built by topological superconductors exhibits an anomalous two-flux-quanta periodicity in critical current on both even and odd parity sectors. This is a striking yet fragile fingerprint of topological superconductivity. As we mentioned in section 1.8, two flux quantum oscillation in Fraunhofer pattern can be spoiled by any finite switching rate $1/\tau \neq 0$, which in our setup will always arise due to mixing with continuum quasiparticles and other noise sources. Fortunately, other signatures of

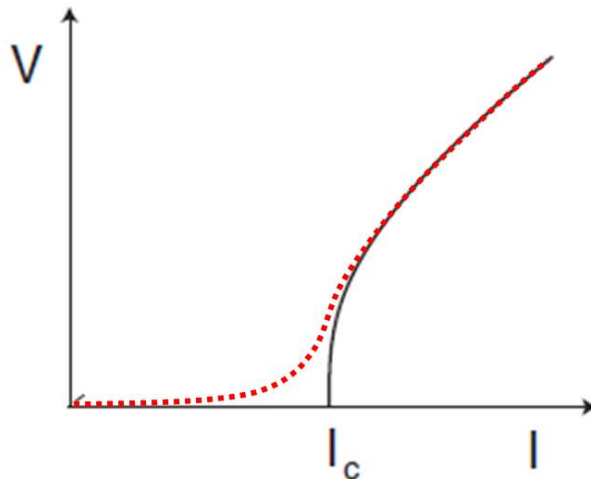


Figure 3.6: Current voltage relation of a resistively shunted Josephson junction. Black curve is at zero temperature. Red dashed curve corresponds to finite temperature.

topological superconductivity nevertheless persist even when parity is fluctuating.

3.5 Low bath temperature parity switching case

When parity is fluctuating ($1/\tau \neq 0$), parity flip processes happens. Let's first consider the low bath temperature limit ($T_b \ll \Delta$), where the transition rates in Eq. (3.7) depend strongly on the relative energies in different parity sectors. As one can see in Eq. (3.7), the transition rate from a lower energy level to higher energy one is exponentially suppressed at low bath temperature T_b . At the limit where temperatures $T \rightarrow 0$ and bath temperature $T_b \rightarrow 0$, the systems chooses the parity which minimizes the energy. In other words, we can minimize washboard potential $U(\phi, f)$ by choosing parity \mathbf{p} so that $U(\phi, f) = \min_{\mathbf{p}} U_{\mathbf{p}}(\phi, f)$. As shown with a black solid curve in fig.(3.9), we effectively have one washboard potential $U(\phi, f)$ in low bath temperature limit. The effective washboard potential $U(\phi, f)$ has local minimums to hold the system if the applied current is smaller than the critical current, as shown in Fig.(3.9)(a). As the applied current exceeding the critical current, the local minimum disappears as shown in fig.(3.9)(b).

One can solve the critical current in low bath temperature limit by finding the

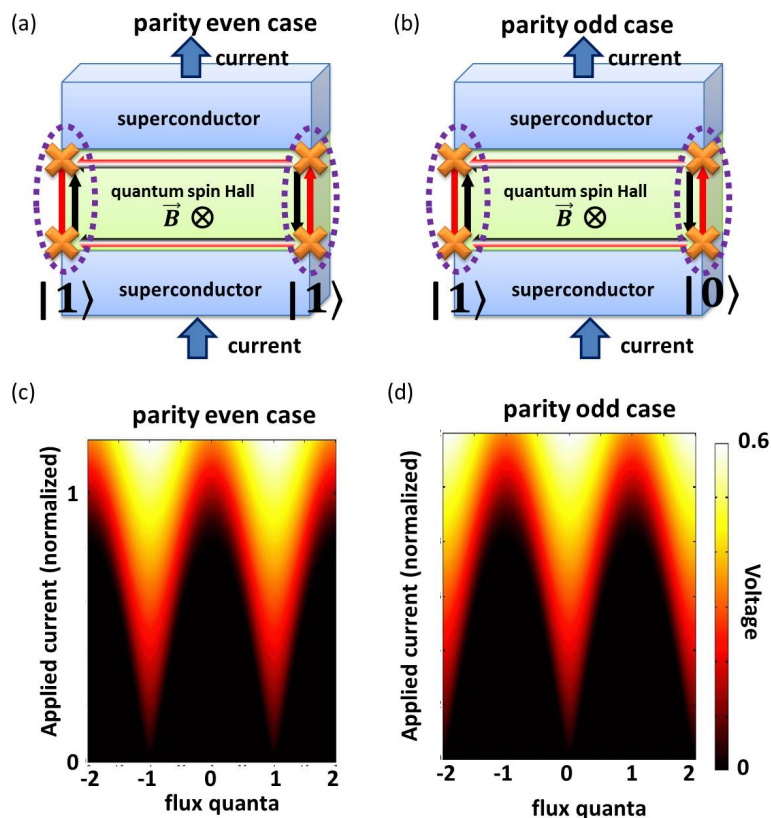


Figure 3.7: (a) and (b) give the example of the occupation numbers of the fermionic state in Josephson junction for parity even and odd case, respectively. In the parity-conserving limit ($1/\tau = 0$), we plot interference patterns in (c) and (d), where (c) corresponds to parity even and (d) corresponds to the parity odd case. The color scale indicates voltage in units of $2eR\Delta/\hbar$ while current is normalized by $e\Delta/\hbar$. Temperature for (c)(d) is $T = 0.05\Delta$.

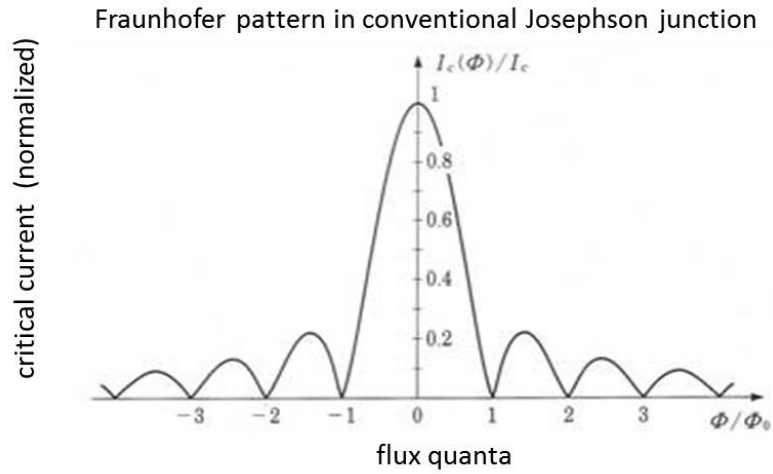


Figure 3.8: Fraunhofer pattern of a conventional Josephson junction. Here we plot critical current as a function of flux Φ . The critical current oscillates every one flux quanta.

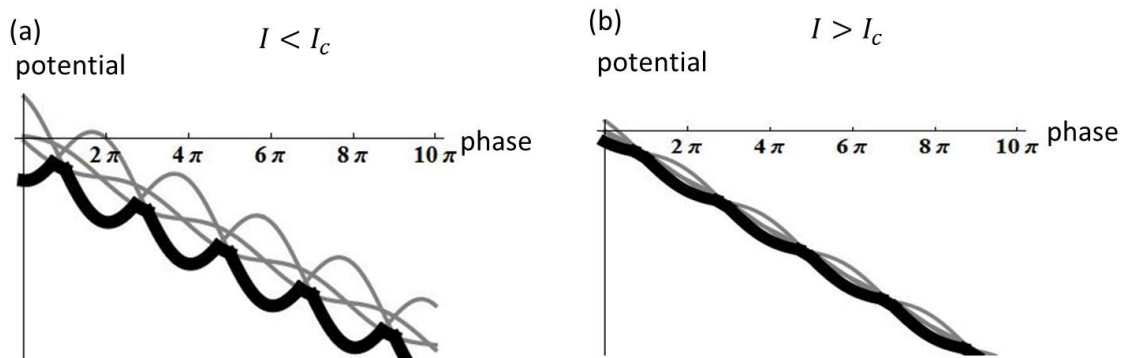


Figure 3.9: Washboard potentials for low bath temperature limit ($T_b \ll \Delta$). Four different parities correspond to four different washboard potential. The solid black line represents the minimum washboard potential of a given phase, gray curves are the others. Fig.(a) corresponds to applied current smaller than critical current, while Fig.(b) is the case otherwise.

maximal current I for which $\partial_\phi U_{\mathbf{p}}(\phi, f) = 0$ admits a solution. In this way, we find critical current as $I_c = e\Delta/\hbar \max\{\cos^2(\pi f/2), \sin^2(\pi f/2)\}$. Figure 3.10(a) displays the numerically computed interference pattern at small but finite T and T_b (which includes thermal phase slips that smear the critical current, as in conventional junctions). The critical current clearly remains finite for all fluxes and roughly follows the larger of the critical currents present in the parity-conserving cases shown in Figs. 3.7(c) and (d). Here the absence of nodes is a remnant of the unconventional current-phase relation rooted in topological superconductivity.

One can compare this result with the experimental data in Ref. [43]. The data indeed show the nodes-lifting feature of the critical current plot. Other sources such as current asymmetry could also lead to nodes-lifting feature appearing in the critical current plot. Investigating how the nodes evolve as a function of an in-plane magnetic field is one way of distinguishing our node-lifting mechanism from other more conventional sources. The idea is to use in-plane magnetic field to drive the superconductor from topological regime to trivial regime. If the nodes-lifting in the critical current is due to parity switching evens in the topological phase, the nodes should recover once the in-plane magnetic field drives the superconductor into the trivial regime. The critical current in experimental data decays as magnetic field increases, while in our simulation, the critical current maintain in the same magnitude even several fluxes are inserted into the junction. The decay of the critical current in Fig.3.10(b) comes from the fact that edge states are not a perfect 1D channel. The adage states actually exponentially decay from the edge into bulk. To simulate the real experiment, we calculate the Fraunhofer pattern by using wave function distributions of edge states from the four band models [40] in the next section.

3.5.1 Critical current with minimum energy

We first prove that the tunneling current of the device in fig. 3.11 is $I = \partial E/\partial\varphi_0$, where E is the Andreev bound state energy, and φ_0 is the offset phase of superconductor that is defined in eq.(3.23).

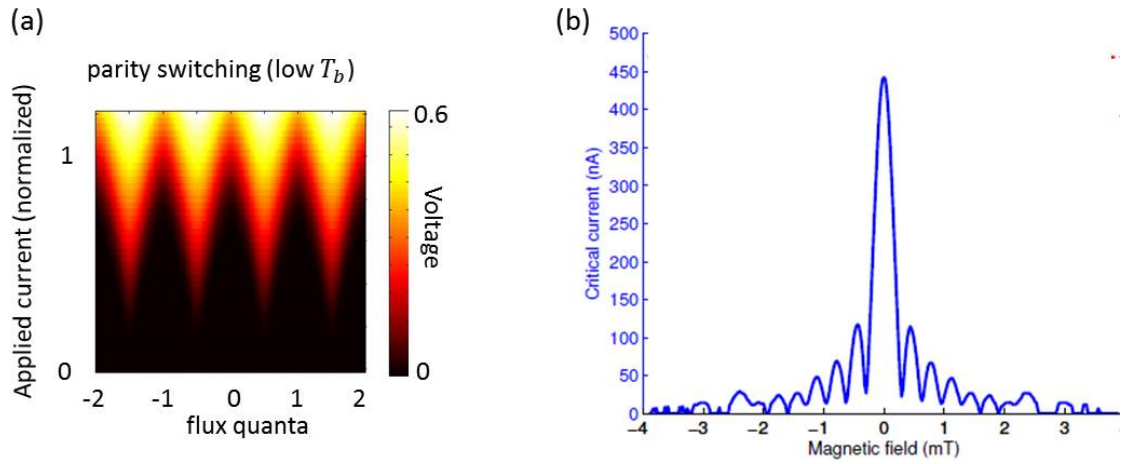


Figure 3.10: (a) Interference patterns in with parity switching at low ($T_b = 0.02\Delta$) bath temperature. The color scale indicates voltage in units of $2eR\Delta/\hbar$ while current is normalized by $e\Delta/\hbar$. Temperature $T = 0.02\Delta$, $\tau = 50\tau_R$. (b) Critical current extract from experimental data in Ref.[43]. One can notice the nodes lifting feature in this critical current plot. Source of fig (b) is from Ref.[43].

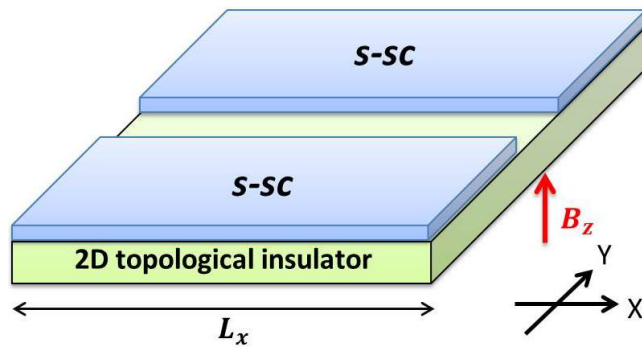


Figure 3.11: A Josephson junction on top on 2D topological insulator such as HgTe quantum well. Magnetic field B_z penetrates the junction.

We begin from the continuous equation of current density \vec{J} , source S , and density ρ , which can be described as:

$$\frac{\partial \rho}{\partial t} = -\nabla \cdot \vec{J} + S \quad (3.10)$$

$$= -\frac{i}{\hbar}[\rho, H_{HgTe}] - \frac{i}{\hbar}[\rho, H_{sc}] \quad (3.11)$$

Here we use the 4 band model as the Hamiltonian of HgTe quantum well H_{HgTe} , and we model the pairing potential as follows:

$$H_{sc} = \Delta c_{\uparrow}^{\dagger} c_{\downarrow}^{\dagger} + \Delta^{\dagger} c_{\downarrow} c_{\uparrow} \quad (3.12)$$

The source term comes from the formation of cooper pair, and therefore we can identify the source term (or sink term) as:

$$S = -\frac{i}{\hbar}[\rho, H_{sc}] \quad (3.13)$$

Consider the stationary states where the density ρ does not change over time; therefore, $\partial \rho / \partial t = 0$. Put this condition into the continuous equation eq.(3.11), and we get the divergence of the current as:

$$\nabla \cdot \vec{J} = S = -\frac{i}{\hbar}[\rho, H_{sc}] \quad (3.14)$$

The charge density operator can be written as

$$\rho = e(c_{\uparrow}^{\dagger} c_{\uparrow} + c_{\downarrow}^{\dagger} c_{\downarrow}) \quad (3.15)$$

Putting this density operator eq.(3.15) into the Heisenberg equation of motion eq.(3.16), we get the divergence of the current as follows:

$$\nabla \cdot \vec{J} = -\frac{i}{\hbar}[\rho, H_{sc}] = -2\frac{ie}{\hbar}(\Delta c_{\uparrow}^{\dagger} c_{\downarrow}^{\dagger} - \Delta^{\dagger} c_{\downarrow} c_{\uparrow}) \quad (3.16)$$

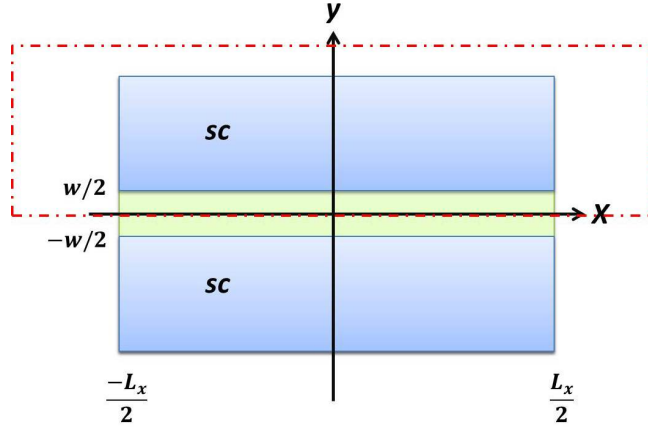


Figure 3.12: A Josephson junction with width L_x and separation w . Magnetic field B_z penetrates the junction.

We can simplify the last line of eq.(3.16) furthermore by rewriting the pairing potential Δ as its phase θ and amplitude Δ_0 as:

$$\Delta = \Delta_0 e^{i\theta} \quad (3.17)$$

The divergence of the current can therefore be simplified as:

$$\nabla \cdot \vec{J} = -2 \frac{ie}{\hbar} (\Delta c_{\uparrow}^{\dagger} c_{\downarrow}^{\dagger} - \Delta^{\dagger} c_{\downarrow} c_{\uparrow}) = -2 \frac{e}{\hbar} \frac{\partial H_{sc}}{\partial \theta} \quad (3.18)$$

We can apply Gauss theorem on eq.(3.18) to get the current I . We first set the coordinate of our device in fig.(3.12). Then we integrate the $\nabla \cdot \vec{J}$ over the red box shown in fig.(3.12). We get the current I as:

$$\hat{I} = \int_{-L_x/2}^{L_x/2} dx J(x, y = 0) \quad (3.19)$$

$$= \int_{\text{red box}} d^2r \nabla \cdot \vec{J} = -2 \frac{e}{\hbar} \int_{\text{red box}} d^2r \frac{\partial H_{sc}}{\partial \theta} \quad (3.20)$$

To simplify eq.(3.20) furthermore, we need to see how the superconductor phase θ winds when magnetic field B_z is applied in the Josephson junction. We assume the magnetic field \vec{B} only penetrates through the junction (in $-\frac{w}{2} < y < \frac{w}{2}$ region) and vanishes at superconductor region (in both $\frac{w}{2} < y$ and $y < -\frac{w}{2}$ region). Therefore,

we can write the magnetic field as:

$$\vec{B} = \begin{cases} 0 & y > \frac{w}{2} \\ B_0 \hat{z} & -\frac{w}{2} < y < \frac{w}{2} \\ 0 & y < -\frac{w}{2} \end{cases} \quad (3.21)$$

The vector potential \vec{A} can then be calculated by using $\vec{B} = \nabla \times \vec{A}$. This gives:

$$\vec{A} = \begin{cases} -B_0 \frac{w}{2} \hat{x} & y > \frac{w}{2} \\ -B_0 y \hat{x} & -\frac{w}{2} < y < \frac{w}{2} \\ B_0 \frac{w}{2} \hat{x} & y < -\frac{w}{2} \end{cases} \quad (3.22)$$

With this vector potential \vec{A} in hand, we can calculate the superconducting phase θ by using $\nabla\theta = 2\pi \frac{\vec{A}}{\phi_0}$, where $\phi_0 = \frac{h}{2e}$ is the flux quanta. In this way, we get the superconducting phase θ as:

$$\theta = \begin{cases} \varphi_0 - \frac{\pi B_0 w}{\phi_0} (x + \frac{L_x}{2}) & y > \frac{w}{2} \\ \text{ill defined} & -\frac{w}{2} < y < \frac{w}{2} \\ \frac{\pi B_0 w}{\phi_0} (x + \frac{L_x}{2}) & y < -\frac{w}{2} \end{cases} \quad (3.23)$$

The superconducting phase θ is ill-defined when pairing potential Δ vanishes. The offset phase φ_0 corresponds to the superconducting phase difference at left edge of the Josephson junction ($x = -\frac{L_x}{2}$).

To get the total current from eq.(3.20), we can use the fact that for a fixed magnetic field B , we have $d\theta = d\varphi_0$ inside the red box of fig.(3.12). In other words, by using eq.(3.23), we can see that:

$$\frac{\partial H_{sc}}{\partial \theta} = \frac{\partial H_{sc}}{\partial \varphi_0} = \frac{\partial H_{\text{total}}}{\partial \varphi_0} \quad \text{if } y > \frac{w}{2} \quad (3.24)$$

We take a derivative of total Hamiltonian $H_{\text{total}} = H_{\text{HgTe}} + H_{sc}$ in the last equality

of eq.(3.24) because the The Hamiltonian of HgTe (H_{HgTe}) is independent of offset phase φ_0 .

Putting eq.(3.24) into eq.(3.20), we get the current operator \hat{I} :

$$\hat{I} = -2\frac{e}{\hbar} \int_{\text{red box}} d^2r \frac{\partial H_{\text{total}}}{\partial \varphi_0} \quad (3.25)$$

We can get the expected value of the current by sandwich the current operator between the eigenfunction $\psi_E(x, y)$; here eigenfunction $\psi_E(x, y)$ satisfied eigen equation $H_{\text{total}}\psi_E(x, y) = E\psi_E(x, y)$. This gives the expectation value of the current as :

$$\langle \hat{I} \rangle_E = -2\frac{e}{\hbar} \int_{\text{red box}} d^2r \psi_E^\dagger(x, y) \left\{ \frac{\partial H_{\text{total}}}{\partial \varphi_0} \right\} \psi_E(x, y) \quad (3.26)$$

$$\begin{aligned} &= -2\frac{e}{\hbar} \int_{\text{red box}} d^2r \frac{\partial}{\partial \varphi_0} \left\{ \psi_E^\dagger(x, y) H_{\text{total}} \psi_E(x, y) \right\} \\ &\quad + 2\frac{e}{\hbar} \int_{\text{red box}} d^2r \left\{ \frac{\partial}{\partial \varphi_0} \psi_E^\dagger(x, y) \right\} H_{\text{total}} \psi_E(x, y) \\ &\quad + 2\frac{e}{\hbar} \int_{\text{red box}} d^2r \psi_E^\dagger(x, y) H_{\text{total}} \left\{ \frac{\partial}{\partial \varphi_0} \psi_E(x, y) \right\} \\ &= -2\frac{e}{\hbar} \frac{\partial E}{\partial \varphi_0} \int_{\text{red box}} d^2r \psi_E^\dagger(x, y) \psi_E(x, y) \\ &= -\frac{e}{\hbar} \frac{\partial E}{\partial \varphi_0} \end{aligned} \quad (3.27)$$

Eq.(4.48) is the current contribution from energy E channel. To get the total current, we can write the Hamiltonian in the energy eigen basis as:

$$\begin{aligned} H_{\text{total}} &= \sum_{E>0} E \Gamma_E^\dagger \Gamma_E + \sum_{E<0} E \Gamma_E^\dagger \Gamma_E \\ &= \sum_{E>0} E \Gamma_E^\dagger \Gamma_E - E \Gamma_{-E}^\dagger \Gamma_{-E} \\ &= \sum_{E>0} E \left\{ \Gamma_E^\dagger \Gamma_E - \Gamma_E \Gamma_E^\dagger \right\} \\ &= 2 \sum_{E>0} E \left\{ \Gamma_E^\dagger \Gamma_E - \frac{1}{2} \right\} \end{aligned} \quad (3.28)$$

Putting eq.(3.28) into eq.(3.25) and eq.(4.48) gives the total current that comes from

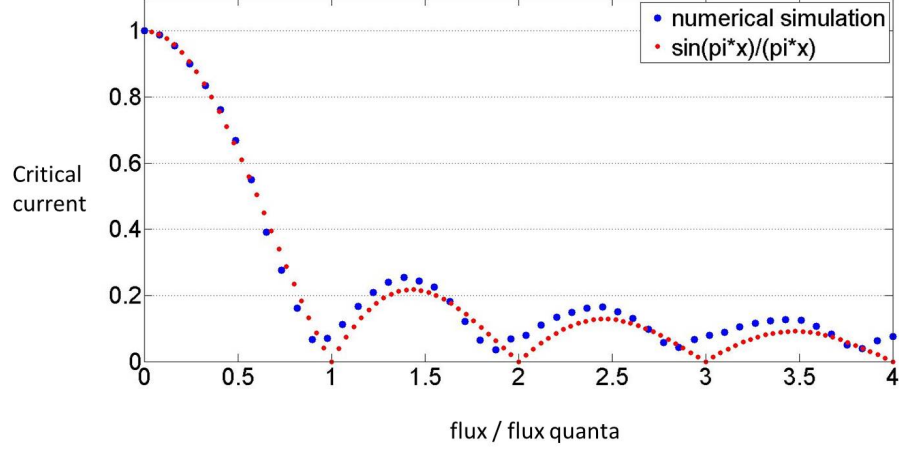


Figure 3.13: The critical current at zero temperature as a function of flux. The blue dots are the critical current of long Josephson junction built by topological superconductor, such as the device shown in fig.(3.11). The red dots correspond to the critical current of a long Josephson junction built by trivial superconductor. Here we assume that the systems occupies the states according to the Fermi Dirac distribution.

all energy channels as:

$$\langle \hat{I} \rangle_{\text{total}} = -\frac{2e}{\hbar} \sum_{E>0} \frac{\partial E}{\partial \varphi_0} \left\{ \langle \Gamma_E^\dagger \Gamma_E \rangle - \frac{1}{2} \right\} \quad (3.29)$$

Here $\langle \Gamma_E^\dagger \Gamma_E \rangle$ is the Fermi-Dirac distribution. The Fermi-Dirac distribution is coming from the assumption that the system occupies different parity sectors with probability distribution that satisfied Fermi-Dirac distribution. In reality, one should solve this probability distribution by using Fokker-Planck analysis in eq.(3.6).

For simplicity, let's consider the zero temperature limit where Fermi-Dirac distribution $\langle \Gamma_E^\dagger \Gamma_E \rangle = 0$ for $E > 0$. In this case tunneling current in eq.(3.29) simplifies into

$$\langle \hat{I} \rangle_{\text{total}} = \frac{e}{\hbar} \sum_{E>0} \frac{\partial E(\varphi_0, \Phi_B)}{\partial \varphi_0} \quad \text{for zero temperature} \quad (3.30)$$

Here Φ_B is the total flux through the junction. The critical current I_{critical} can be cal-

culated by choosing the offset phase φ_0 such that it maximizes the current in eq.(3.30). By using eq.(3.30), the problem of calculating tunneling current is simplified into an eigenvalue problem. To simulate a real experimental system, we calculate the eigen energy by diagonalize the four band model [40] of HgTe quantum well with induced pairing potential and flux in real space. This gives us the eigen energy $E(\varphi_0, \Phi_B)$ as a function of flux Φ_B and superconducting phase φ_0 . We can then use eq.(3.30) to calculate current. The numerical simulation is shown in fig.(3.13). One can see the Fraunhofer pattern with node lifting features.

3.6 High bath temperature parity switching case

Finally, we analyze the high bath temperature limit $T_b \gg \Delta$ where the parities fluctuate randomly, independently of the initial and final energies, on a time scale τ . As one can see in eq.(3.7), when bath temperature T_b goes to infinity, the probability will equally distribute through all possible parities. Because parity even and odd correspond to different critical currents as shown in fig.3.5, if the system could indeed populate through all possible parity sectors, which critical current are we going to measure?

To answer this question, let's first notice that there are three distinct current regimes separated by the critical currents $I_{c1} = \min_{\mathbf{p}} I_{\mathbf{p},c}$ and $I_{c2} = \max_{\mathbf{p}} I_{\mathbf{p},c}$. For $I < I_{c1}$ local minima exists in the washboard potentials $U_{\mathbf{p}}$ for all four parity sectors. Nevertheless, even at $T = 0$ —where thermal diffusion is absent—the phase ϕ can still transform between minima of $U_{\mathbf{p}}$ via parity-switching events; see Figs.(3.14). After two consecutive parity flips, ϕ either returns to its initial value, as shown in Figs. 3.14(c), or shifts by $\pm 2\pi$, as Figs. (3.14)(a) and (b) illustrate. The 2π and -2π phase changes occur with essentially equal probability when $T_b \gg \Delta$, and moreover contribute equal but opposite voltages. Hence, these processes cancel one another out in the dc limit. In other words, parity switching events generate telegraph noise in the voltage with equal probability of positive and negative signals that time-average to zero.

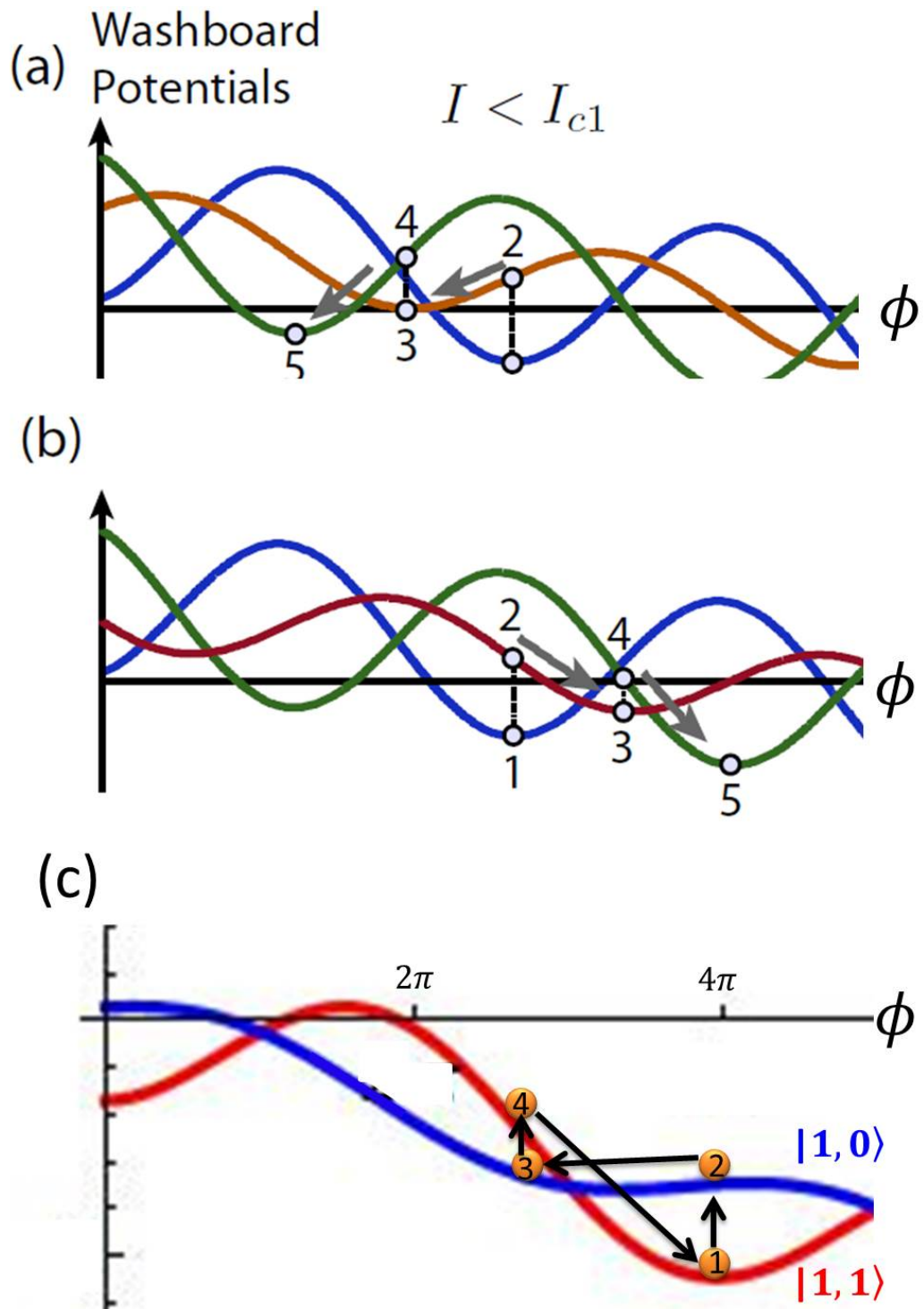


Figure 3.14: Washboard potentials for select parity sectors in the high-bath-temperature regimes. For low currents $I < I_{c1}$, consecutive parity flips can mediate $\pm 2\pi$ phase slips as in (a) and (b), or the phase slips cancel each other out in consecutive parity flips as shown in (c).

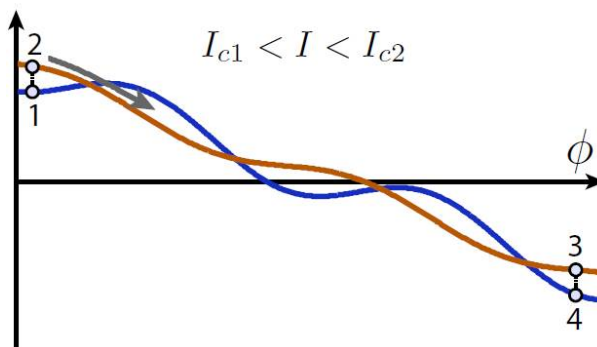


Figure 3.15: (color online). Washboard potentials for select parity sectors in the high-bath-temperature regimes. When currents I is at the regime of $I_{c1} < I < I_{c2}$, One parity have washboard potential with local minimums to trap the system (blue curve), while other parity does not have a local minimum (red curve). The parity switching process leads a net phase drifting, from which arises nonzero voltage.

With currents between I_{c1} and I_{c2} only two of the washboard potentials exhibit stable minima. Because of the high bath temperature, the phase ϕ can escape from one of these minima via a parity-switching event into a potential without any minima, producing a steady drift of ϕ . The drift ceases only when a subsequent parity flip re-traps the phase; see Fig. 3.15 for an illustration.

When applied current is larger than critical currents of all parities, none of the band support minima, and the phase ϕ drifts continuously as in Fig.3.16.

We thus arrive at the following overall picture for the high-bath-temperature case. When current is smaller than all critical currents of all possible parity sectors $I < I_{c1} = \min_{\mathbf{p}} I_{\mathbf{p},c}$ voltage remains negligible. In other words, in high bath temperature, lower critical current I_{c1} as a function of flux follows the *minimum* of the critical currents associated with the four parity sectors. Furthermore, the critical current vanishes at zero flux and is maximal at one-half flux quantum—precisely as in a π -junction [see Fig.3.17]. For $I > I_{c1}$ the voltage is far from featureless—a second critical current $I_{c2} = \max_{\mathbf{p}} I_{\mathbf{p},c}$ also appears, reflecting the multiple parity sectors. This feature becomes prominent upon examining d^2V/dI^2 [Fig. 3.18(a)] as well as specific voltage-current line cuts [Fig. 3.18(b)]. Thus, long parity-flip times τ allow one to image the critical currents in all parity sectors. Rapid parity flipping, however, renders the junction resistive at any flux and yields identically zero critical current.

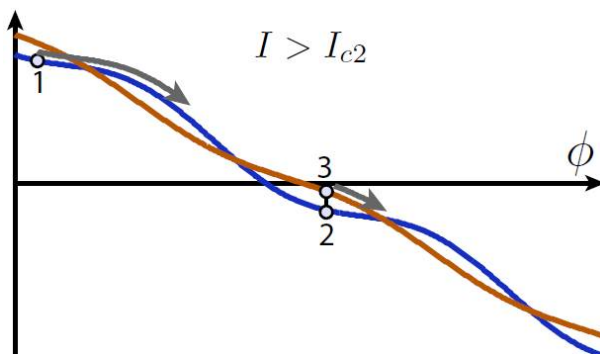


Figure 3.16: (color online). Washboard potentials for select parity sectors in the high-bath-temperature regimes. When currents I is larger than critical current in all parity sections $I_{c1} < I_{c2} < I$, none of the parity has washboard potential with local minimums to trap the system. The phase will keep increasing over time as the system tries to minimize the energy, from which arises nonzero voltage.

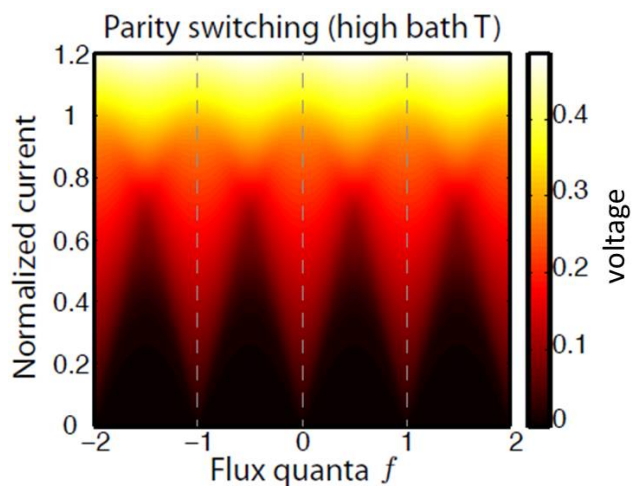


Figure 3.17: (color online). Interference patterns with parity switching at high ($T_b = 100\Delta$) bath temperature. The color scale indicates voltage in units of $2eR\Delta/\hbar$ while current is normalized by $e\Delta/\hbar$. Data correspond $T = 0.02\Delta$, $\tau = 5\tau_R$.

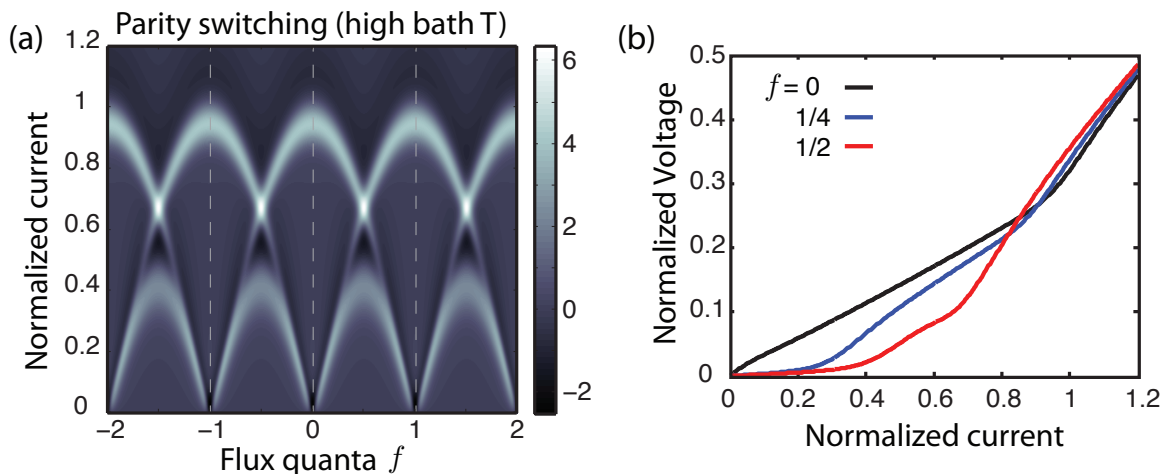


Figure 3.18: (color online). (a) Color plot of d^2V/dI^2 and (b) voltage-current line cuts corresponding to the high-bath-temperature data in Fig.(3.17). The two critical currents I_{c1} and I_{c2} are clearly visible in both plots. Voltage and current are respectively expressed in units of $2eR\Delta/\hbar$ and $e\Delta/\hbar$.

3.7 Discussion

Our study of extended QSH Josephson junctions reveals that parity switching processes, although destructive to the critical current's anomalous periodicity, generate new fingerprints of the underlying topological superconductors expected to form. Surprisingly, stronger poisoning actually *enhances* the signatures in the critical current. We expect the results to apply quite generally—even when the actual switching mechanism differs from our model. For instance, if the bound-state energies approach the continuum states near Δ then bulk quasiparticles can easily mediate parity flips [30]. We verified numerically that qualitatively similar behavior to the high- T_b limit arises when switching occurs predominantly at energies near Δ .

While our analysis has so far included only 4π -periodic current contributions, it is important to note that conventional 2π -periodic components $\propto \sin \delta\phi_{R/L}$ generically flow in parallel. With low bath temperatures their effects are decidedly minor—the lifted nodes in Fig. 3.10 survive even for quite large conventional currents. More significant effects occur at high bath temperature. There the new terms lead to deviations from the π -junction behavior mimicked in Fig. 3.17. The resulting interference pattern nevertheless *still* remains anomalous. Most importantly, multiple critical cur-

rents remain visible in the current-voltage relation. The critical current, as with low bath temperatures, also remains finite for any magnetic field.

The absence of nodes in the critical current at half-integer flux quanta thus survives quite generally from the interplay between fractional Josephson physics and parity switching. To provide a compelling indicator of topological superconductivity, however, the ability to experimentally distinguish from other node-lifting mechanisms such as current asymmetry is essential. This may be achieved by introducing a strong *in-plane* magnetic field, which can force the 1D topological superconductors at the junction into a trivial phase [19]. Therefore, observing the controlled destruction and revival of nodes as one varied the in-plane field strength would likely rule out alternative mechanisms and provide strong evidence for topological superconductivity.

Chapter 4

Universal transport signatures of topological superconductivity in quantum spin Hall architectures

4.1 Introduction

Topological superconductors are particularly interesting in light of the active ongoing experimental efforts for realizing exotic physics such as Majorana zero modes[1, 37, 73, 74, 75, 38]. These zeros modes could pave the way towards topological quantum information processing[76]. Ongoing experiments have provided undeniable results which indicate the existence of Majorana zero modes, but complementary experiments need to be performed which take us beyond any doubt. One major issue is that many proposals[77, 78, 79, 80] for finding Majorana zero modes come from heterostructures which require topological superconductivity. Thus, identification of Majorana zero modes requires signatures of topological superconductivity.

One possible procedure for this identification would be first find signatures of a topological superconductor and then use the topological superconductor to host Majorana zero modes. One way to do this is to break time reversal symmetry on a domain of the topological superconductor. A natural system to implement such a procedure is a 2D topological insulator, since proximity pairing to a superconductor will induce pairing on the 2D topological insulator[4, 81]; thereby creating a topological superconducting region. One can then break time reversal symmetry with

a magnetic field after confirming the existence of the topological superconductor to bind Majorana zero modes.

Inspired by recent experimental progress on inducing superconductivity in edge states of 2D topological insulators[2, 9, 82], we want to ask how we unambiguously reveal topological superconductivity if it indeed appears in such a set up. Due to the fact that some of these experiments[2, 9] are done by building long Josephson junctions on top of 2D topological insulators, the fractional Josephson Effect[77, 4] seems the most natural way to probe topological superconductivity in these experiments. However, this effect requires parity conservation in Josephson junction[83, 84], which can easily be destroyed by quasi-particle poisoning or thermal fluctuation in real experiments. For this reason, we propose a detection scheme that is free of those restrictions and based on a simple geometry as shown in fig.(4.1). Our geometry benefits from its simplicity by only requiring edge states to proximity pair with a nearby superconductor.

Since intrinsic interactions such as Coulomb repulsion appear in physical systems, we include the effect in our model. Surprisingly, once interactions are present in the edge, we find universal conductance for topological superconductivity. This is in sharp contrast to the non-interacting case where the finite size effect provides size dependent non-universal conductance[85]. The physics becomes more interesting as we enter the strongly interacting regime where strong repulsive interactions spontaneously break time reversal symmetry, which can be interpreted as parafermion modes appearing at the junctions between the edge states and superconducting region[86, 87]. In order to understand the phase diagram between weakly and strongly interacting regimes we model the edge states as a Luttinger liquid and use standard renormalize group techniques[88, 89, 90, 91]. This provides us with the general phase diagram for any interaction.

We propose a new scheme to probe topological superconductivity with a control experiment where the topological superconductivity disappears. We do this without breaking time reversal symmetry and contrast the results with the case where time reversal symmetry is broken[35]. For weak repulsive interaction, we predict that the

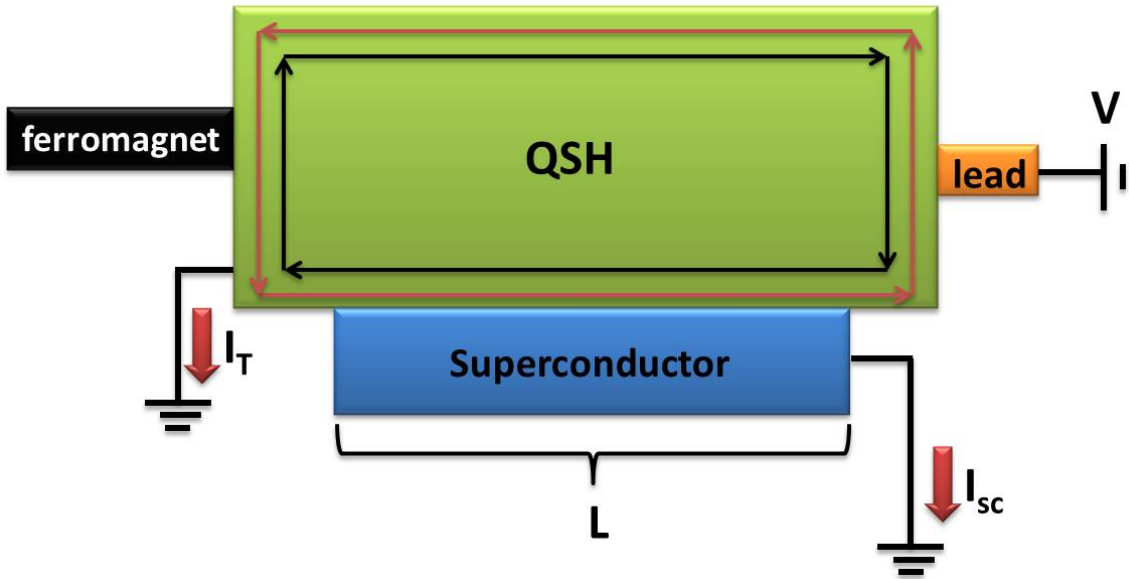


Figure 4.1: A superconductor couples to edge states of quantum spin Hall effect. The conductance of such device provides universal signatures for topological superconductivity.

conductance of the topological superconductor is insensitive to time reversal breaking, in contrast to the trivial superconductor where the conductance dramatically changes when we apply time reversal broken field.

4.2 Setup

Here we describe the minimal platform required to probe topological superconductivity. One way to engineer a 1D topological superconductor is to take edge states of a topological insulator and induce pairing through the proximity effect to a parent superconductor[4]. Fig. 4.1 shows how to construct such a setup. The device can be probed by injecting electrons through a lead into the edge states and measuring transport properties which pertain to normal transmission, I_t , and Andreev reflection I_{sc} . By analyzing the tunnelling conductance $G_t = I_t/V$ and superconductor conductance $G_{sc} = I_{sc}/V$ as a function of voltage V and temperature, we find universal conductance that only depends on the correlation length ξ induced by the proximity pairing.

The universal conductances provide a way to distinguish the topological and trivial superconductors[92]. To be more precise, we consider two physically distinct regimes characterized by the induced correlation length ξ on the edge states of the topological insulator. One regime where the superconducting region (L) on the topological insulator edge is much larger than the induced correlation length ξ , the other one is comparable or shorter than the induced correlation length. The first one ($L \gg \xi$) is approximated by an infinitely long superconductor where low energy modes do not propagate from one side to the other. This is the regime which supports topological superconductivity. The latter one ($L \approx \xi$) is given by a short superconductor where the low energy physics is well approximated by a point impurity. This is the regime where finite size effect destroys the topological properties and is essentially a trivial superconductor. Comparing the difference of conductance between long and short domains of induced pairing allows one to identify the existence of a 1D topological superconductor.

4.3 Hamiltonian of the system

To calculate the conductance in regimes, we model the 1D interacting edge states as a Luttinger liquid. Depending on the interaction strength, tunnelling across the superconductor and induced pairing, one finds that the system is driven to an array of exotic fixed points, each showing different conductance signatures. Here we construct the low energy Hamiltonian for the topological insulator edge and the superconductor. Generically it will take the form,

$$H = H_{KE} + H_{int} + H_B. \quad (4.1)$$

where H_{KE} is the kinetic part, H_{int} encodes the interactions present in the quantum spin Hall edge, and H_B is a boundary Hamiltonian, which incorporates the low energy physics induced by the superconductor. We assume the superconducting gap is much larger than any energy scale to be considered and leave it out of the effective

Hamiltonian.

The physical degrees of freedom are fermions residing on the topological insulator edge. We label them by their momentum as right- and left-moving modes denoted $\psi_{R/L}$. For now we remain faithful to the topological insulator edge and only allow perturbations which are time reversal invariant. Time reversal is an anti-unitary operator which squares to negative one and takes the form,

$$T(\psi_R) = \psi_L \quad (4.2)$$

$$T(\psi_L) = -\psi_R. \quad (4.3)$$

Although the physical degrees of freedom are fermions it is much easier to bosonize the edge so that interaction effects are simply tuned by the Luttinger parameter[93] g , with $g < 1$, $g = 1$ and $g > 1$ correspond to repulsive, non-interacting, and attractive interactions. With the goal of bosonizing the Hamiltonian in mind, we write the fermionic operator ψ in terms of bosonic field θ and φ as,

$$\psi_{R/L} \sim e^{i(\varphi \pm \theta)}. \quad (4.4)$$

where the bosonic fields satisfy the commutation relation $[\varphi(x), \theta(x')] = i\pi\Theta(x - x')$. Meanwhile, time reversal can be inferred from the fermionic operators and takes the form $T(\varphi) = -\varphi - \pi/2$ and $T(\theta) = \theta + \pi/2$.

The Hamiltonian now takes the simple form,

$$H = \frac{v}{2\pi} \int_x [g(\partial_x \varphi)^2 + g^{-1}(\partial_x \theta)^2] + H_B. \quad (4.5)$$

The integration over x is split into $(-\infty, 0)$ for the infinite superconductor limit and $(-\infty, \infty)$ for the short superconductor. In doing so one implicitly assumes that the induced superconducting gap is larger than the fermi energy of the topological insulator edge modes.

As shown in the following sections, time reversal strongly constrains the boundary conditions and boundary terms H_B in both long and short superconductors limits.

The boundary couplings H_B are found by listing all time reversal invariant terms which couple the left- and right-moving fermions at the boundary. We then bosonize these and keep only the most relevant terms in the renormalization group sense as these dominate the low energy physics. With the renormalize group equations of these perturbations in hand, we can calculate the stability of each fixed point, which allows one to access the phase diagram for any interactions. In the following sections, we illustrate the ideas of calculating stability of each fixed points in great details.

4.4 Fixed point actions for infinite superconductor

We first consider the case where the induced superconductivity on the topological insulator edge is long when compared to the induced correlation length. That is, we expect electron tunneling across the superconductor to be negligible. At the fixed point this amounts to assuming an infinitely long superconductor. As a scattering problem, the electrons have two possibilities when they approach the superconductor, they either reflect as electrons or holes, and the first is referred to normal reflection while the latter is Andreev reflection.

We can write down the boundary conditions required by perfect Andreev reflection as $\psi_R = e^{i\alpha}\psi_L^\dagger$, where $\alpha = \pm\pi/2$ is fixed by time reversal symmetry. We denote the point $x = 0$ as the boundary between the edge states and the infinite superconductor. At the boundary, $\varphi(0)$ is pinned to $\pm\pi/4$ again due to time reversal symmetry and the Andreev reflection boundary condition. For the purpose of calculating stability of each fixed point, we integrate out all the fields away from the boundary and calculate the effective Hamiltonian in terms of boundary fields Φ and Θ , as shown in Appendix A and reference by L. Fidkowski *et. al.*. Once we do so, the perfect Andreev reflection fixed point action becomes

$$S_A[\Theta] = \int \frac{d\omega}{2\pi} \frac{|\omega|}{2\pi g} \Theta_\omega \Theta_{-\omega}. \quad (4.6)$$

Andreev reflection is the only process that preserves time reversal in the long super-

conductor limit. The other process, normal reflection breaks time reversal symmetry. For this reason, it seems we will not have normal reflection if we conserve time reversal. It turns out that as interactions become very strongly repulsive, time reversal may break spontaneously. The boundary conditions required by perfect normal reflection are $\psi_R = e^{i\alpha'}\psi_L$. Once integrating out the bulk edge modes, the normal reflection fixed point action at the boundary takes the form:

$$S_N[\Phi] = \int \frac{d\omega}{2\pi} \frac{g|\omega|}{2\pi} \Phi_\omega \Phi_{-\omega}. \quad (4.7)$$

Given the fixed point actions we can analyze their stability under various time reversal preserving and time reversal breaking perturbations. Once these perturbations are bosonized we can read off their scaling dimension and understand the stability of the fixed points by renormalization group analysis.

4.4.1 Perturbing the fixed point actions with TRI terms in infinite SC case

We start with the time reversal invariant case and list all terms that could appear in the boundary Hamiltonian, H_B . The lowest order terms are:

$$\psi_R\psi_L + h.c. \sim \sin 2\varphi \quad (4.8)$$

$$\sum_{\sigma} \psi_{\sigma} i\sigma \partial_x \psi_{\sigma} + h.c. \sim \cos 2\varphi \sin 2\theta \quad (4.9)$$

$$\psi_L^{\dagger} i\partial_x \psi_L^{\dagger} \psi_R i\partial_x \psi_R + h.c. \sim \cos 4\theta \quad (4.10)$$

$$\psi_L i\partial_x \psi_L \psi_R i\partial_x \psi_R \sim \cos 4\varphi \quad (4.11)$$

where on the right hand side we have bosonized the fermionic operator. Higher order terms could appear, e.g., we could square any of the above terms; however, their scaling dimension will make them strongly irrelevant compared to the terms listed above. Thus this list is exhaustive for the low energy universal physics around the infinite superconductor fixed point. Of particular interest are the two four body terms

that are found by squaring the pairing term. As we will see they provide the leading non-trivial perturbations at the Andreev fixed point.

At the Andreev fixed point, time reversal invariance pins $\varphi(0) = \pm\pi/4$ which leaves the only non-trivial back-scattering perturbation as $\lambda \cos 4\Theta$. The coupling λ flows according to,

$$\frac{d\lambda}{dl} = \lambda(1 - 8g) \quad (4.12)$$

Thus we see that $\lambda \cos 4\Theta$ is irrelevant for $g > 1/8$ and relevant for $g < 1/8$. Hence for strong repulsive interaction where $g < 1/8$, the Andreev reflection fixed point is unstable and flows to the only other fixed point available – perfect normal reflection.

At the normal reflection fixed point, Θ is pinned due to boundary conditions. Therefore, we have perturbations that bosonize to $\tilde{\lambda}_k \cos k\Phi$, which flows as

$$\frac{d\tilde{\lambda}_k}{dl} = \tilde{\lambda}_k \left(1 - \frac{k^2}{2g}\right). \quad (4.13)$$

Such a perturbation is irrelevant for $g < k^2/2$. We know that this fixed point must be stable for $g < 1/8$ and thus we find that the maximum value k can take is $1/2$. This corresponds to a perturbation of the form $\cos \Phi/2$. Indeed, this does not naturally appear in the fermionic language. We will show that this term arises from parafermion modes being weakly bound to the edge state-superconductor interface.

To understand how these parafermion modes appear, we perform a duality transformation which takes the Andreev reflection fixed point to the normal reflection fixed point. One finds that $\cos 4\Theta$ is dual to $\cos \Phi/2$. The calculation is nearly identical to the one given in Ref.[35] and so we leave the details to Appendix B. The resulting partition sum after performing a duality on the $\cos 4\theta$ term is,

$$Z_{dual} = \int \mathcal{D}\Phi e^{-S_N[\Phi] - \int d\tau v \cos \Phi/2} \quad (4.14)$$

Furthermore, we see that the perturbation of $\cos \Phi/2$ flows according to,

$$\frac{dv}{dl} = v \left(1 - \frac{1}{8g}\right), \quad (4.15)$$

which implies that normal reflection is stable for $g < 1/8$, as anticipated. Indeed this shows that spontaneous time reversal breaking may occur for strong repulsive interactions—as the action is not time reversal invariant. This suggests that for $g < 1/8$ we spontaneously break time reversal symmetry. Because of this, we must require that our system doesn't develop any magnetization. That is, $e^{2i\theta}$ cannot gain an expectation value in this broken symmetry phase. Even stranger is the generation of $\cos \Phi/2$, which is not a local fermionic degree of freedom. This seems unphysical at first sight, but can be understood in the following way. Imagine we have a helical wire with very strongly repulsive interactions such that $\cos 4\theta$ is relevant. In this case we should imagine that the interface isn't just a helical liquid and a superconductor, but on some length scale, say δL , a region of $\cos 4\theta$ is created. This then spontaneously breaks time reversal invariance, since θ gets pinned at the boundary, and as we will see, binds a zero mode to the interface of the superconductor and the $\cos 4\theta$ region. This generates a four-fold ground state degeneracy. When δL is roughly equal to the zero modes localization length, the zero mode will couple to the helical wire and leak into the bulk of the system, and ground state degeneracy will be lost.

To see this we can consider the operator $\hat{O} = e^{i(\varphi(-\delta L) - \varphi(0))}$. For $x \in \{-\delta L, 0\}$, we have $\hat{O}\theta(x) = (\theta(x) - \pi/2)\hat{O}$. That is, it shifts the minima of the $\cos 4\theta$ potential, and since $\rho = \partial_x \theta / 2\pi$ it can be interpreted as tunnelling a charge $-e/4$ quasiparticle across the $\cos 4\theta$ region. As has been seen in previous works, the region between the superconductor and the $\cos 4\theta$ perturbation will bind a parafermion zero mode[94, 86], which we denote α . Thus we find that the parafermion mode leads to a physical perturbation of the form,

$$\delta H = v(\alpha \hat{O}^\dagger + h.c.). \quad (4.16)$$

Thus when interactions are very strong we see that a $\cos \Phi/2$ perturbation can be generated by a parafermion mode which is spontaneously created on short length scales.

symmetry	action	perturbation	dimension
TRI	S_A	$(\psi_L^\dagger i\partial\psi_L^\dagger)(\psi_R i\partial\psi_R) + h.c.$	$8g$
	S_N	$\alpha\hat{O}^\dagger + h.c.$	$1/(8g)$
TRB	S_A	$(\psi_L^\dagger\psi_R) + h.c.$	$2g$
	S_N	$\gamma(\psi_R^\dagger - \psi_R)$	$1/(2g)$

Table 4.1: We list all the possible fixed point actions, perturbations and dimension of perturbations for long superconductor limit. These actions are stable when the dimensions of their corresponding perturbations are all larger than 1. Here we denote fixed point action of normal reflection as S_N and Andreev reflection as S_A , and use γ and \hat{O} to represent Majorana and parafermion operators.

4.4.2 Perturbing the fixed point actions with TRB terms in infinite SC case

We now consider the stability of the fix point actions under time reversal breaking perturbations. The lowest order term which breaks time reversal is the back-scattering term: $V_z(\psi_L^\dagger\psi_R) + h.c.$. This term flows as $dV_z/dl = (1 - 2g)V_z$ at the Andreev reflection fixed point[35], which tells us Andreev reflection is stable to weak interactions when $1/2 < g$. For strong repulsive interaction when $g < 1/2$, the system flows to the normal reflection fixed point. We can understand this by coupling a Majorana zero modes [35] γ that appear at the ends of the topological superconductor to left/ right movers $\lambda\gamma(\psi_R^\dagger - \psi_R)$. This term flows as $d\lambda/dl = (1 - 1/(2g))\lambda$ at the normal reflection fixed point[35], which shows that normal reflection fixed point is stable when $g < 1/2$.

All the fixed point actions and their lowest order perturbations and dimension of perturbations for the infinite superconductor are summarized in table(4.1). With this table one can infer the phase diagram shown in fig.(4.2) (a) and (c). These phase diagrams show that unless we have extremely strong repulsive interactions (i.e. $g < 1/8$ for time reversal invariant and $g < 1/2$ for broken case) the Andreev reflection fixed point is always stable for the long superconductor limit. In other words, for weak interactions we will measure the universal conductance $2e^2/h$ of the topological superconductor regardless of whether time reversal symmetry is broken or not.

4.5 Fixed point actions for finite superconductor

Here we would like to contrast the conductance measurements of the infinite (topological) superconductor with that of a finite or short induced superconductivity. For the short superconductor boundary modes either end will be coupled and allow for non-zero conductance transmission through the superconducting regime. When analyzed in the renormalization group sense, this problem maps onto an impurity problem of the edge states to the topological insulator. This provides a control experiment where effects of the topological superconductor will disappear as we crossover from the limit of a long superconducting regime to that of a short one. A feature of this experiment is that we don't need to see a topological phase transition in order to verify the existence of a topological superconductor. Instead we propose investigating the crossover by killing the topological superconductor with finite size effects.

We analyze the short superconductor limit in the same way we did the infinite one: we first characterize all fixed point actions and then consider various symmetry allowed perturbations. These fixed point actions will describe the dynamics of the boundary fields which can now couple across the superconductor. It turns out that the only stable fixed points are perfect normal transmission, perfect Andreev reflection, and perfect normal reflection. The latter two fixed points essentially split the superconductor into two halves, each characterized by Andreev or normal reflection individually. Therefore, the fixed point actions are the same as two copies of eq.(4.6) and eq.(4.7) at each side. We denote them as $S_{N\oplus N} = S_N[\Phi_1] + S_N[\Phi_2]$ for normal reflection and $S_{A\oplus A} = S_A[\Theta_1] + S_A[\Theta_2]$ for Andreev reflection, with Φ_1, Θ_1 as boundary fields at one side and Φ_2, Θ_2 for the other side.

The normal transmission fixed point amounts to considering the superconductor as a point impurity in the edge states. Hence continuity requires the boundary fields to be the same at each side (i.e. $\Phi_1 = \Phi_2, \Theta_1 = \Theta_2$, which we call Φ and Θ , respectively). Again the fixed point action can be found by integrating out fields

away from the impurity, which leaves the fixed point action:

$$S_o[\Phi, \Theta] = \int \frac{d\omega}{2\pi} \frac{|\omega|}{\pi} (g\Phi_\omega\Phi_{-\omega} + g^{-1}\Theta_\omega\Theta_{-\omega}). \quad (4.17)$$

With these fixed point actions in hand, we can analyze the stability under various perturbations in the same way as before. Once doing so we will be able to map out the corresponding phase diagram for short (impurity) superconductor.

4.5.1 Perturbing the fixed point actions with TRI terms in short SC case

Again we determine all possible perturbations by demanding time reversal invariance and compare the results when time reversal breaking terms are included. Here we present an exhaustive list of the most relevant two particle time reversal invariant terms such as Andreev transmission and normal tunneling:

$$\psi_{R1}\psi_{R2} + \psi_{L1}\psi_{L2} \sim \cos(\varphi_1 + \varphi_2) \sin(\theta_1 + \theta_2) \quad (4.18)$$

$$\psi_{R1}^\dagger\psi_{R2} + \psi_{L1}^\dagger\psi_{L2} \sim \cos(\varphi_2 - \varphi_1) \sin(\theta_2 - \theta_1) \quad (4.19)$$

$$\psi_{R1}\psi_{L2} - \psi_{L1}\psi_{R2} \sim \sin(\varphi_1 + \varphi_2) \cos(\theta_1 - \theta_2) \quad (4.20)$$

$$\psi_{R1}^\dagger\psi_{L2} - \psi_{L1}^\dagger\psi_{R2} \sim \sin(\varphi_2 - \varphi_1) \cos(\theta_2 + \theta_1) \quad (4.21)$$

With these perturbations in hand, we first assess the stability of the perfect Andreev reflection fixed point. This fixed point is characterized by boundary conditions $\varphi_j = \pm\pi/4$ with the fixed point action $S_{A\oplus A}$. The first and last terms in the list above drop out due to time reversal invariance. The leading perturbations are $\lambda_1 \cos(\Theta_2 - \Theta_1)$ and $\lambda_1 \sin(\Theta_2 - \Theta_1)$. Both have the same scaling dimension. The coupling λ_1 of these perturbations flows according to,

$$\frac{d\lambda_1}{dl} = \lambda_1(1 - g). \quad (4.22)$$

These flow equations tells us that Andreev reflection fixed point is stable under attractive interactions. For repulsive interactions, Andreev reflection is not stable, and therefore the system will flow to one of the other two possible fixed points: normal reflection and normal transmission fixed points. Because normal reflection breaks time reversal symmetry, normal transmission is the only possible fixed point for a time reversal invariant system. We can check this argument by using the same perturbation analysis as before. The lowest order perturbation at the normal transmission fixed for g close to 1 is,

$$\psi_{R1}\psi_{L2} - \psi_{L1}\psi_{R2} \sim \lambda'_2 \sin(2\Phi) \quad (4.23)$$

which flows according to,

$$\frac{d\lambda'_2}{dl} = \lambda'_2 \left(1 - \frac{1}{g}\right). \quad (4.24)$$

This shows us that the normal transmission fixed point is stable for $g < 1$ and unstable for $g > 1$. For strong repulsive interactions time reversal symmetry can be broken spontaneously. We can see this by analyzing the back-scattering term under renormalization. The lowest order symmetry allowed back-scattering perturbation is:

$$(\psi_{R1}^\dagger \psi_{L2})^2 + (\psi_{L1}^\dagger \psi_{R2})^2 + h.c. \sim v \cos 4\theta \quad (4.25)$$

which flows according to

$$\frac{dv}{dl} = v(1 - 4g). \quad (4.26)$$

This back-scattering term makes normal transmission unstable for $g < 1/4$, and hence the perfect normal transmission fixed point is stable for $g \in (1/4, 1)$. For $g < 1/4$ this term becomes relevant and the wire effectively splits into two disconnected regions separated by $\cos 4\theta$ governed by the normal reflection fixed point action $S_{N \oplus N}$. We summarize this discussion by plotting the phase diagram in fig.(4.2)(b) for a short superconductor under time reversal symmetry.

4.5.2 Perturbing the fixed point actions with TRB terms in finite SC case

Another advantage of the system is that it is relatively straightforward to break time reversal symmetry with an external field. This can be used as another knob to distinguish the topological superconductor from the short superconductor. For weak interactions, the topological superconductor is stable to time reversal breaking terms while the short superconductor is not. Thus tuning an external magnetic field and performing conductance measurements allows one to tell if the induced superconductor is topological or not.

Breaking time reversal symmetry corresponds to allowing local back-scattering terms such as $V_z(\psi_{R1}^\dagger\psi_{L1} + \psi_{R2}^\dagger\psi_{L2}) + h.c.$. The normal transmission fixed point is unstable to such perturbations, since it has scaling dimension g and is therefore unstable for repulsive interactions. Meanwhile the pairing term $A(\psi_{R1}\psi_{L2} - \psi_{L1}\psi_{R2}) + h.c.$ has scaling dimension $1/g$ and is therefore unstable to attractive interactions as well. Therefore, the normal and Andreev reflection fixed points are the only possible stable fixed points as shown in the phase diagram fig.(4.2)(d). The phase boundary between normal reflection and Andreev reflection can be calculated by using standard renormalization group methods as we did before. To summarize these calculations we list all the perturbations and their dimensions at each fixed point in table(4.2). In this table, the dimensions of perturbations in time reversal broken case indicate that normal reflection is stable to repulsive interactions while Andreev reflection is stable to attractive interactions.

4.6 Conductance

Now that we have mapped out the phase diagram, we are in a position to analyze small perturbations to the fixed point actions and look at the corresponding corrections to the conductance. This can be done very precisely, as was done in Ref.[89], but in this case dimensional analysis gives the same results [88, 89, 90, 95, 96]. We also restrict

symmetry	action	perturbation	dimension
TRI	$S_{A\oplus A}$	$(\psi_{R1}^\dagger \psi_{R2} + \psi_{L1}^\dagger \psi_{L2}) + h.c.$	g
		$(\psi_{R1} \psi_{L2} - \psi_{L1} \psi_{R2}) + h.c.$	g
	S_0	$(\psi_{R1}^\dagger \psi_{L2})^2 + (\psi_{L1}^\dagger \psi_{R2})^2 + h.c.$	$4g$
		$\psi_{R1} \psi_{L2} - \psi_{L1} \psi_{R2} + h.c.$	$1/g$
	$S_{N\oplus N}$	$\psi_{R1} \psi_{R2} + \psi_{L1} \psi_{L2} + h.c.$	$1/g$
$\psi_{R1}^\dagger \psi_{R2} + \psi_{L1}^\dagger \psi_{L2} + h.c.$		$1/g$	
$\psi_{R1} \psi_{L2} - \psi_{L1} \psi_{R2} + h.c.$		$1/g$	
$\psi_{R1}^\dagger \psi_{L2} - \psi_{L1}^\dagger \psi_{R2} + h.c.$		$1/g$	
$\hat{O}_1^\dagger \hat{O}_2 + h.c.$		$1/(4g)$	
TRB	$S_{A\oplus A}$	$(\psi_{R1}^\dagger \psi_{R2} + \psi_{L1}^\dagger \psi_{L2}) + h.c.$	g
		$(\psi_{R1} \psi_{L2} - \psi_{L1} \psi_{R2}) + h.c.$	g
	S_0	$\psi_{R1}^\dagger \psi_{L1} + \psi_{R2}^\dagger \psi_{L2} + h.c.$	g
		$\psi_{R1} \psi_{L2} - \psi_{L1} \psi_{R2} + h.c.$	$1/g$
	$S_{N\oplus N}$	$\psi_{R1} \psi_{R2} + \psi_{L1} \psi_{L2} + h.c.$	$1/g$
$\psi_{R1}^\dagger \psi_{R2} + \psi_{L1}^\dagger \psi_{L2} + h.c.$		$1/g$	
$\psi_{R1} \psi_{L2} - \psi_{L1} \psi_{R2} + h.c.$		$1/g$	
$\psi_{R1}^\dagger \psi_{L2} - \psi_{L1}^\dagger \psi_{R2} + h.c.$		$1/g$	

Table 4.2: We list all the possible fixed point actions (normal transmission S_0 , normal $S_{N\oplus N}$ and Andreev reflection $S_{A\oplus A}$), and lowest order perturbations for short superconductor limit. These actions are stable when the dimensions of their corresponding perturbations are all larger than 1. \hat{O} is parafermion operator.

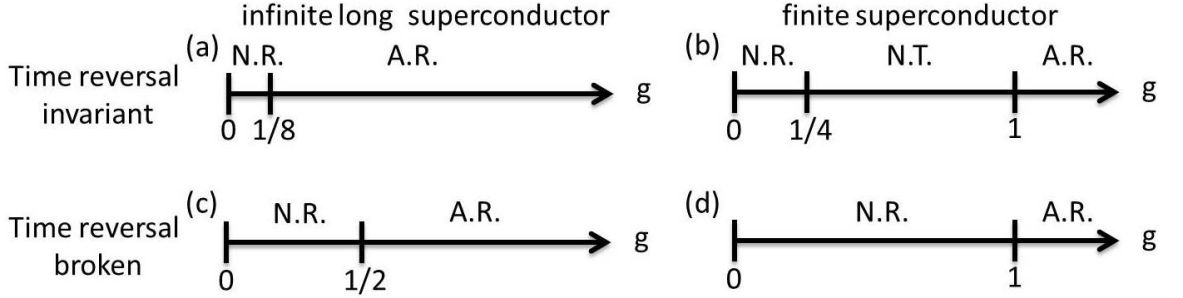


Figure 4.2: Phase diagram. Here g is the Luttinger liquid parameter. N.R., N.T., and A.R. correspond to normal reflection, normal transmission, and Andreev reflection. Each phase provides unique signatures such as tunneling conductance $G_t = I_t/V$ and superconductor conductance $G_{sc} = I_{sc}/V$ to characterize them. For example, normal reflection, normal transmission and Andreev reflection are characterized by $(G_t, G_{sc}) = (0, 0)$, $(\frac{e^2}{h}, 0)$ and $(0, \frac{2e^2}{h})$, respectively.

ourselves to the realistic regime of small repulsive interactions. This corresponds to a Luttinger parameter $1 - \delta < g < 1$ for $\delta \ll 1$.

4.6.1 Time reversal invariant case

We begin by investigating the time reversal invariant fixed points. We have two cases: the long (topological) superconducting limit, and the short (trivial) limit, where the fixed point actions are dominated by Andreev reflection and normal transmission, respectively.

In the long superconductor limit the lowest order time reversal invariant perturbation at perfect the Andreev reflection fixed point is the Umklapp back-scattering[86] term:

$$\delta H = \lambda \psi_L^\dagger i \partial_x \psi_L^\dagger \psi_R i \partial_x \psi_R + h.c. \sim \lambda \cos(4\Theta). \quad (4.27)$$

This perturbation serves to decrease the conductance G_{sc} by back-scattering. To find the lowest order corrections to the conductance we employ the Kubo formula. This requires finding the current-current correlator. Thus we start by finding the current operator, \hat{I} defined by,

$$\hat{I} = \frac{d\hat{N}}{dt} = i[\delta\hat{H}, \hat{N}] \propto \lambda \quad (4.28)$$

where number operator $\hat{N} = \psi_L^\dagger \psi_L + \psi_R^\dagger \psi_R$. Here we have used the fact that $\delta\hat{H}$ is proportional to λ .

We are now positioned to find the deviation of the conductance δG by invoking the Kubo formula[97, 98]

$$\delta G = \lim_{\omega \rightarrow 0} \frac{1}{\omega_n} \int_0^\beta d\tau \langle T_\tau \hat{I}(\tau) \hat{I}(0) \rangle |_{i\omega_n \rightarrow \omega + i\eta} \propto \lambda^2 \quad (4.29)$$

where the λ^2 comes from the scaling of the conductance with λ . We can calculate the coupling strength λ from the flow equation shown in eq(4.12). To solve this we

integrate l to the cut off l_{max} , where we get the tunneling strength λ :

$$\lambda = (e^{-l_{max}})^{8g-1}. \quad (4.30)$$

At zero temperature, the flow has cut off at the voltage V , which means $e^{-l_{max}} \sim V$. By this substitution, we find the relation between the coupling strength and voltage to be

$$\lambda = (V)^{8g-1}. \quad (4.31)$$

Squaring the coupling strength, we get the perturbed conductance δG :

$$\delta G \propto \lambda^2 \propto (V)^{16g-2} \quad (4.32)$$

We can calculate the total conductance by summing the non-perturbed conductance—which is $G_{sc} = 2e^2/h$ for Andreev reflection fixed point, and perturbed conductance in eq.(4.32). This gives us the total conductance

$$G_{sc} = G_{sc}^0 + \delta G = \frac{e^2}{h} \left(2 - \left(\frac{V}{V^*} \right)^{16g-2} \right). \quad (4.33)$$

This signature indicates how the conductance changes at fixed Luttinger parameter as a function of voltage. Hence, in principle, it can be used in experiments to infer what the Luttinger parameter is of the physical system. We plot what the scaling form of this total conductance is as a function of voltage in Fig(4.3)(a).

We now consider the short superconductor limit where electrons can hop past the superconducting region with strength t . This provides two regimes of interest: one where the voltage is small compared to t and the other where it is large compared to t . Intuitively large t compared to voltage promotes normal transmission (i.e., $G_t = e^2/h$). When the voltage is large compared to t normal transmission is suppressed while Andreev reflection is enhanced (i.e., $G_{sc} = 2e^2/h$). An easy way to convince yourself of this fact is to take the $t \rightarrow 0$ limit, where the edge states are parsed and we

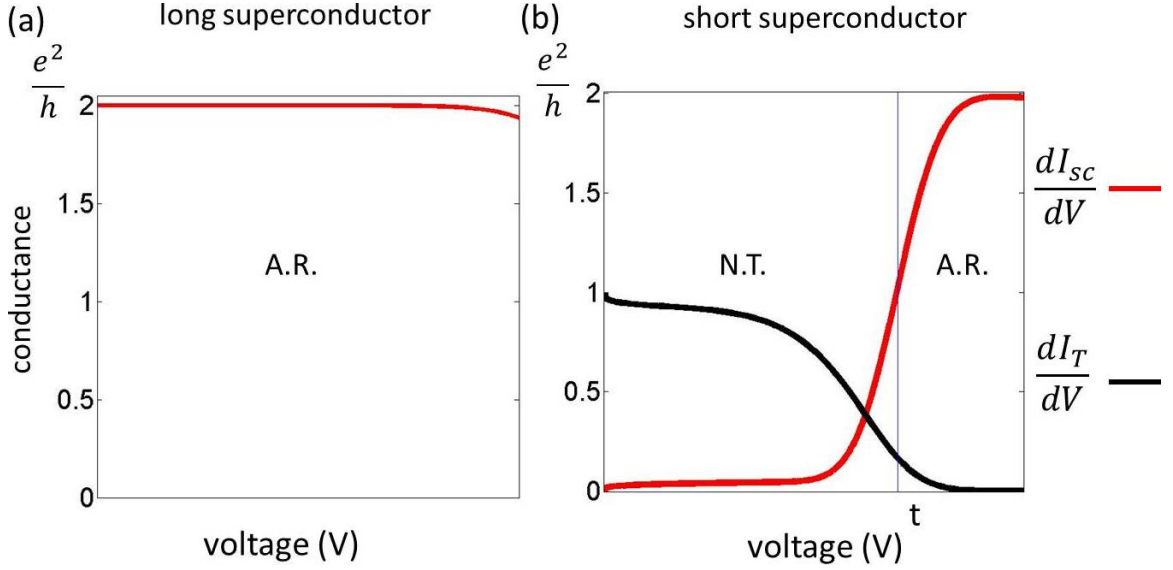


Figure 4.3: Conductance under weak repulsive interactions and time reversal invariant perturbations, by analyzing the power law of deviations in conductance, we can tell the interactions strength g in the edge states. (a) Conductance G_{sc} of a topological superconductor. Here we plot G_{sc} according to eq(4.33). (b) Conductance of a trivial superconductor. G_{sc} and G_t are plotted according to eq.(4.35).

are driven back to the infinite superconductor limit. A novel result is that we can tune between a topological superconductor and a trivial one by appropriately adjusting the voltage. One should note, however, that there is no phase transition, rather, just a crossover where finite size effects dominate the trivial regime and disappear as we ramp up the voltage to find ourselves in the topological superconductor limit.

The deviation of conductance that comes from lowest order perturbation in normal transmission fixed point is the Andreev tunneling term, as shown in table(4.2).

$$\delta H = \lambda(\psi_{R1}\psi_{L2} - \psi_{L1}\psi_{R2}) + h.c. \quad (4.34)$$

This perturbation has coupling constant with dimension $(\frac{1}{g})$. Squaring the coupling constant gives us the correction of conductance as $\delta G \sim \lambda^2 \sim V^{2(\frac{1}{g}-1)}$. Because Andreev tunneling describes an electron tunneling out from the superconductor as a hole contributing to I_t , we must have two electrons contribute to I_{sc} in order to

conserve charge. Therefore, this correction will modify both G_t and G_{sc} ,

$$\begin{aligned} G_t &\approx \frac{e^2}{h} \left(1 - \left(\frac{V}{t}\right)^{2(\frac{1}{g}-1)} - \left(\frac{V}{t}\right)^{(8g-2)} \right) && \text{if } V < t \\ G_{sc} &\approx \frac{2e^2}{h} \left(\frac{V}{t}\right)^{2(\frac{1}{g}-1)} && \text{if } V < t \end{aligned} \quad (4.35)$$

We plot this modification of conductances in fig.(4.3) (b), in the regime of voltage V smaller than the tunneling coupling t .

4.6.2 Time reversal broken case

Because the conductance of a topological superconductor and a trivial superconductor respond to magnetic fields in a very different way, we can use this as an identification process to reveal topological superconductivity.

The key ingredients here are that the conductance of topological superconductor is immune to time reversal broken field, while conductance of trivial superconductor dramatically changes when we apply the magnetic field. One can understand this in the following way: Andreev reflection is the only process in topological superconductor without breaking time reversal symmetry. Once we break time reversal symmetry, Majorana fermions appear at the end of topological superconductor, which again provides the channels for Andreev reflection. For this reason, conductance of topological superconductor G_{sc} always quantized as $2e^2/h$ at zero bias regardless time reversal is broken or not. As for trivial superconductor, it is stable in normal transmission fixed point with time reversal invariant and flows to normal reflection fixed point as time reversal is broken. Hence, the tunneling conductance G_t jumps between e^2/h to 0 at zero bias as we apply magnetic field.

To check the argument that we demonstrate above, We first take a look of conductance in topological superconductor when we break time reversal symmetry. As shown in phase diagram Fig.4.2(c), for weak interactions, we will have the system in Andreev reflection fixed point. The lowest order perturbation is a back scattering term with dimension $2g$, as shown in Table.4.1. The back scattering term provides

deviation of conductance with power law $4g - 2$, which leads to conductance being

$$G_{sc} \approx \frac{2e^2}{h} \left(1 - \left(\frac{V}{V^*} \right)^{4g-2} \right) \quad (4.36)$$

We plot conductance of topological superconductor with time reversal broken in Fig.4.4(a). One can compare this result with trivial superconductor. We start from a short superconductor limit with time reversal invariant. This is the case where we have already derived conductance in fig.(4.3)(b). We then start to break time reversal symmetry by applying magnetic field, and assume that time reversal broken term such as Zeeman coupling V_z is smaller than the hopping strength t . When voltage is larger than time reversal broken field V_z , we can neglect time reversal broken field. Therefore, the conductance of broken case will be the same as the invariant one in this limit. In other words, Fig.4.3(b) and Fig.4.4(b) have the same power law when voltage is larger than time reversal broken field V_z .

In the other limit where the voltage is smaller than time reversal broken field, the electrons begin to do normal reflection. This implies that tunneling conductance G_t goes to zero at zero bias. The perturbed conductance can be extract from flow equations of perturbations. With dimensional analysis and perturbations shown in table(4.2), we get the following perturbed conductances:

$$G_t \approx \frac{e^2}{h} \left(\frac{V}{V_z} \right)^{\frac{2}{g}-2} \quad \text{if } V < V_z \quad (4.37)$$

$$G_{sc} \approx \frac{2e^2}{h} \left(\frac{V}{V_z} \right)^{\frac{2}{g}-2} \quad \text{if } V < V_z \quad (4.38)$$

Surprisingly, once we break time reversal symmetry, the conductance of trivial superconductor is not a monotonic function of voltage. As one can see in Fig.4.4(b), we predict that the tunneling conductance G_t has maximum value at the voltage between the strength of time reversal broken field V_z and hopping strength t . Comparing the tunneling conductance G_t between time reversal invariant and broken case in Fig.4.3(b) and Fig.4.4(b), we find that tunneling conductance G_t jumps from e^2/h to zero at zero bias as we break time reversal symmetry.

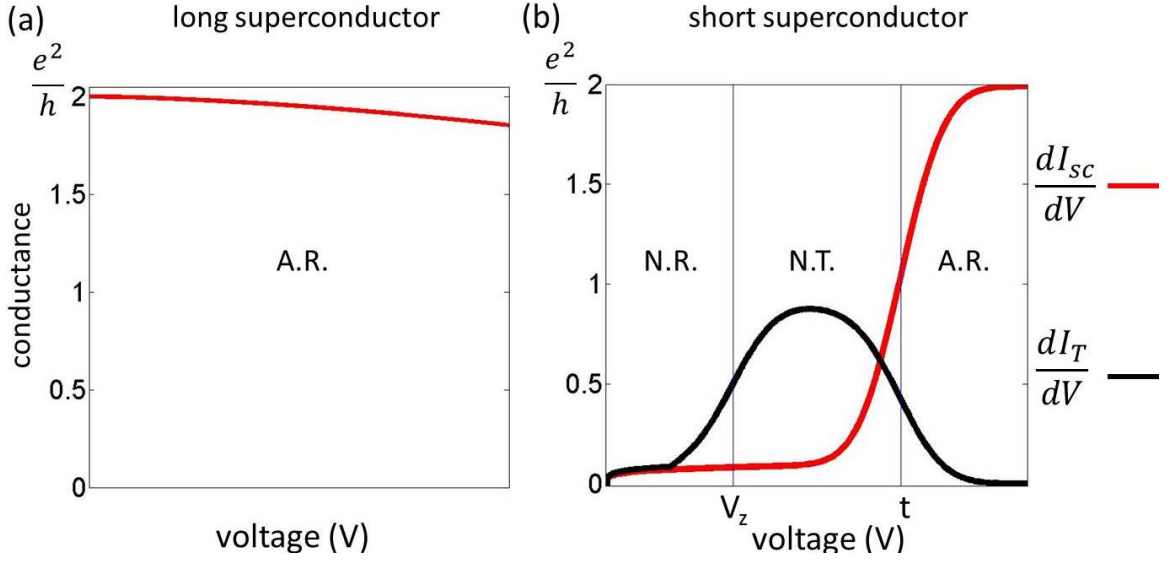


Figure 4.4: Conductance for time reversal broken case. Here V_z is time reversal breaking term (backward scattering term), and λ is tunneling coupling.

4.7 Conclusions

In conclusion, we show that interactions provided universal conductances for revealing topological superconductivity. To do that, we compare to two regimes of size of superconductors. One has superconductor length larger than induced correlation length and the other one is smaller. Long superconductor limit is the regime where we have topological superconductivity. In contrast, the finite size effect destroys topological superconductivity in the short superconductor limit. To use conductance for revealing topological superconductivity, we show that with weak repulsive interactions, conductance of topological superconductor is not sensitive with magnetic field, in contrast to trivial superconductor, where it is very sensitive

4.8 Appendix: Parafermion zero mode

In the superconducting region $\varphi(x) = n_\varphi\pi + \pi/4$ and in the $\cos 4\theta$ region we have $\theta(x) = n_\theta\pi/2$ for $n_\varphi, n_\theta \in \mathbb{Z}$. Using the commutation relations for φ and θ we find that $[n_\varphi, n_\theta] = 2i/\pi$. Using Clarke et al we find the zero mode bound to the domain

will to be of the form:

$$\alpha = e^{i\pi(n_\varphi+n_\theta/2)} \quad (4.39)$$

up to an overall phase. This operator commutes with the Hamiltonian and leads to a four fold ground state degeneracy of the Hamiltonian. It is useful to note that $T(n_\varphi) = -n_\varphi - 1/2$ and $T(n_\theta) = n_\theta + 1$, and the gauge symmetry $(\phi, \theta) \rightarrow (\phi + \pi, \theta + \pi)$ yields $n_\varphi \rightarrow n_\varphi + 1$ and $n_\theta \rightarrow n_\theta + 2$. As we shrink the length of the perturbed region the zero mode can couple to the Luttinger liquid by tunnelling a fractional fractional charge. To see this we consider the following operator relation:

$$e^{i\lambda\varphi(x)}\theta(x') = (\theta(x') - \lambda\pi\Theta(x-x'))e^{i\lambda\varphi(x)}. \quad (4.40)$$

It shows us that $e^{i\lambda\varphi}$ creates a kink in θ of size $-\lambda\pi$. By noting that the charge density is $\rho = \partial x\theta/2\pi$ we see that it actually creates a quasiparticle of charge $-\lambda/2$. Thus a physical tunnelling term between the zero mode and the Luttinger liquid will be of the form $\hat{O} = e^{i\lambda(\varphi(0)-\pi n_\varphi)}$, which destroys a charge $e\lambda/2$ quasiparticle at one side of the $\cos 4\theta$ region and creates it at the other. For $\lambda = 1/2$ may think of this as an operator which toggles us between the minima of the $\cos 4\theta$ potential. For $\lambda = 1$ it shifts by two minima; however, this coupling will always be a less relevant perturbation to the normal fixed point under RG flow. For $\lambda = 1/2$ the operator \hat{O} and α satisfy,

$$\hat{O}\alpha = e^{-i\pi/2}\alpha\hat{O} \quad (4.41)$$

showing that they are indeed conjugate variables with \mathbb{Z}_4 statistics. With this, we find a few reasonable looking perturbations: $\hat{O} + h.c.$, $\alpha + h.c.$, $\hat{O}\alpha + h.c.$ and $\hat{O}\alpha^\dagger + h.c.$. The most reasonable looking one is:

$$\delta H = v(\hat{O} + \hat{O}^\dagger) \quad (4.42)$$

We also require that this perturbation satisfies TRI, and hence end up with:

$$\delta H = v \cos \frac{(\Phi - \pi n_\varphi)}{2}. \quad (4.43)$$

Thus we see that a $\cos \Phi/2$ perturbation to the Hamiltonian can be generated by a \mathbb{Z}_4 zero mode.

4.9 Appendix: Perfect Andreeve reflection

Consider a long superconductor couples to a Luttinger liquid. We are going to calculate conductances at Andreeve reflection and normal reflection fixed points. Let's first start from perfect Andreeve reflection fixed point case. Similar to what C. L. Kane and M. P. A. Fisher did in their paper [89], we write down Andreeve fixed point action as

$$S_A = \int \frac{dw}{2\pi} \frac{|\omega|}{2\pi g} |\Theta_\omega|^2 \quad (4.44)$$

To calculate the current, we couple the vector potential $a(\tau)$ and current density $j(\tau)$ to form the source term. And we add this source term into our action

$$S_S = i \int_0^\beta d\tau a(\tau) j(\tau) \quad (4.45)$$

Here τ is the imaginary time (i.e. $\tau = it$).

In order to calculate partition function Z , we write the current density $j(\tau)$ in terms of Θ as $j(\tau) = \frac{e}{\pi} \partial_\tau \Theta(\tau)$. The total action S_t is the sum of both fixed point action and source term

$$S_t = S_A + S_S \quad (4.46)$$

This action allows us to calculate the partition function as

$$\begin{aligned}
Z &= \int \mathcal{D}\Theta e^{-S_t} \\
&= \int \mathcal{D}\Theta \exp \left(- \int \frac{d\omega}{2\pi} \frac{|\omega|}{2\pi g} |\Theta_\omega|^2 + \frac{e}{\pi} \int \frac{d\omega}{2\pi} \omega a(-\omega) \Theta(\omega) \right) \\
&= \exp \left(- \int \frac{d\omega}{2\pi} \frac{ge^2\omega}{2\pi} |a_\omega|^2 \right) \\
&= \exp \left(- \frac{ge^2}{2\pi i} \int d\tau a(\tau) \partial_\tau a(\tau) \right)
\end{aligned} \tag{4.47}$$

In last step we integrate out the Θ field. The partition function becomes a function of the vector potential a that we add in the source term in eq.(4.45). With this partition function in hand, we can calculate the expectation value of the current density as

$$\langle j \rangle = - \frac{\delta \ln Z}{\delta a(\tau)} = g \frac{2e^2}{2\pi} \frac{\partial a(\tau)}{i\partial\tau} = g \frac{2e^2}{2\pi} \frac{\partial a(t)}{\partial t} \tag{4.48}$$

We set $\frac{\hbar}{2\pi} = \hbar = 1$ in the Hamiltonian at the beginning. As we reinstall the unit back to our formula $2\pi = h$, the current density becomes

$$\langle j \rangle = g \frac{2e^2}{h} \frac{\partial a(t)}{\partial t} \tag{4.49}$$

From what we learn in electro statics, time derivative of a vector potential a is electric field E (i.e. $E = \partial a / \partial t$). Therefore our current density becomes

$$\langle j \rangle = g \frac{2e^2}{h} E \tag{4.50}$$

This expression of the current density allows us to calculate the conductance G_0 as

$$G_0 = I/V = j/E = g \frac{2e^2}{h} \tag{4.51}$$

This conductance is what we expect. In reality, The experiment always done by coupling the Luttinger liquid with normal metal lead. Therefore, the conductance will modify into $\frac{2e^2}{h}$ as point out by ref.[99, 100].

Because the system will flow away from fixed point as we include the relevant perturbations. We therefore calculate how conductance changes as we include the perturbations at the junction between Luttinger liquid and superconductor.

4.10 Appendix: Perfect normal reflection

The boundary condition of perfect normal reflection is $\psi_L(x=0) = \psi_R(x=0)$. Since $\psi_R/L = e^{i(\phi \pm \theta)}$, this gives $\Theta = 0 \bmod \pi$. This boundary condition immediately gives zero current as we use current formula $j = \frac{e}{\pi} \partial_\tau \Theta(\tau) = 0$, which means zero conductance at perfect normal reflection fixed point.

We can prove this zero conductance in a more rigorous way by evaluation current from $j = \delta \ln Z / \delta a$. As we will see, the vector potential $a(\tau)$ only affects the perturbations in normal reflection fix point action. Due to the fact that perturbation comes from the interaction between Luttinger liquid and superconductor. This implies the conductance will always vanish in normal reflection fix point if there is no interaction at the junction. We begin this calculation by doing a duality transformation of Andreev reflection action:

$$\begin{aligned}
 S(\Theta) &= S_A(\Theta) + S_S(\Theta) + 2\lambda \int d\tau \cos(4\Theta) \\
 &= \int \frac{d\omega}{2\pi} \frac{|\omega|}{2\pi g} |\Theta_\omega|^2 + \frac{ie}{\pi} \int d\tau a(\tau) \partial_\tau \Theta \\
 &\quad + 2\lambda \int d\tau \cos(4\Theta)
 \end{aligned} \tag{4.52}$$

Put this action into the formula of partition function $Z = \int \mathcal{D}\Theta e^{-S}$, and use the Villain approximation in action:

$$e^{-2\lambda \cos 4\Theta} \rightarrow e^{-2\lambda} \sum_{n \in \mathbb{Z}} e^{\lambda(4\Theta - 2\pi n)^2} \tag{4.53}$$

Then using a Hubbard Strotonovitch field $\rho = \frac{\partial_\tau \Phi}{2\pi}$ to decouple the quadratic term,

$$\int \mathcal{D}\rho e^{-\int d\tau (\rho^2/\lambda + 2i\rho(4\Theta - 2\pi n(\tau)))} = e^{\lambda(4\Theta - 2\pi n(\tau))^2}$$

The term $\sum_n e^{2i\rho 2\pi n} = \sum_n e^{2in\partial_\tau \Phi}$ requires $\partial_\tau \Phi = 0$. Gauge invariant further requires $\Phi = Z\pi$. We can impose this condition by add $v \cos(2\Phi)$ into the action. After these steps, the partition function Z becomes

$$Z = \int \mathcal{D}\Phi \mathcal{D}\Theta \exp \left(- \int \frac{d\omega}{2\pi} \frac{|\omega|}{2\pi g} |\Theta_\omega|^2 + \frac{\omega}{\pi} (4\Phi + ea)\Theta_\omega + \int d\tau v \cos(2\Phi) \right)$$

Replace $4\Phi \rightarrow \Phi'$ and integrate out Θ field, and the partition function becomes

$$Z = \int \mathcal{D}\Phi' \exp \left[- \int \frac{d\omega}{2\pi} \frac{g|\omega|}{2\pi} |\Phi' + ea|^2 + \int d\tau v \cos \left(\frac{\Phi'}{2} \right) \right]$$

Replace $\Phi' + ea = \tilde{\Phi}$, and we get the normal reflection action with vector potential $a(\tau)$ inside the relevant perturbation:

$$Z = \int \mathcal{D}\tilde{\Phi} \exp \left[- \int \frac{d\omega}{2\pi} \frac{g|\omega|}{2\pi} |\tilde{\Phi}|^2 + \int d\tau v \cos \left(\frac{\tilde{\Phi} - ea}{2} \right) \right]$$

This partition function tells us, without perturbation (i.e. $v = 0$), that the current $j = \delta \ln Z / \delta a = 0$. We therefore conclude the conductance at normal fixed point could only be nonzero if we have interaction between superconductor and Luttinger liquid. To calculate current, we can expand this partition function with Taylor series (see Appendix A):

$$\begin{aligned} Z &= \\ Z_0 &\left(1 + \frac{v^2}{2} \left(\frac{\pi\alpha/\beta}{\sin(\pi(\tau_1 - \tau_2)/\beta)} \right)^{\frac{1}{4g}} \cos \left(\frac{e}{2} (a(\tau_1) - a(\tau_2)) \right) \right. \\ &\left. + \mathcal{O}(v^3) \right) \end{aligned} \tag{4.54}$$

Taking the derivative of this partition function ($j = \delta \ln Z / \delta a$), we get the current as

$$\begin{aligned} I &= \frac{\delta \ln Z}{\delta a(\tau)} \\ &= \frac{v^2}{2} \int_0^{i\beta} idt \sin\left(\frac{e}{2}(a(t) - a(t'))\right) (P^+ + P^-) \end{aligned}$$

Where $P^+ = \left(\frac{\pi\alpha/\beta}{\sin(i\pi(t_1-t_2)/\beta)}\right)^{\frac{1}{4g}}$, and $P^- = \left(\frac{\pi\alpha/\beta}{\sin(i\pi(-t_1+t_2)/\beta)}\right)^{\frac{1}{4g}}$. In DC limit, the vector potential $a = Vt$ where V is the voltage. With this information in hand, we can extract the current at zero temperature limit as $I \sim V^{\frac{1}{4g}-1}$, and give the conductance as $G \sim V^{\frac{1}{4g}-2}$. Similarly, we can also extract current at zero voltage limit $I \sim T^{\frac{1}{4g}-1}$, and give the conductance as $G \sim T^{\frac{1}{4g}-2}$.

We can actually get this result by using dimensional analysis. To do that, we notice the RG equation for perturbation $v \cos(m\Phi)$ in normal reflection fixed point is

$$\frac{dv}{dl} = v \left(1 - \frac{m^2}{2g}\right) \quad (4.55)$$

By calculating the coupling strength v gives the conductance as

$$\delta G \propto v^2 = (V)^{2(m^2/(2g)-1)} \quad (4.56)$$

Since $\cos(\Phi/2)$ is the relevant perturbation, we put $m = 1/2$ in eq.(4.55). This gives the conductance at normal reflection fixed point as

$$G \sim (V)^{(\frac{1}{4g}-2)} \quad (4.57)$$

4.11 Appendix: Perfect normal transmission

In short superconductor limit, the fixed point is perfect normal transmission. We can write down its action as

$$S_T = \int \frac{d\omega}{2\pi} \frac{|\omega|}{\pi} (g|\Phi_\omega|^2 + g^{-1}|\Theta_\omega|^2) \quad (4.58)$$

To calculate conductance, we add that the source term $S_S = \int_0^\beta d\tau a(\tau)j(\tau)$, and replace current density as $j(\tau) = \frac{e}{\pi}\partial_\tau\Theta(\tau)$. The calculation is the same as perfect Andreeve reflection case except replacing $g \rightarrow g/2$ in the action of perfect Andreeve reflection. We can therefore get the unperturbed conductance as

$$G_0 = g \frac{e^2}{h} \quad (4.59)$$

To calculate the perturbed conductance, we notice the relevant perturbations for normal transmission are

$$\begin{aligned} \eta(\psi_{R1}\psi_{R2} + \psi_{L1}\psi_{L2}) &\sim \eta \cos(\phi_1 + \phi_2) \sin(\theta_1 + \theta_2) \\ &\sim \eta \cos(2\Phi) \sin(2\Theta) \end{aligned} \quad (4.60)$$

$$\begin{aligned} \xi(\psi_{R1}\psi_{L2} - \psi_{L1}\psi_{R2}) &\sim \xi \sin(\phi_1 + \phi_2) \cos(\theta_1 - \theta_2) \\ &\sim \xi \sin(2\Phi) \end{aligned} \quad (4.61)$$

The RG equations for the coupling are

$$\begin{aligned} \frac{d\eta}{dl} &= \eta(1 - g - 1/g) \\ \frac{d\xi}{dl} &= \xi(1 - 1/g) \end{aligned} \quad (4.62)$$

We solve these RG equations and set the voltage as cut-off when we integrate over l , and we get

$$\begin{aligned} \eta &= (V)^{g+1/g-1} \\ \xi &= (V)^{1/g-1} \end{aligned} \quad (4.63)$$

Current-current correlation gives conductance as

$$\begin{aligned} \delta G_\eta &\propto (V)^{2g+2/g-2} \\ \delta G_\xi &\propto (V)^{2/g-2} \end{aligned} \quad (4.64)$$

4.12 Appendix: Expansion of partition function

In this appendix, we expand the partition function of normal reflection in eq.(4.54) up to second order. We assume the perturbation term $v \cos((\tilde{\Phi} - ea)/2)$ is small, and therefore we can Taylor expand this partition function as:

$$\begin{aligned}
Z &= \int \mathcal{D}\tilde{\Phi} \exp \left[- \int \frac{d\omega}{2\pi} \frac{g|\omega|}{2\pi} |\tilde{\Phi}|^2 + \int d\tau v \cos \left(\frac{\tilde{\Phi} - ea}{2} \right) \right] \\
&= Z_0 \left(1 + v \left\langle \int d\tau \cos \left(\frac{\tilde{\Phi} - ea}{2} \right) \right\rangle \right. \\
&\quad \left. + \frac{v^2}{2} \left\langle \left(\int d\tau \cos \left(\frac{\tilde{\Phi} - ea}{2} \right) \right)^2 \right\rangle + \mathcal{O}(v^3) \right) \tag{4.65}
\end{aligned}$$

Here Z_0 is the partition function at normal reflection fixed point without any perturbation.

$$Z_0 = \int \mathcal{D}\tilde{\Phi} \exp \left[- \int \frac{d\omega}{2\pi} \frac{g|\omega|}{2\pi} |\tilde{\Phi}|^2 \right] \tag{4.66}$$

$\langle f(\tilde{\Phi}) \rangle$ is the average of $f(\tilde{\Phi})$ over the partition function.

$$\langle f(\tilde{\Phi}) \rangle = \frac{1}{Z_0} \int \mathcal{D}\tilde{\Phi} \exp \left[- \int \frac{d\omega}{2\pi} \frac{g|\omega|}{2\pi} |\tilde{\Phi}|^2 \right] f(\tilde{\Phi}) \tag{4.67}$$

We can evaluate the first order correction of partition function as following:

$$\begin{aligned}
&\left\langle \cos \left(\frac{\tilde{\Phi} - ea}{2} \right) \right\rangle \\
&= 2 \int d\tau \exp \left[-2 \int_{\Lambda_b}^{\Lambda_a} \frac{d\omega}{2\pi} \frac{\pi}{4g|\omega|} \right] \cos \left[\frac{ea(\tau)}{2} \right] \\
&= \int d\tau \left(\frac{\Lambda_a}{\Lambda_b} \right)^{(-1/4g)} \cos \left[\frac{ea(\tau)}{2} \right] \tag{4.68}
\end{aligned}$$

Here Λ_a and Λ_b are the upper and lower bound of the energy. The upper bound of the energy Λ_a is proportional to temperature $k_B T$, and the lower bound of the energy Λ_b is proportional to inverse of system size, which goes to zero as the system size goes

to infinity. For this reason, the first order correction vanishes ($\left(\frac{\Lambda_a}{\Lambda_b}\right)^{(-1/4g)} \rightarrow 0$) as system is infinitely large.

Now, let's look at the second order term of partition function.

$$\begin{aligned}
& 4 \left\langle \cos \left(\frac{\Phi(\tau_1) - ea(\tau_1)}{2} \right) \cos \left(\frac{\Phi(\tau_2) - ea(\tau_2)}{2} \right) \right\rangle \\
&= \langle e^{\frac{i}{2}(\phi(\tau_1) + \phi(\tau_2))} \rangle e^{\frac{-ie}{2}(a(\tau_1) + a(\tau_2))} + h.c. \\
&\quad + \langle e^{\frac{i}{2}(\phi(\tau_1) - \phi(\tau_2))} \rangle e^{\frac{-ie}{2}(a(\tau_1) - a(\tau_2))} + h.c. \\
&= e^{\frac{-1}{8}\langle(\phi(\tau_1) + \phi(\tau_2))^2\rangle} e^{\frac{-ie}{2}(a(\tau_1) + a(\tau_2))} + h.c. \\
&\quad + e^{\frac{-1}{8}\langle(\phi(\tau_1) - \phi(\tau_2))^2\rangle} e^{\frac{-ie}{2}(a(\tau_1) - a(\tau_2))} + h.c.
\end{aligned} \tag{4.69}$$

We can simplify this correction by the following identities:

$$\langle \phi(\tau_1)^2 \rangle = \int \frac{d\omega}{2\pi} \frac{\pi}{g|\omega|} \tag{4.70}$$

$$\langle \phi(\tau_1)\phi(\tau_2) \rangle = \int \frac{d\omega}{2\pi} \frac{\pi}{g|\omega|} \cos(\omega(\tau_1 - \tau_2)) \tag{4.71}$$

With these two identities in hand, we find that $e^{\frac{-1}{8}\langle(\phi(\tau_1) + \phi(\tau_2))^2\rangle} = e^{-\int \frac{d\omega}{2\pi} \frac{\pi}{4g|\omega|} (1 + \cos(\omega(\tau_1 - \tau_2)))}$.

With the same reason that we use for arguing the vanishing of first order, we find that this term goes to zero as the system becomes infinitely large. Therefore, the second order term remain one nonvanish term, which is

$$e^{\frac{-1}{8}\langle(\phi(\tau_1) - \phi(\tau_2))^2\rangle} = e^{-\int \frac{d\omega}{2\pi} \frac{\pi}{4g|\omega|} (1 - \cos(\omega(\tau_1 - \tau_2)))} \tag{4.72}$$

To get this second order term, we need to evaluate the integration:

$$\int_0^\infty \frac{d\omega}{2\pi} \frac{\pi}{4g\omega} (1 - \cos(\omega(\tau_1 - \tau_2))) \tag{4.73}$$

This integration has logarithmic diverging when $\omega \rightarrow \infty$. We therefore add $e^{-\alpha\omega}$ to the integration as soft upper bound of energy and let $\alpha \rightarrow 0$ after we did the

integration. We therefore get the following integration:

$$\int_0^\infty \frac{d\omega}{2\pi} \frac{\pi}{4g\omega} \{1 - \cos[\omega(\tau_1 - \tau_2)]\} e^{-\alpha\omega} \quad (4.74)$$

To calculate the finite temperature effect, we replace ω with Matsubara frequency $\omega_n = \frac{2n\pi}{\beta}$ and the integration as the sum of Matsubara frequency $\int \frac{d\omega}{2\pi} \rightarrow \frac{1}{\beta} \sum$. At finite temperature the integration now becomes a sum of series. To calculate this series, we notice that the derivative of this series is a geometric series

$$\begin{aligned} I(\tau, \omega) &= \frac{1}{\beta} \sum_n \frac{1}{\omega_n} \{1 - \cos(\omega_n \tau)\} e^{-\alpha\omega_n} \\ \frac{dI(\tau, \omega)}{d\tau} &= \frac{1}{\beta} \sum_n \sin(\omega_n \tau) e^{-\alpha\omega_n} = \frac{1}{2\beta} \cot\left(\frac{\pi\tau}{\beta}\right) \end{aligned} \quad (4.75)$$

Integrate $\frac{dI(\tau, \omega)}{d\tau}$, and we get

$$\begin{aligned} I(\tau, \omega) &= \frac{1}{2\beta} \int_\alpha^\tau d\tau' \cot\left(\frac{\pi\tau'}{\beta}\right) = \frac{1}{2\pi} \ln\left(\frac{\sin(\pi\tau/\beta)}{\sin(\pi\alpha/\beta)}\right) \\ &\approx \frac{1}{2\pi} \ln\left(\frac{\sin(\pi\tau/\beta)}{(\pi\alpha/\beta)}\right) \end{aligned} \quad (4.76)$$

Put together eq.(4.72) and eq.(4.76), and we get the two point correlation function as [89]

$$e^{\frac{-1}{8}\langle(\phi(\tau_1) - \phi(\tau_2))^2\rangle} = \left(\frac{\pi\alpha/\beta}{\sin(\pi(\tau_1 - \tau_2)/\beta)}\right)^{\frac{1}{4g}} \quad (4.77)$$

With the vanishing of the first order and the second order correction that we got from eq.(4.77), we can write the partition function in eq.(4.65) as

$$\begin{aligned} Z &= Z_0 \left(1 + \frac{v^2}{2} \left(\frac{\pi\alpha/\beta}{\sin(\pi(\tau_1 - \tau_2)/\beta)}\right)^{\frac{1}{4g}} \cos\left(\frac{e}{2}(a(\tau_1) - a(\tau_2))\right)\right) \\ &\quad + \mathcal{O}(v^3) \end{aligned} \quad (4.78)$$

4.13 Appendix:Duality for $\cos 4\theta$

We begin with the partition function at the Andreev reflection fixed point perturbed by $\cos 4\Theta$ with $g < 1/8$,

$$Z = \int \mathcal{D}\Theta e^{-S_A[\Theta] - 2\lambda \int d\tau \cos 4\Theta}. \quad (4.79)$$

where we take λ to be very large and positive. We first use the Villain approximation,

$$e^{-2\lambda \cos 4\Theta} \rightarrow e^{-2\lambda \sum_{n \in \mathbb{Z}} e^{\lambda(4\Theta - 2\pi n)^2}} \quad (4.80)$$

and then a hubbard Strotonovitch field ρ to decouple the quadratic term,

$$\int \mathcal{D}\rho e^{-\int d\tau (\rho^2/\lambda + 2i\rho(4\Theta - 2\pi n(\tau)))} = \quad (4.81)$$

$$= e^{\lambda(4\Theta - 2\pi n(\tau))^2}. \quad (4.82)$$

Putting these together we find,

$$Z = \int \mathcal{D}\Theta \mathcal{D}\rho \sum_{n(\tau) \in \mathbb{Z}} e^{-S_A[\Theta] - \int d\tau (\rho^2/\lambda + 2i\rho(4\Theta - 2\pi n(\tau)))}. \quad (4.83)$$

Now we write $\rho = \partial_\tau \Phi / (2\pi)$, with Φ/π conjugate to Θ , and substitute it into the partition function. This results in,

$$Z = \int \mathcal{D}\Theta \mathcal{D}\Phi \sum_{n(\tau) \in \mathbb{Z}} e^{-S_A[\Theta] - \int d\tau \left(\frac{1}{\lambda} \left(\frac{\partial_\tau \Phi}{2\pi} \right)^2 + i \frac{\partial_\tau \Phi}{\pi} (4\Theta - 2\pi n(\tau)) \right)}. \quad (4.84)$$

The sum over $n(\tau)$ enforces a delta function on $\partial_\tau \Phi$ restricted to zero, i.e., $\delta(\partial_\tau \Phi)$. Thus we find that Φ is a constant modulo π (since the solution must be invariant under $\partial_\tau \Phi \rightarrow \partial_\tau \Phi + \pi$ means that $\Phi(\tau + \delta\tau) - \Phi(\tau) \in \pi\mathbb{Z}$). We enforce this constraint ‘softly’ by adding a term to the action $-v \cos 2\Phi$ with v large. We then integrate out

Θ and find an action solely in terms of Φ . This results in,

$$Z = \int \mathcal{D}\Phi e^{-\int \frac{d\omega}{2\pi} \frac{16|\omega|g}{2\pi} \Phi_\omega \Phi_{-\omega} - \int d\tau \left(\frac{1}{\lambda} \left(\frac{\partial_\tau \Phi}{2\pi} \right)^2 - v \cos 2\Phi \right)} \quad (4.85)$$

The $(\partial_\tau \Phi)^2$ term is irrelevant compared to $|\omega||\Phi|^2$ so we throw it away. We then re-scale the field $\Phi_\omega \rightarrow \Phi_\omega/4$ so that the action takes on the original form of the normal reflection fixed point. This yields,

$$Z_{dual} = \int \mathcal{D}\Phi e^{-S_N[\Phi] - \int d\tau v \cos \Phi/2} \quad (4.86)$$

as stated in the main text.

Chapter 5

Electrical manipulation of Majorana fermions in an interdigitated superconductor-ferromagnet device

Topological superconductors have attracted considerable recent interest because they may provide the first unambiguous realization of Majorana fermions in any physical setting. The pursuit of these elusive objects in condensed matter [101, 102] is motivated largely by the non-Abelian statistics [103, 104, 105] that they underpin, which is widely sought for quantum computation [106]. Although much attention recently has focused on finding Majorana fermions in 1D systems [77, 107, 108, 109, 110, 36], 2D platforms [103, 111, 112, 113, 114, 115, 116] offer some unique virtues such as the ability to perform interferometry [117, 118, 119, 120, 121, 122, 123] to probe non-Abelian statistics. One promising 2D scheme involves a quantum well sandwiched between an *s*-wave superconductor and a magnetic insulator [113]. Fabricating this device is, however, rather nontrivial as one must synthesize high quality interfaces on both sides of the quantum well—which is typically buried in a heterostructure. One can avoid a multilayered architecture by invoking a specific type of 2D electron gas (2DEG) with appreciable Rashba and Dresselhaus coupling, but the candidate materials for this proposal are limited.

In this chapter, we introduce a new 2D Majorana platform (Fig. 5.1) consisting of interdigitated superconductor/ferromagnet insulator strips deposited on a 2DEG (pe-

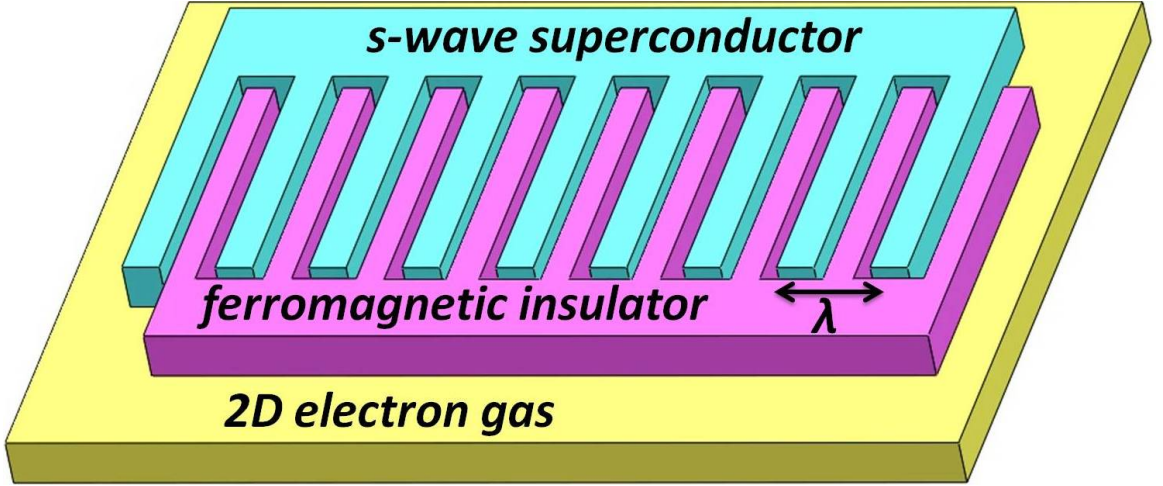


Figure 5.1: Schematic of the proposed interdigitated superconductor-ferromagnet 2DEG architecture. The device supports a robust topological phase when the finger spacing λ is smaller than half of the Fermi wavelength (*i.e.* $\lambda < \lambda_F/2$). A topological phase can also appear in the regime $\lambda > \lambda_F/2$, though generally with a suppressed gap. Table I provides values of λ_F for select 2DEGs when the chemical potential is set to $\mu = 0$.

riodically modulated 1D topological superconductors were considered in Ref. [124]). The proposed setup exhibits several virtues. For one, our device requires interface engineering on only one side of the 2DEG—alleviating one experimental challenge with previous semiconductor-based proposals. Because of this feature one can also employ a wider variety of 2DEGs, including surface states of bulk semiconductors such as InAs [125, 126, 127]. Meanwhile, this structure naturally allows one to *electrically* generate vortices to trap Majorana zero-modes, potentially allowing Majorana fermions to be braided using currents similar to the proposal of Ref. [128]. We further show that in our device (as well as any 2D topological superconductor) Majorana edge states can be detected by observing an anomalous shift of the zeros in the Fraunhofer pattern measured in a long Josephson junction.

We model the semiconductor in this device with the following Hamiltonian,

$$\begin{aligned}
 H = & \int d^2\mathbf{r} \left\{ \psi^\dagger \left[-\frac{\hbar^2 \nabla^2}{2m} - \mu - i\alpha(\sigma^x \partial_y - \sigma^y \partial_x) \right] \psi \right. \\
 & \left. + V_z(\mathbf{r}) \psi^\dagger \sigma^z \psi + [\Delta(\mathbf{r}) \psi_\uparrow \psi_\downarrow + \text{H.c.}] \right\}, \tag{5.1}
 \end{aligned}$$

2DEG	α [eVÅ]	m/m_e	λ_F [μm]
InGaAs/InAlAs	0.05	0.04	1.19
InSb/InAlSb	0.14	0.0139	1.22
Bulk InAs surface	0.11	0.03	0.72

Table 5.1: Effective mass m in units of the electron mass m_e , Rashba coupling strength α , and Fermi wavelength λ_F evaluated at $\mu = 0$ for the 2DEG's listed in the left column.

where ψ_σ^\dagger creates an electron with spin σ and effective mass m , μ is the chemical potential, α is the Rashba coupling strength, and σ^a are Pauli matrices that contract with the spin indices. The spatially varying Zeeman and pairing fields induced by the alternating ferromagnetic and superconducting strips are respectively denoted by $V_z(\mathbf{r})$ and $\Delta(\mathbf{r})$. For simplicity we will retain only their maximal Fourier components and take $V_z(\mathbf{r}) = 2\bar{V}_z \sin^2(\frac{1}{2}Qx)$ and $\Delta(\mathbf{r}) = 2\bar{\Delta} \cos^2(\frac{1}{2}Qx)$. Here \bar{V}_z and $\bar{\Delta}$ are the spatial average of these quantities, which modulate at wavevector $Q = 2\pi/\lambda$ with λ the finger spacing shown in Fig. 5.1. This choice is expected to not only quantitatively capture the effects of interdigitation, but as we will see also leads to an intuitive physical picture for the device's behavior.

As a primer it is worth recalling the physics of the sandwich structure originally proposed by Sau *et al.* [113], where a uniform Zeeman field V_z^{unif} opens a chemical potential window in which only one Fermi surface is present. Incorporating s -wave pairing with strength Δ^{unif} in this regime effectively drives the 2DEG into a topological $p + ip$ superconductor due to the interplay with spin-orbit coupling. [112, 113, 115, 102, 129] Quantitatively, the topological phase appears provided $(V_z^{\text{unif}})^2 > (\Delta^{\text{unif}})^2 + \mu^2$. In our interdigitated setup it is natural to expect that when the Fermi wavelength λ_F for the semiconductor greatly exceeds the finger spacing λ , electrons in the 2DEG effectively experience 'smeared' Zeeman and pairing fields with strength \bar{V}_z and $\bar{\Delta}$. Similar physics to the uniform case ought to then emerge—in particular, a topological phase when $\bar{V}_z^2 \gtrsim \bar{\Delta}^2 + \mu^2$.

To confirm this intuition and extract the phase diagram for arbitrary λ_F/λ , we study the quasiparticle spectrum for Eq. (5.1). Defining a Nambu spinor $\Psi_{\mathbf{k}} = [\psi_\uparrow(\mathbf{k}), \psi_\downarrow(\mathbf{k}), \psi_\downarrow^\dagger(-\mathbf{k}), -\psi_\uparrow^\dagger(-\mathbf{k})]^T$, the Hamiltonian can be written in momentum

space as

$$H = \int \frac{d^2\mathbf{k}}{(2\pi)^2} (\overline{\mathcal{H}}_{\mathbf{k}} + \delta\mathcal{H}_{\mathbf{k}}) \quad (5.2)$$

$$\begin{aligned} \overline{\mathcal{H}}_{\mathbf{k}} = & \Psi_{\mathbf{k}}^\dagger \left[\left(\frac{\hbar^2 k^2}{2m} - \mu \right) \tau^z + \alpha (k_y \sigma^x - k_x \sigma^y) \tau^z \right. \\ & \left. + \overline{V}_z \sigma^z + \overline{\Delta} \tau^x \right] \Psi_{\mathbf{k}} \end{aligned} \quad (5.3)$$

$$\delta\mathcal{H}_{\mathbf{k}} = \Psi_{\mathbf{k}}^\dagger \left[-\frac{\overline{V}_z}{2} \sigma^z + \frac{\overline{\Delta}}{2} \tau^x \right] \Psi_{\mathbf{k}+Q\hat{\mathbf{x}}} + \text{H.c.} \quad (5.4)$$

with τ^a Pauli matrices that act in particle-hole space. The Hamiltonian $\overline{\mathcal{H}}_{\mathbf{k}}$ describes a semiconductor proximate to a uniform superconductor and ferromagnet and is precisely the model studied in Ref. [113]. The bulk excitation spectrum obtained from $\overline{\mathcal{H}}_{\mathbf{k}}$ in the topological phase with $\mu = 0$, $\overline{V}_z = 1.5\overline{\Delta}$, $m\alpha^2 = 3\overline{\Delta}$ and $k_y = 0$ appears in the red dashed lines of Fig. 5.2; roughly, the gap at $k_x = 0$ is set by \overline{V}_z while $\overline{\Delta}$ determines the gap at the Fermi wavevector $k_F = 2\pi/\lambda_F$. Our interdigitated structure produces a new term $\delta\mathcal{H}_{\mathbf{k}}$ that couples spinors with wavevectors \mathbf{k} and $\mathbf{k} \pm Q\hat{\mathbf{x}}$. As we ‘turn on’ these couplings the spectrum of $\overline{\mathcal{H}}_{\mathbf{k}}$ evolves very similarly to the band structure of free electrons in a weak periodic potential [130]. In particular, the dominant effect of $\delta\mathcal{H}_{\mathbf{k}}$ is to open a gap in the excitation spectrum whenever the energies cross Bragg planes at $k_x = \pm Q/2 = \pm\pi/\lambda$ (modulo reciprocal lattice vectors). For momenta away from these values $\delta\mathcal{H}_{\mathbf{k}}$ couples states that are far from resonant and hence perturbs these only weakly.

It follows that for $\lambda_F/\lambda \gg 1$ the periodic modulation modifies the quasiparticle spectrum appreciably only at very high energies. This point is illustrated by the solid curves in Fig. 5.2, which display the numerically obtained spectrum for the full Hamiltonian in Eq. (5.2) in a repeated zone scheme, using the same parameters as above but now with $\lambda_F/\lambda = 2.6$. Even for this ratio of λ_F/λ , the spectrum is nearly identical to that of the uniform case away from $k_x = \pm\pi/\lambda$. When $\lambda_F/\lambda \gg 1$ one can clearly incorporate $\delta\mathcal{H}_{\mathbf{k}}$ while essentially leaving the bulk excitation gap exhibited by the uniform system intact. Thus by adiabatic continuity our interdigitated device

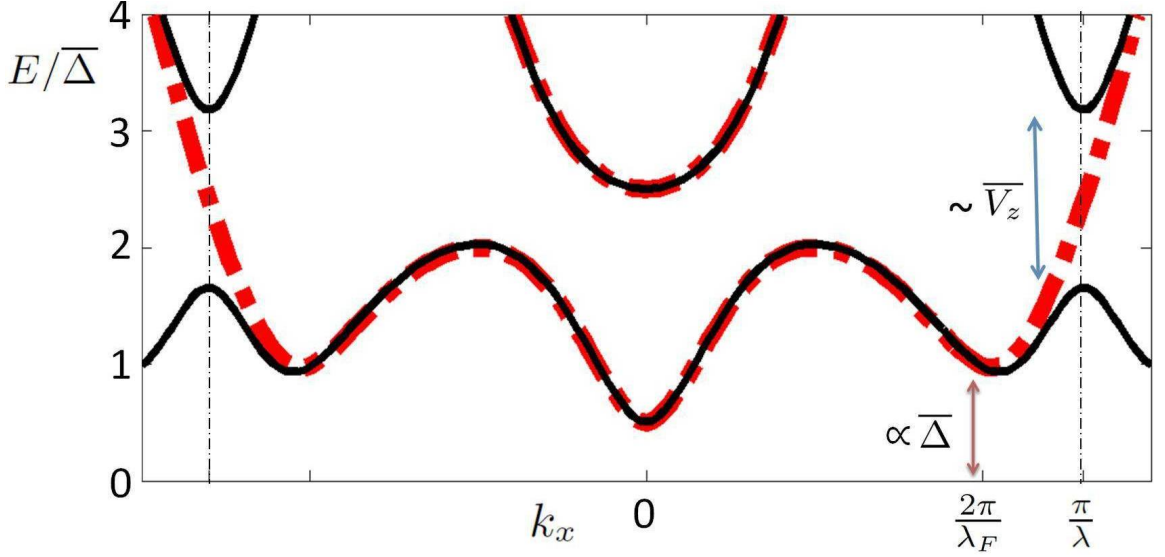


Figure 5.2: Bulk quasiparticle spectrum versus k_x in a uniform structure (dashed curve) and interdigitated device with $\lambda_F/\lambda = 2.6$ (solid curve). In both cases we use parameters $k_y = 0$, $\mu = 0$, $\bar{V}_z = 1.5\bar{\Delta}$, and $m\alpha^2 = 3\bar{\Delta}$. The red arrow indicates the pairing gap at the Fermi momentum $k_F \equiv \frac{2\pi}{\lambda_F} \approx 2m\alpha/\hbar^2$, while the blue arrow denotes the degeneracy gap opened at $k_x = \frac{\pi}{\lambda}$ due to the interdigitation. Note that the excitation spectra for the uniform and interdigitated systems differ appreciably only at rather higher energies here.

supports a topological phase in this limit provided $\bar{V}_z^2 \gtrsim \bar{\Delta}^2 + \mu^2$, consistent with the intuition provided earlier. As further evidence, Figs. 5.3(a) and (b) display the quasiparticle spectrum as a function of k_y in a system with open boundary conditions along the x direction. The data correspond to $\mu = 0$, $m\alpha^2 = 3\bar{\Delta}$ and $\lambda_F/\lambda = 2.5$, while the Zeeman energy changes from $\bar{V}_z = 0.5\bar{\Delta}$ in (a) to $\bar{V}_z = 2\bar{\Delta}$ in (b). In (a) a trivial gapped state clearly emerges due to the weak Zeeman energy. The larger \bar{V}_z value in (b), however, satisfies our topological criterion, and one indeed sees the signature gapless chiral Majorana edge states inside of the bulk gap.

As one reduces the ratio λ_F/λ to a value of order one or smaller, the physics becomes considerably more subtle. Indeed, once $\lambda_F/\lambda \approx 2$ the Bragg plane at $k_x = Q/2$ approaches the Fermi wavevector, and the pairing gap can then be dramatically altered by the interdigitation. We ascertain the global phase diagram of our device by numerically computing the minimum excitation gap δ for a system on a torus as a function of λ_F/λ and $\bar{V}_z/\bar{\Delta}$. Figure 5.4 shows the results for $\mu = 0$ and spin-

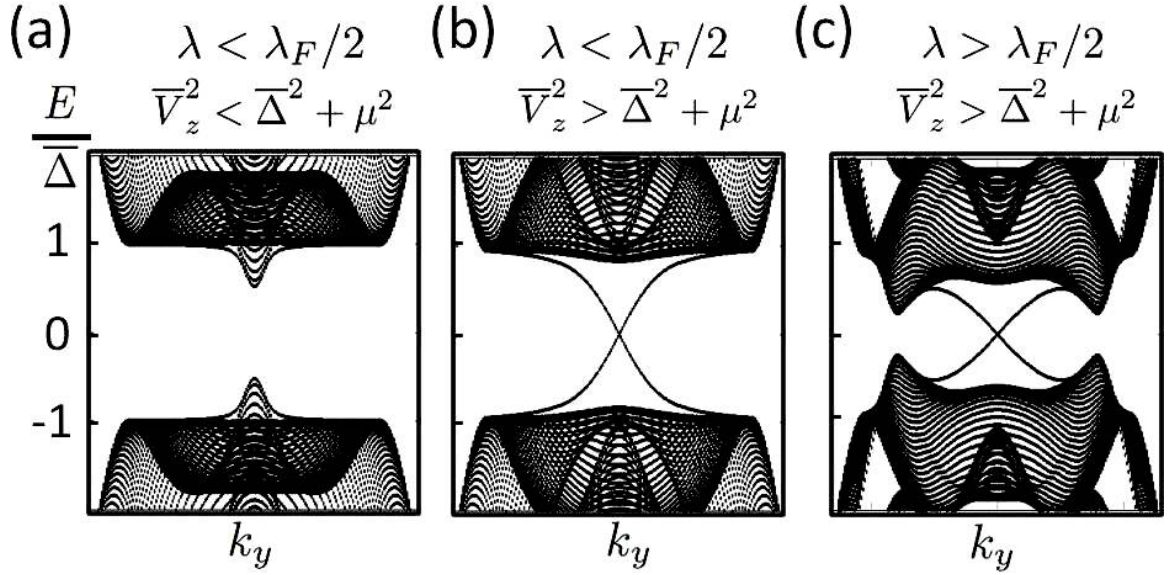


Figure 5.3: Quasiparticle spectrum in various regimes for an interdigitated device with periodic boundary conditions along y but open boundary conditions along x . In all parts we take $\mu = 0$ and $m\alpha^2 = 3\bar{\Delta}$, while the finger spacing and Zeeman energy vary as (a) $\lambda_F/\lambda = 2.5$, $\bar{V}_z = 0.5\bar{\Delta}$, (b) $\lambda_F/\lambda = 2.5$, $\bar{V}_z = 2\bar{\Delta}$, and (c) $\lambda_F/\lambda = 1.5$, $\bar{V}_z = 2\bar{\Delta}$. A trivial state appears in (a) while the larger Zeeman field in (b) drives a topological phase supporting chiral Majorana edge states within the bulk gap. Interestingly, the topological phase and associated Majorana edge states survive even in (c) despite the relatively small ratio of λ_F/λ .

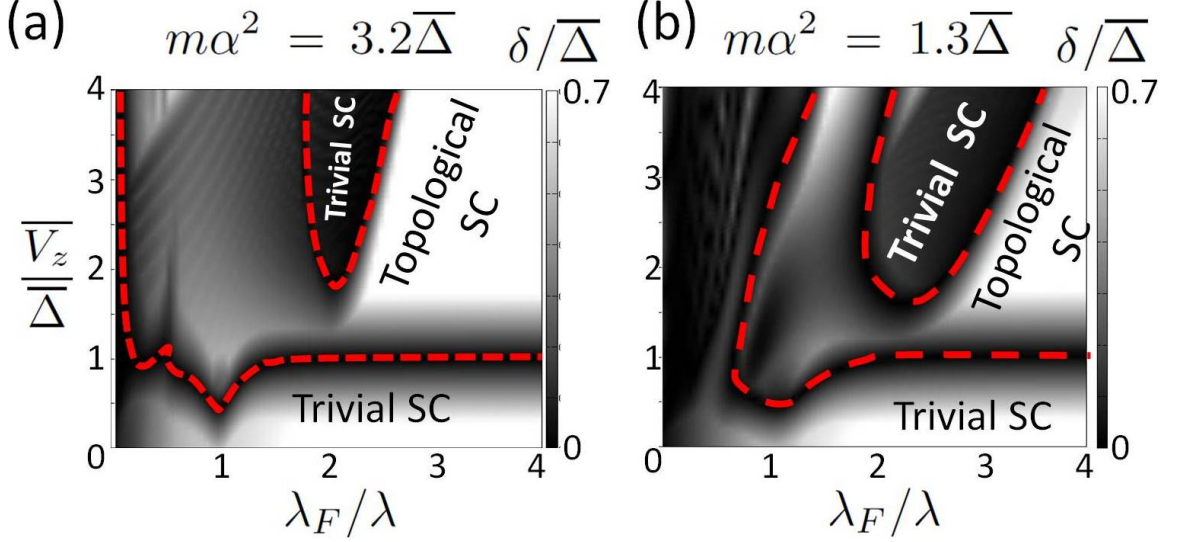


Figure 5.4: Phase diagrams for $\mu = 0$ and spin-orbit energies (a) $m\alpha^2 = 3.2\bar{\Delta}$ and (b) $m\alpha^2 = 1.3\bar{\Delta}$. The horizontal axis represents ratio of the Fermi wavelength λ_F to the finger spacing λ , while the vertical axis is the Zeeman energy normalized by pairing strength. The shading indicates the bulk gap δ normalized by $\bar{\Delta}$. Red dashed lines denote the boundary between topological phase and trivial phases.

orbit energies of $m\alpha^2 = 3.2\bar{\Delta}$ in (a) and $m\alpha^2 = 1.3\bar{\Delta}$ in (b). The following points are noteworthy here: 1) At ‘large’ λ_F/λ topological superconductivity appears when $\bar{V}_z \gtrsim \bar{\Delta}$, in line with our results above. 2) The topological phase survives over a range of parameters even for rather small values of λ_F/λ , though the gap is generally reduced compared to the large λ_F/λ limit. Figure 5.3(c) illustrates the spectrum in the $\lambda_F/\lambda < 2$ regime for a system with open boundary conditions along x ; just as in Fig. 5.3(b) the characteristic chiral edge states again appear here. 3) Interestingly, for $\lambda_F/\lambda \sim 1$ the critical value of \bar{V}_z required to generate the topological phase *decreases* compared to the uniform case.

Having numerically demonstrated that our device exhibits a topological phase with an edge state, we now describe how the interdigitated structure naturally allows us to *electrically* generate vortices to trap Majorana zero-modes. Consider the setup of Fig. 5.5. Supercurrent flowing from contact 1 to contact 2 produces a winding in the superconducting phase $\theta(\mathbf{r})$ across the fingers in the device. When the phase difference between the contacts approaches 2π , a vortex forms near the center of the system to minimize the energy $E \propto \int d^2\mathbf{r}(\nabla\theta)^2$. The spatial profile of the phase follows from

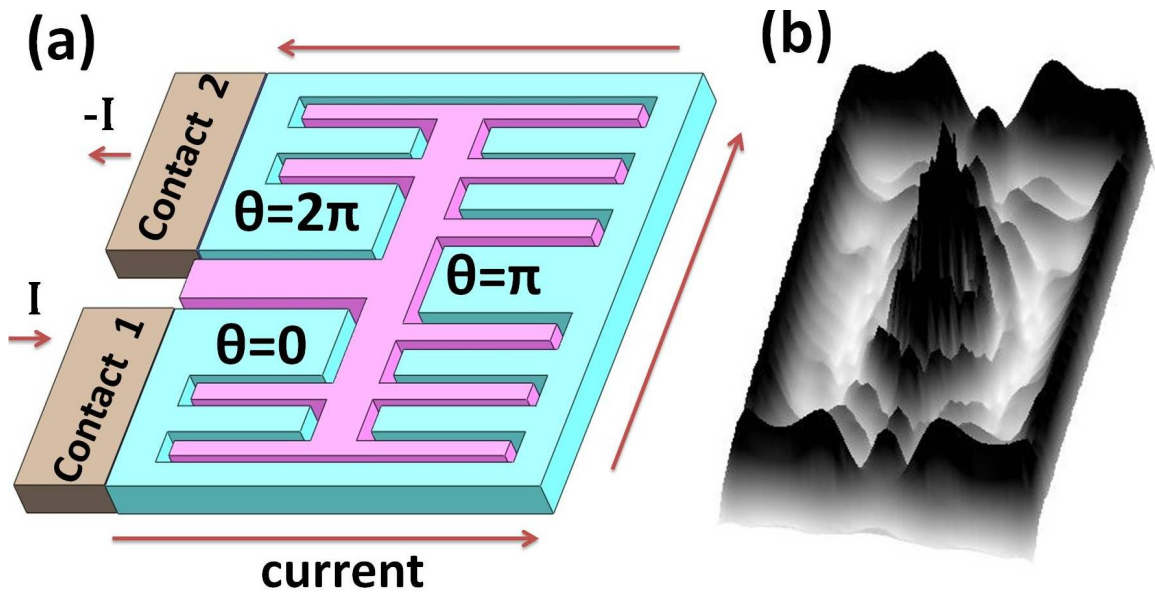


Figure 5.5: (a) Scheme to electrically stabilize a vortex binding a Majorana zero-mode. Here the singular phase winding is induced by current flowing from contact 1 to contact 2, rather than from a magnetic field. In (b) we illustrate the probability density extracted from the near-zero energy mode generated by a current-induced vortex at the center of the device (parameters are $\mu = 0$, $m\alpha^2 = 1.3\bar{\Delta}$, $\bar{V}_z = 2\bar{\Delta}$, and $\lambda = \lambda_F/4$). The large central peak corresponds to the Majorana bound to the vortex, which hybridizes weakly with the outer Majorana running along the perimeter.

the supercurrent $\mathbf{j}(\mathbf{r}) \propto \Delta^*(\mathbf{r})\nabla\Delta(\mathbf{r}) - \Delta(\mathbf{r})\nabla\Delta^*(\mathbf{r})$, with $\Delta(\mathbf{r}) = \Delta_{SC}(\mathbf{r})e^{i\theta(\mathbf{r})}$, where the pairing potential's magnitude satisfies $\Delta_{SC}(\mathbf{r}) = 2\bar{\Delta}$ beneath the superconductors [blue regions in Fig. 5.5(a)] and goes to zero under the ferromagnets [pink regions in Fig. 5.5(a)]. In particular, one can extract $\theta(\mathbf{r})$ by iterating the current conservation equation $\nabla \cdot \mathbf{j}(\mathbf{r}) = 0$ subject to boundary conditions along the system's perimeter. With this phase in hand, one can diagonalize the Hamiltonian in the presence of a current-induced vortex and extract the wavefunctions for each quasiparticle state. Figure 5.5(b) illustrates the resulting probability distribution for the near-zero-energy state in the spectrum; the large central peak corresponds to a localized Majorana mode bound to the vortex core, while the outer peak represents a second Majorana mode running along the edge.

Finally, we discuss the detection of Majorana edge states in the topological phase exhibited by our device (or, equivalently, any other realization) via an unconventional Fraunhofer pattern.¹ Consider a pair of topological superconductors forming a long Josephson junction of width w pierced by a magnetic field [see Fig. 5.6(a)]. At low energies it suffices to focus only on the chiral edge states, which can be modeled by an effective Hamiltonian $H = H_t + H_b + H_{\text{tunneling}}$. [103, 131, 123] The first two terms $H_{t/b} = \pm i v \hbar \int dx \gamma_{t/b} \partial_x \gamma_{t/b}$ describe the kinetic energy for the top/bottom edge states, with $\gamma_{t/b}$ Majorana operators and v the edge velocity. The last term incorporates inter-edge tunneling with strength t at the interface and reads $H_{\text{tunneling}} = it \int_{-w/2}^{w/2} dx \gamma_t \gamma_b \cos[\theta(x)/2]$, where $\theta(x)$ is the local superconducting phase difference across the junction induced by the applied field. Neglecting the magnetic field that is produced from the tunneling current, $\theta(x)$ is determined by the external magnetic flux Φ according to $\theta(x) = \theta_0 + 2\pi \frac{\Phi}{\Phi_0} \frac{x}{w}$ (Φ_0 is the flux quantum and θ_0 is the phase difference at the junction's center).

The Majorana-mediated contribution to the local current density flowing across the junction follows from $j(x) = \frac{et}{\hbar} \sin[\theta(x)/2] i \gamma_t \gamma_b$. We calculate the current perturbatively in t assuming the weak-tunneling limit $\frac{tw}{2\pi\hbar v} < 1$ where the hybridization energy is smaller than the level spacing. In this case the physics depends sharply on

¹This idea has been independently proposed by Julia Meyer and Manuel Houzet.

whether, at $t = 0$, Majorana zero-modes exist at each edge. If neither edge supports a zero-mode, then the current vanishes to first order in t . However, if zero-modes exist at both edges (due to an odd number of vortices in their bulk) then a finite current $\langle j(x) \rangle = \frac{et}{\hbar L} \sin[\theta(x)/2]$ emerges, where L is the superconductors' perimeter. Integrating over the junction width yields a total Majorana-mediated current

$$I_M = \frac{twe}{\hbar L} \sin\left(\frac{\theta_0}{2}\right) \left[\frac{\sin\left(\frac{\pi}{2} \frac{\Phi}{\Phi_0}\right)}{\frac{\pi}{2} \frac{\Phi}{\Phi_0}} \right]. \quad (5.5)$$

The solid black curve in Fig. 5.6(b) illustrates $|I_M|$ as a function of Φ ; remarkably, the zeros occur at *even* multiples of Φ/Φ_0 in contrast to the conventional Fraunhofer pattern shown for comparison in the red dashed curve. For a sample of size $5\mu\text{m} \times 5\mu\text{m}$ with the coupling energy $t = 0.025\text{meV}$ [123], we estimate that the typical magnitude of I_M is $\sim 1.5\text{nA}$. This result is valid when the edge velocity obeys $v > 3 \times 10^4\text{m/s}$ so that the weak tunneling limit is satisfied. It is important to keep in mind, however, that the experimentally observed current will not be given by I_M alone—a potentially much larger conventional current I_s flows in parallel. The magnitude of the total current $I_{\text{tot}} = I_s + I_M$ is sketched by the blue curve in Fig. 5.6(b). One can infer the existence of I_M by the unconventional Fraunhofer pattern that exhibits shifted zeros as shown in the figure. We note that very recently an experiment of this type has been performed in a long Josephson junction formed at the surface of a 3D topological insulator [132], though the findings are rather different from what we predict here.

In conclusion, we have shown that our interdigitated structure exhibits a topological phase that is particularly robust when the finger spacing is smaller than half of the Fermi wavelength. There the bulk gap can be comparable to that in a uniform system; furthermore, additional perturbations induced by the interdigitation (such as variations in chemical potential and Rashba strength) should play a minor role. To access this regime the finger spacing should be $\lesssim 600\text{nm}$ for the quantum wells listed in Table I and $\lesssim 400\text{nm}$ for the surface state of bulk InAs. We also note that since electrons effectively see ‘smeared’ fields in this limit, the specific interdigitated pattern studied here is by no means required—similar physics should arise, *e.g.*, in

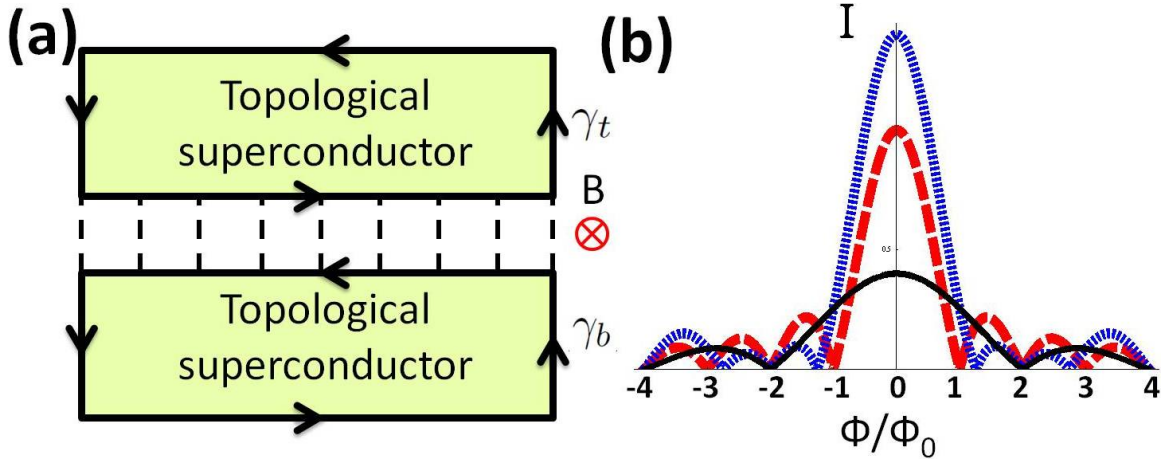


Figure 5.6: (a) Long Josephson junction formed by adjacent topological superconductors. A magnetic field \vec{B} orients perpendicular to the plane and uniformly penetrates through the junction. (b) The solid black curve represents the magnitude of the tunneling current arising from coupled Majorana zero-modes at the edge. This contribution exhibits zeros at even multiples of the flux quantum in sharp contrast to the Fraunhofer pattern exhibited by ordinary s -wave superconductor junctions (red dashed curve). The blue curve represents the anomalous Fraunhofer pattern that would arise in an experiment due to the Majorana-mediated component and a parallel conventional current contribution.

checkerboard arrangements. An interesting feature of our setup is that vortices can be generated by applying currents. This mechanism may eventually provide a practical means of manipulating and braiding vortices for quantum computation. We also pointed out that chiral Majorana edge states produce an anomalous Fraunhofer pattern that can be observed in any realization of topological $p + ip$ superconductivity.

Chapter 6

Future direction

In summary, we show that topological superconductivity provides a promising platform for exotic excitations such as Majorana zero modes and parafermions. The underlying nonabelian exchange statistic gives a pathway toward topological quantum information. Here I am going to show another special property of topological superconductivity—the ability of teleporting electrons. This proposal was proposed by Liang Fu [133]. He suggested that electrons can nonlocally transfer through Majorana bound states. To be more precisely, an electron which is injected into one Majorana bound state can go out from another Majorana bound state that is far apart as long as the superconducting phase remains coherent. In the following discussion, we use the Majorana zero modes that are induced in a 2D topological insulator as an example to illustrate this idea. Fig.6.1(a) shows the topological superconductivity that is induced on edge states by coupling these states to a superconductor. Majorana zero modes appear at the end of the topological superconducting region as one breaks time reversal symmetry by inducing Zeeman splitting. These two Majorana modes form a single fermionic states. One can assume the initial state of this single fermionic state is an empty state. As one injects an electron into one of the Majorana mode, the single fermionic states goes from the empty state to the occupied state. The electron can hop out through another Majorana mode which gives the teleport of the electron.

One can generalize Liang’s proposal to the interacting case. As shown in Fig.6.1(b), strong repulsive interactions causes spontaneously time reversal symmetry breaking on edge states. This mechanism arises Z_4 parafermions as proximity effect is induced

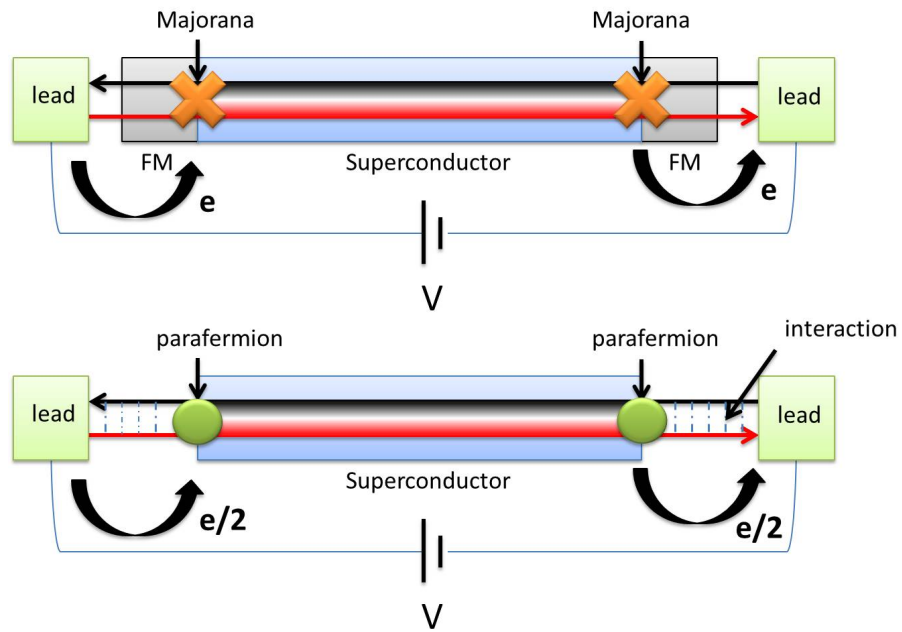


Figure 6.1: (a) Electrons teleport through Majorana bound states. (b) Fractional charge teleport through parafermion modes.

on the edge states. One can think a Z_4 parafermion as a half Majorana fermion. Therefore, the Z_4 parafermions may allow $e/2$ fractional charge to teleport across the superconducting region.

Bibliography

- [1] V. Mourik, K. Zuo, S. M. Frolov, S. R. Plissard, E. P. A. M. Bakkers, and L. P. Kouwenhoven, “Signatures of majorana fermions in hybrid superconductor-semiconductor nanowire devices,” *Science*, vol. 336, no. 6084, pp. 1003–1007, 2012.
- [2] H. Ren, S. Hart, T. Wagner, P. Leubner, M. Muehlbauer, C. Bruene, H. Buhmann, L. Molenkamp, and A. Yacoby, “Induced superconductivity in the quantum spin hall edge,” *Nature Physics*, vol. 10, pp. 638–643, 2014.
- [3] S. Nadj-Perge, I. K. Drozdov, B. A. Bernevig, and A. Yazdani, “Proposal for realizing Majorana fermions in chains of magnetic atoms on a superconductor,” *Phys. Rev. B*, vol. 88, p. 020407, Jul 2013.
- [4] L. Fu and C. L. Kane, “Josephson current and noise at a superconductor/quantum-spin-hall-insulator/superconductor junction,” *Phys. Rev. B*, vol. 79, p. 161408, Apr 2009.
- [5] J. D. Sau, R. M. Lutchyn, S. Tewari, and S. Das Sarma, “Generic new platform for topological quantum computation using semiconductor heterostructures,” *Phys. Rev. Lett.*, vol. 104, p. 040502, Jan 2010.
- [6] Y. Oreg, G. Refael, and F. von Oppen, “Helical liquids and majorana bound states in quantum wires,” *Phys. Rev. Lett.*, vol. 105, p. 177002, Oct 2010.
- [7] R. M. Lutchyn, J. D. Sau, and S. Das Sarma, “Majorana fermions and a topological phase transition in semiconductor-superconductor heterostructures,” *Phys. Rev. Lett.*, vol. 105, p. 077001, Aug 2010.

- [8] S.-P. Lee, K. Michaeli, J. Alicea, and A. Yacoby, “Revealing topological superconductivity in extended quantum spin hall josephson junctions,” *Phys. Rev. Lett.*, vol. 113, p. 197001, Nov 2014.
- [9] V. S. Pribiag, A. J. Beukman, F. Qu, M. C. Cassidy, C. Charpentier, W. Wegscheider, and L. P. Kouwenhoven, “Edge-mode superconductivity in a two dimensional topological insulator,” *arXiv preprint arXiv:1408.1701*, 2014.
- [10] S.-P. Lee, J. Alicea, and G. Refael, “Electrical manipulation of majorana fermions in an interdigitated superconductor-ferromagnet device,” in preparation.
- [11] A. Y. Kitaev, “Unpaired Majorana fermions in quantum wires,” *Sov. Phys.–Uspeki*, vol. 44, p. 131, Oct. 2001.
- [12] C. W. J. Beenakker, “Search for Majorana fermions in superconductors,” *Annu. Rev. Con. Mat. Phys.*, vol. 4, pp. 113–136, 2013.
- [13] J. Alicea, “New directions in the pursuit of Majorana fermions in solid state systems,” *Rep. Prog. Phys.*, vol. 75, p. 076501, 2012.
- [14] M. Leijnse and K. Flensberg, “Introduction to topological superconductivity and majorana fermions,” *Semiconductor Science and Technology*, vol. 27, no. 12, p. 124003, 2012.
- [15] T. D. Stanescu and S. Tewari, “Majorana fermions in semiconductor nanowires: fundamentals, modeling, and experiment,” *Journal of Physics: Condensed Matter*, vol. 25, no. 23, p. 233201, 2013.
- [16] C. Nayak, S. H. Simon, A. Stern, M. Freedman, and S. Das Sarma, “Non-Abelian anyons and topological quantum computation,” *Rev. Mod. Phys.*, vol. 80, pp. 1083–1159, Sep 2008.
- [17] J. Alicea, “New directions in the pursuit of majorana fermions in solid state systems,” *Reports on Progress in Physics*, vol. 75, no. 7, p. 076501, 2012.

- [18] J. Alicea and A. Stern, “Designer non-abelian anyon platforms: from majorana to fibonacci,” *arXiv preprint arXiv:1410.0359*, 2014.
- [19] L. Fu and C. L. Kane, “Josephson current and noise at a superconductor/quantum-spin-Hall-insulator/superconductor junction,” *Phys. Rev. B*, vol. 79, p. 161408(R), 2009.
- [20] A. M. Black-Schaffer and J. Linder, “Magnetization dynamics and majorana fermions in ferromagnetic josephson junctions along the quantum spin hall edge,” *Phys. Rev. B*, vol. 83, p. 220511, Jun 2011.
- [21] D. M. Badiane, M. Houzet, and J. S. Meyer, “Nonequilibrium josephson effect through helical edge states,” *Phys. Rev. Lett.*, vol. 107, p. 177002, Oct 2011.
- [22] L. Jiang, D. Pekker, J. Alicea, G. Refael, Y. Oreg, and F. von Oppen, “Unconventional josephson signatures of majorana bound states,” *Phys. Rev. Lett.*, vol. 107, p. 236401, Nov 2011.
- [23] Q. Meng, V. Shivamoggi, T. L. Hughes, M. J. Gilbert, and S. Vishveshwara, “Fractional spin Josephson effect and electrically controlled magnetization in quantum spin Hall edges,” *Phys. Rev. B*, vol. 86, p. 165110, Oct 2012.
- [24] L. Jiang, D. Pekker, J. Alicea, G. Refael, Y. Oreg, A. Brataas, and F. von Oppen, “Magneto-Josephson effects in junctions with Majorana bound states,” *Phys. Rev. B*, vol. 87, p. 075438, Feb 2013.
- [25] M. Houzet, J. S. Meyer, D. M. Badiane, and L. I. Glazman, “Dynamics of majorana states in a topological josephson junction,” *Phys. Rev. Lett.*, vol. 111, p. 046401, Jul 2013.
- [26] C. W. J. Beenakker, D. I. Pikulin, T. Hyart, H. Schomerus, and J. P. Dahlhaus, “Fermion-parity anomaly of the critical supercurrent in the quantum spin-hall effect,” *Phys. Rev. Lett.*, vol. 110, p. 017003, Jan 2013.

- [27] S. Barbarino, R. Fazio, M. Sasseti, and F. Taddei, “Parity dependent josephson current through a helical luttinger liquid,” *New J. Phys.*, vol. 15, p. 085025, 2013.
- [28] S.-F. Zhang, W. Zhu, and Q.-F. Sun, “Josephson junction on one edge of a two dimensional topological insulator affected by magnetic impurity,” *Journal of Physics: Condensed Matter*, vol. 25, p. 295301, 2013.
- [29] F. Crepin and B. Trauzettel, “Parity measurement in topological josephson junctions,” *arXiv:1305.7433*, unpublished.
- [30] D. M. Badiane, L. I. Glazman, M. Houzet, and J. S. Meyer, “Ac josephson effect in topological josephson junctions,” *arXiv:1310.5683*, unpublished.
- [31] K. T. Law, P. A. Lee, and T. K. Ng, “Majorana fermion induced resonant andreev reflection,” *Phys. Rev. Lett.*, vol. 103, p. 237001, 2009.
- [32] S. Mi, D. I. Pikulin, M. Wimmer, and C. W. J. Beenakker, “Proposal for the detection and braiding of majorana fermions in a quantum spin hall insulator,” *Phys. Rev. B*, vol. 87, p. 241405, Jun 2013.
- [33] C. W. J. Beenakker, J. M. Edge, J. P. Dahlhaus, D. I. Pikulin, S. Mi, and M. Wimmer, “Wigner-poisson statistics of topological transitions in a josephson junction,” *Phys. Rev. Lett.*, vol. 111, p. 037001, Jul 2013.
- [34] F. Crepin, B. Trauzettel, and F. Dolcini, “Evidence for majorana bound states in transport properties of hybrid structures based on helical liquids,” *arXiv:1401.0507*, unpublished.
- [35] L. Fidkowski, J. Alicea, N. Lindner, R. Lutchyn, and M. Fisher, “Universal transport signatures of majorana fermions in superconductor-luttinger liquid junctions,” *Phys. Rev. B*, vol. 85, p. 245121, Jun 2012.
- [36] V. Mourik, K. Zuo, S. M. Frolov, S. R. Plissard, E. P. A. M. Bakkers, and L. P. Kouwenhoven, “Signatures of majorana fermions in hybrid superconductor-

- semiconductor nanowire devices,” *Science*, vol. 336, no. 6084, pp. 1003–1007, 2012.
- [37] A. Das, Y. Ronen, Y. Most, Y. Oreg, M. Heiblum, and H. Shtrikman, “Zero-bias peaks and splitting in an al-inas nanowire topological superconductor as a signature of majorana fermions,” *Nature Physics*, vol. 8, no. 12, pp. 887–895, 2012.
- [38] S. Nadj-Perge, I. K. Drozdov, J. Li, H. Chen, S. Jeon, J. Seo, A. H. MacDonald, B. A. Bernevig, and A. Yazdani, “Observation of majorana fermions in ferromagnetic atomic chains on a superconductor,” *Science*, vol. 346, no. 6209, pp. 602–607, 2014.
- [39] B. A. Bernevig, T. L. Hughes, and S.-C. Zhang, “Quantum Spin Hall Effect and Topological Phase Transition in HgTe Quantum Wells,” *Science*, vol. 314, p. 1757, 2006.
- [40] M. König, S. Wiedmann, C. Brune, A. Roth, H. Buhmann, L. W. Molenkamp, X.-L. Qi, and S.-C. Zhang, “Quantum Spin Hall Insulator State in HgTe Quantum Wells,” *Science*, vol. 318, p. 766, 2007.
- [41] A. Roth, C. Brune, H. Buhmann, L. W. Molenkamp, J. Maciejko, X.-L. Qi, and S.-C. Zhang, “Nonlocal Transport in the Quantum Spin Hall State,” *Science*, vol. 325, p. 294, 2009.
- [42] K. C. Nowack, E. M. Spanton, M. Baenninger, M. König, J. R. Kirtley, B. Kalisky, C. Ames, P. Leubner, C. Brüne, H. Buhmann, L. W. Molenkamp, D. Goldhaber-Gordon, and K. A. Moler, “Imaging currents in hgte quantum wells in the quantum spin hall regime,” *Nature Materials*, vol. 12, pp. 787–791, 2013.
- [43] S. Hart, H. Ren, T. Wagner, P. Leubner, M. Mühlbauer, C. Brüne, H. Buhmann, L. W. Molenkamp, and A. Yacoby, “Induced superconductivity in the quantum spin hall edge,” *Nature Physics*, vol. 10, p. 638643, 2014.

- [44] C. Liu, T. L. Hughes, X.-L. Qi, K. Wang, and S.-C. Zhang, “Quantum spin Hall effect in inverted type-II semiconductors,” *Phys. Rev. Lett.*, vol. 100, p. 236601, 2008.
- [45] L. Du, I. Knez, G. Sullivan, and R.-R. Du, “Observation of quantum spin hall states in inas/gasb bilayers under broken time-reversal symmetry,” *arXiv:1306.1925*, unpublished.
- [46] E. M. Spanton, K. C. Nowack, L. Du, R.-R. Du, and K. A. Moler, “Images of edge current in inas/gasb quantum wells,” *arXiv:1401.1531*, unpublished.
- [47] I. Knez, R.-R. Du, and G. Sullivan *Phys. Rev. Lett.*, vol. 109, p. 186603, Oct 2012.
- [48] C. Nayak, S. H. Simon, A. Stern, M. Freedman, and S. Das Sarma, “Non-abelian anyons and topological quantum computation,” *Rev. Mod. Phys.*, vol. 80, pp. 1083–1159, Sep 2008.
- [49] N. Read and D. Green, “Paired states of fermions in two dimensions with breaking of parity and time-reversal symmetries and the fractional quantum hall effect,” *Phys. Rev. B*, vol. 61, pp. 10267–10297, Apr 2000.
- [50] A. Y. Kitaev, “Unpaired majorana fermions in quantum wires,” *Physics-Uspekhi*, vol. 44, no. 10S, p. 131, 2001.
- [51] D. A. Ivanov, “Non-abelian statistics of half-quantum vortices in p -wave superconductors,” *Phys. Rev. Lett.*, vol. 86, pp. 268–271, Jan 2001.
- [52] J. D. Sau, R. M. Lutchyn, S. Tewari, and S. Das Sarma, “Generic new platform for topological quantum computation using semiconductor heterostructures,” *Phys. Rev. Lett.*, vol. 104, p. 040502, Jan 2010.
- [53] Y. Oreg, G. Refael, and F. von Oppen, “Helical liquids and majorana bound states in quantum wires,” *Phys. Rev. Lett.*, vol. 105, p. 177002, Oct 2010.

- [54] L. Fu and C. L. Kane, “Superconducting proximity effect and majorana fermions at the surface of a topological insulator,” *Phys. Rev. Lett.*, vol. 100, p. 096407, Mar 2008.
- [55] V. Mourik, K. Zuo, S. Frolov, S. Plissard, E. Bakkers, and L. Kouwenhoven, “Signatures of majorana fermions in hybrid superconductor-semiconductor nanowire devices,” *Science*, vol. 336, no. 6084, pp. 1003–1007, 2012.
- [56] A. Das, Y. Ronen, Y. Most, Y. Oreg, M. Heiblum, and H. Shtrikman, “Zero-bias peaks and splitting in an al-inas nanowire topological superconductor as a signature of majorana fermions,” *Nature Physics*, vol. 8, no. 12, pp. 887–895, 2012.
- [57] A. D. K. Finck, D. J. Van Harlingen, P. K. Mohseni, K. Jung, and X. Li, “Anomalous modulation of a zero-bias peak in a hybrid nanowire-superconductor device,” *Phys. Rev. Lett.*, vol. 110, p. 126406, Mar 2013.
- [58] M. König, H. Buhmann, L. W. Molenkamp, T. Hughes, C.-X. Liu, X.-L. Qi, and S.-C. Zhang, “The quantum spin hall effect: Theory and experiment,” *Journal of the Physical Society of Japan*, vol. 77, no. 3, p. 031007, 2008.
- [59] B. A. Bernevig, T. L. Hughes, and S.-C. Zhang, “Quantum spin hall effect and topological phase transition in hgte quantum wells,” *Science*, vol. 314, no. 5806, pp. 1757–1761, 2006.
- [60] M. Knig, S. Wiedmann, C. Brne, A. Roth, H. Buhmann, L. W. Molenkamp, X.-L. Qi, and S.-C. Zhang, “Quantum spin hall insulator state in hgte quantum wells,” *Science*, vol. 318, no. 5851, pp. 766–770, 2007.
- [61] L. Fu and C. L. Kane, “Josephson current and noise at a superconductor/quantum-spin-hall-insulator/superconductor junction,” *Phys. Rev. B*, vol. 79, p. 161408, Apr 2009.
- [62] C. Beenakker, “Search for majorana fermions in superconductors,” *Annual Review of Condensed Matter Physics*, vol. 4, no. 1, pp. 113–136, 2013.

- [63] J. Alicea, Y. Oreg, G. Refael, F. von Oppen, and M. P. Fisher, “Non-abelian statistics and topological quantum information processing in 1d wire networks,” *Nature Physics*, vol. 7, no. 5, pp. 412–417, 2011.
- [64] J. Reuther, J. Alicea, and A. Yacoby, “Gate defined wires in hgte quantum wells: from majorana fermions to spintronics,” *arXiv:1303.1207*, 2013.
- [65] S. Mi, D. Pikulin, M. Wimmer, and C. Beenakker, “Proposal for the detection and braiding of majorana fermions in a quantum spin hall insulator,” *arXiv:1304.1685*, 2013.
- [66] M. Guigou, P. Recher, J. Cayssol, and B. Trauzettel, “Spin hall effect at interfaces between hgte/cdte quantum wells and metals,” *Phys. Rev. B*, vol. 84, p. 094534, Sep 2011.
- [67] M. Guigou and J. Cayssol, “Andreev spectroscopy of doped hgte quantum wells,” *Phys. Rev. B*, vol. 82, p. 115312, Sep 2010.
- [68] L. Fu, “Electron teleportation via majorana bound states in a mesoscopic superconductor,” *Phys. Rev. Lett.*, vol. 104, p. 056402, Feb 2010.
- [69] K. C. Nowack, E. M. Spanton, M. Baenninger, M. König, J. R. Kirtley, B. Kalisky, C. Ames, P. Leubner, C. Brüne, H. Buhmann, *et al.*, “Imaging currents in hgte quantum wells in the quantum spin hall regime,” *arXiv preprint arXiv:1212.2203*, 2012.
- [70] M. Tinkham, *Introduction to superconductivity, 2nd edition*. Mineola, New York: Dover, 1996.
- [71] V. Ambegaokar and B. I. Halperin, “Voltage due to thermal noise in the dc josephson effect,” *Phys. Rev. Lett.*, vol. 22, pp. 1364–1366, Jun 1969.
- [72] H. Risken, *The Fokker-Planck equation*. Berlin Heidelberg: Springer-Verlag, 1989.

- [73] M. T. Deng, C. L. Yu, G. Y. Huang, M. Larsson, P. Caroff, and H. Q. Xu, “Anomalous zero-bias conductance peak in a nb-insb nanowire-nb hybrid device,” *Nano Lett.*, vol. 12, no. 12, pp. 6414–6419, 2012.
- [74] L. P. Rokhinson, X. Liu, and J. K. Furdyna, “The fractional a.c. josephson effect in a semiconductorsuperconductor nanowire as a signature of majorana particles,” *Nature Physics*, vol. 8, pp. 795–799, 2012.
- [75] A. D. K. Finck, D. J. Van Harlingen, P. K. Mohseni, K. Jung, and X. Li, “Anomalous modulation of a zero-bias peak in a hybrid nanowire-superconductor device,” *Phys. Rev. Lett.*, vol. 110, p. 126406, Mar 2013.
- [76] C. Nayak, S. H. Simon, A. Stern, M. Freedman, and S. Das Sarma, “Non-abelian anyons and topological quantum computation,” *Rev. Mod. Phys.*, vol. 80, pp. 1083–1159, Sep 2008.
- [77] A. Y. Kitaev *Physics-Uspekhi* **44**, 131, 2001.
- [78] Y. Oreg, G. Refael, and F. von Oppen, “Helical liquids and majorana bound states in quantum wires,” *Phys. Rev. Lett.*, vol. 105, p. 177002, Oct 2010.
- [79] R. M. Lutchyn, J. D. Sau, and S. Das Sarma, “Majorana fermions and a topological phase transition in semiconductor-superconductor heterostructures,” *Phys. Rev. Lett.*, vol. 105, p. 077001, Aug 2010.
- [80] J. D. Sau, R. M. Lutchyn, S. Tewari, and S. Das Sarma, “Generic new platform for topological quantum computation using semiconductor heterostructures,” *Phys. Rev. Lett.*, vol. 104, p. 040502, Jan 2010.
- [81] L. Fu and C. L. Kane, “Superconducting proximity effect and majorana fermions at the surface of a topological insulator,” *Phys. Rev. Lett.*, vol. 100, p. 096407, Mar 2008.
- [82] A. Kononov, S. Egorov, N. Titova, Z. Kvon, N. Mikhailov, S. Dvoretzky, and E. Deviatov, “Conductance oscillations at the interface between a superconduc-

tor and the helical edge channel in a narrow hgte quantum well,” *JETP Letters*, vol. 101, p. 41, 2015.

- [83] S.-P. Lee, K. Michaeli, J. Alicea, and A. Yacoby, “Revealing topological superconductivity in extended quantum spin hall josephson junctions,” *Phys. Rev. Lett.*, vol. 113, p. 197001, Nov 2014.
- [84] M. Houzet, J. S. Meyer, D. M. Badiane, and L. I. Glazman, “Dynamics of majorana states in a topological josephson junction,” *Phys. Rev. Lett.*, vol. 111, p. 046401, Jul 2013.
- [85] P. Adroguer, C. Grenier, D. Carpentier, J. Cayssol, P. Degiovanni, and E. Orignac, “Probing the helical edge states of a topological insulator by cooper-pair injection,” *Phys. Rev. B*, vol. 82, p. 081303, Aug 2010.
- [86] C. P. Orth, R. P. Tiwari, T. Meng, and T. L. Schmidt, “Non-abelian parafermions in time-reversal-invariant interacting helical systems,” *Phys. Rev. B*, vol. 91, p. 081406, Feb 2015.
- [87] F. Zhang and C. L. Kane, “Time-reversal-invariant Z_4 fractional josephson effect,” *Phys. Rev. Lett.*, vol. 113, p. 036401, Jul 2014.
- [88] C. L. Kane and M. P. A. Fisher, “Transport in a one-channel luttinger liquid,” *Phys. Rev. Lett.*, vol. 68, pp. 1220–1223, Feb 1992.
- [89] C. L. Kane and M. P. A. Fisher, “Transmission through barriers and resonant tunneling in an interacting one-dimensional electron gas,” *Phys. Rev. B*, vol. 46, pp. 15233–15262, Dec 1992.
- [90] C. L. Kane and M. P. A. Fisher, “Resonant tunneling in an interacting one-dimensional electron gas,” *Phys. Rev. B*, vol. 46, pp. 7268–7271, Sep 1992.
- [91] I. Affleck, J.-S. Caux, and A. M. Zagoskin, “Andreev scattering and josephson current in a one-dimensional electron liquid,” *Phys. Rev. B*, vol. 62, pp. 1433–1445, Jul 2000.

- [92] R. M. Lutchyn and J. H. Skrabacz, “Transport properties of topological superconductor–luttinger liquid junctions: A real-time keldysh approach,” *Phys. Rev. B*, vol. 88, p. 024511, Jul 2013.
- [93] C. Kane and M. Fisher, “Transmission through barriers and resonant tunneling in an interacting one-dimensional electron gas,” *Phys. Rev. B*, vol. 46, pp. 15233–15262, Dec 1992.
- [94] J. A. David J. Clarke and K. Shtengel, “Exotic non-abelian anyons from conventional fractional quantum hall states,” *Nature Communications*, vol. 4, p. 1348, Jan 2013.
- [95] O. M. Yevtushenko, A. Wugalter, V. I. Yudson, and B. L. Altshuler, “Transport in helical luttinger liquid with kondo impurities,” *arXiv preprint arXiv:1503.03348*, 2015.
- [96] I. Affleck and D. Giuliano, “Topological superconductor–luttinger liquid junctions,” *J. Stat. Mech*, vol. 2013, no. 06, p. P06011, 2013.
- [97] M. P. A. Fisher, “Cooper-pair tunneling into a quantum hall fluid,” *Phys. Rev. B*, vol. 49, pp. 14550–14553, May 1994.
- [98] D. L. Maslov and M. Stone, “Landauer conductance of luttinger liquids with leads,” *Phys. Rev. B*, vol. 52, pp. R5539–R5542, Aug 1995.
- [99] D. L. Maslov and M. Stone, “Landauer conductance of luttinger liquids with leads,” *Phys. Rev. B*, vol. 52, pp. R5539–R5542, Aug 1995.
- [100] I. Safi and H. J. Schulz, “Transport in an inhomogeneous interacting one-dimensional system,” *Phys. Rev. B*, vol. 52, pp. R17040–R17043, Dec 1995.
- [101] C. W. J. Beenakker *arXiv:1112.1950*, 2011.
- [102] J. Alicea *arXiv:1202.1293*, 2012.

- [103] N. Read and D. Green, “Paired states of fermions in two dimensions with breaking of parity and time-reversal symmetries and the fractional quantum hall effect,” *Phys. Rev. B*, vol. 61, pp. 10267–10297, Apr 2000.
- [104] D. A. Ivanov, “Non-abelian statistics of half-quantum vortices in p -wave superconductors,” *Phys. Rev. Lett.*, vol. 86, pp. 268–271, Jan 2001.
- [105] J. Alicea, Y. Oreg, G. Refael, F. Von Oppen, and M. Fisher, “Non-abelian statistics and topological quantum information processing in 1d wire networks,” *Nature Physics*, vol. 7, no. 5, pp. 412–417, 2011.
- [106] C. Nayak, S. H. Simon, A. Stern, M. Freedman, and S. Das Sarma, “Non-abelian anyons and topological quantum computation,” *Rev. Mod. Phys.*, vol. 80, pp. 1083–1159, Sep 2008.
- [107] L. Fu and C. L. Kane, “Josephson current and noise at a superconductor/quantum-spin-hall-insulator/superconductor junction,” *Phys. Rev. B*, vol. 79, p. 161408, Apr 2009.
- [108] R. M. Lutchyn, J. D. Sau, and S. Das Sarma, “Majorana fermions and a topological phase transition in semiconductor-superconductor heterostructures,” *Phys. Rev. Lett.*, vol. 105, p. 077001, Aug 2010.
- [109] Y. Oreg, G. Refael, and F. von Oppen, “Helical liquids and majorana bound states in quantum wires,” *Phys. Rev. Lett.*, vol. 105, p. 177002, Oct 2010.
- [110] A. Cook and M. Franz *arXiv:1105.1787*, 2011.
- [111] L. Fu and C. L. Kane, “Superconducting proximity effect and majorana fermions at the surface of a topological insulator,” *Phys. Rev. Lett.*, vol. 100, p. 096407, Mar 2008.
- [112] M. Sato, Y. Takahashi, and S. Fujimoto, “Non-abelian topological order in s -wave superfluids of ultracold fermionic atoms,” *Phys. Rev. Lett.*, vol. 103, p. 020401, Jul 2009.

- [113] J. D. Sau, R. M. Lutchyn, S. Tewari, and S. Das Sarma, “Generic new platform for topological quantum computation using semiconductor heterostructures,” *Phys. Rev. Lett.*, vol. 104, p. 040502, Jan 2010.
- [114] P. A. Lee *arXiv:0907.2681*, 2009.
- [115] J. Alicea, “Majorana fermions in a tunable semiconductor device,” *Phys. Rev. B*, vol. 81, p. 125318, Mar 2010.
- [116] S. B. Chung, H.-J. Zhang, X.-L. Qi, and S.-C. Zhang, “Topological superconducting phase and majorana fermions in half-metal/superconductor heterostructures,” *Phys. Rev. B*, vol. 84, p. 060510, Aug 2011.
- [117] A. Stern and B. I. Halperin, “Proposed experiments to probe the non-abelian $\nu = 5/2$ quantum hall state,” *Phys. Rev. Lett.*, vol. 96, p. 016802, Jan 2006.
- [118] P. Bonderson, A. Kitaev, and K. Shtengel, “Detecting non-abelian statistics in the $\nu = 5/2$ fractional quantum hall state,” *Phys. Rev. Lett.*, vol. 96, p. 016803, Jan 2006.
- [119] L. Fu and C. L. Kane, “Probing neutral majorana fermion edge modes with charge transport,” *Phys. Rev. Lett.*, vol. 102, p. 216403, May 2009.
- [120] A. R. Akhmerov, J. Nilsson, and C. W. J. Beenakker, “Electrically detected interferometry of majorana fermions in a topological insulator,” *Phys. Rev. Lett.*, vol. 102, p. 216404, May 2009.
- [121] J. D. Sau, S. Tewari, and S. Das Sarma, “Probing non-abelian statistics with majorana fermion interferometry in spin-orbit-coupled semiconductors,” *Phys. Rev. B*, vol. 84, p. 085109, Aug 2011.
- [122] E. Grosfeld, B. Seradjeh, and S. Vishveshwara, “Proposed aharonov-casher interference measurement of non-abelian vortices in chiral p -wave superconductors,” *Phys. Rev. B*, vol. 83, p. 104513, Mar 2011.

- [123] E. Grosfeld and A. Stern, “Observing majorana bound states of josephson vortices in topological superconductors,” *Proceedings of the National Academy of Sciences*, vol. 108, no. 29, p. 11810, 2011.
- [124] J. D. Sau, C. H. Lin, H.-Y. Hui, and S. Das Sarma, “Avoidance of majorana resonances in periodic topological superconductor-nanowire structures,” *Phys. Rev. Lett.*, vol. 108, p. 067001, Feb 2012.
- [125] T. Matsuyama, R. Kürsten, C. Meißner, and U. Merkt, “Rashba spin splitting in inversion layers on p-type bulk inas,” *Phys. Rev. B*, vol. 61, pp. 15588–15591, Jun 2000.
- [126] S. Lamari, “Effect of the doping concentration on the zero-field spin splitting and rashba parameter in a p inas mosfet,” *Phys. Rev. B*, vol. 67, p. 165329, Apr 2003.
- [127] S. Estévez Hernández, M. Akabori, K. Sladek, C. Volk, S. Alagha, H. Hardt-
degen, M. G. Pala, N. Demarina, D. Grützmacher, and T. Schäpers, “Spin-orbit coupling and phase coherence in inas nanowires,” *Phys. Rev. B*, vol. 82, p. 235303, Dec 2010.
- [128] A. Romito, J. Alicea, G. Refael, and F. von Oppen, “Manipulating majorana fermions using supercurrents,” *Phys. Rev. B*, vol. 85, p. 020502, Jan 2012.
- [129] A. Yamakage, Y. Tanaka, and N. Nagaosa, “Evolution of edge states and critical phenomena in the rashba superconductor with magnetization,” *Phys. Rev. Lett.*, vol. 108, p. 087003, Feb 2012.
- [130] N. W. Ashcroft and N. D. Mermin, “Solid state physics,” *Solid State Physics, Chapter 9*, 1976.
- [131] P. Fendley, M. P. A. Fisher, and C. Nayak, “Edge states and tunneling of non-abelian quasiparticles in the $\nu = 5/2$ quantum hall state and $p + ip$ superconductors,” *Phys. Rev. B*, vol. 75, p. 045317, Jan 2007.

- [132] J. R. Williams, A. J. Bestwick, P. Gallagher, S. S. Hong, Y. Cui, A. S. Bleich, J. G. Analytis, I. R. Fisher, and D. Goldhaber-Gordon *arXiv:1202.2323*, 2012.
- [133] L. Fu, “Electron teleportation via majorana bound states in a mesoscopic superconductor,” *Phys. Rev. Lett.*, vol. 104, p. 056402, Feb 2010.